David P. O'Neill

University College

Supervised by

Dr. S.J. Payne

Mathematical Modelling of the Effects of Hepatic RadioFrequency Ablation

A thesis submitted for the degree of Doctor of Philosophy

Trinity Term, 2012

A thesis submitted for the degree of Doctor of Philosophy.

Mathematical Modelling of the Effects of Hepatic RadioFrequency Ablation

by David P. O'Neill, University College.

Submitted Trinity Term, 2012.

Abstract

Liver cancer is a major cause of death worldwide and the impact that it has is set to increase in the coming decades. More than half a million cases are diagnosed each year and it is likely many more sufferers are dying unidentified in parts of the world with poor healthcare. Survival rates for untreated cases after diagnosis are low with few patients living beyond one year. A key cause for low survival rates being that the standard treatment is surgical resection; fewer than one quarter of patients are suitable for invasive surgery and five year survival rates rarely exceeds 66 %.

RadioFrequency Ablation (RFA) is a minimally invasive technique which utilises the electrically resistive property of tissue to deposit heat energy locally in the vicinity of the tips of an RFA needle. Heat is transferred away through the tissue by conduction, convection of large blood vessels, and bulk flow of blood in smaller vessels. Liver cells, both cancerous and benign, when exposed to the resultant abnormally high temperatures die considerably more rapidly than in cases of natural hyperthermia. It is thus the radiotherapist's objective to place the RFA needle in a position that maximises destruction of tumour cells, but minimises the collateral damage of surrounding healthy cells. The learning curve of this nontrivial task is reflected unfavourably in the statistics that relate patient survival rate to clinician experience.

In this thesis two mathematical models are presented that could be combined into a 'global' model of the effects of RFA. To predict cell death under RFA, the O'Neill Model is presented in which cells are accounted for by one of three states: *alive*, *vulnerable*, and *dead*. A mechanistic interpretation of the O'Neill Model is attained through comparison to a model from the literature. A known, but little investigated occurrence of tissue swelling in the annular region peripheral to the ablation volume is modelled in a novel way through equations from the literature that track ion transport across the cell membrane; the O'Neill Model for cell death is also incorporated into this model of œdema.

Acknowledgements

There are, of course, a number of people whom I owe considerable thanks to. For the most part there are two groups to be thanked: those who brought me to a place four years ago where I could embark upon postgraduate research, and those whose existence got me to the point of a written thesis.

There is, however, one person who has a foot in both camps; my supervisor, Stephen Payne, was kind (or foolish) enough to encourage me to apply to Univ. as a 6^{th}-former, interviewed and let me in, provided me with the D.Phil. studentship, and then guided and supported me through the doctoral process. His teaching and encouragement have been ever present and gratefully received.

My parents, always supportive and eternally interested in my work deserve the most credit for cultivating my enthusiasm for engineering, and learning in general. Also deserving of thanks are Steve Collins and Mike Chappell amongst my other tutors, and Mark Thompson, my 4^{th}-year project supervisor who encouraged me to continue to the D.Phil. — a decision I was very slow to make, but do not regret.

My research as part of IMPPACT has meant that I have met a memorable team of collaborators. Tingying Peng as one and as fellow member of the group in Oxford deserves singling out as a pleasure to have worked with and an excellent colleague for three busy years. The remainder of the research group, past and present, thank you for providing a lab atmosphere that never made me think twice about cycling up the hill. Claire, for our continual conversation, electronic or conventional; Tee, for late-night lab company; Amit, for your spare-bed-providing generosity; and to all the others, thank you.

Extracurricular activities in three forms have really made my graduate life a (busy) pleasure. Spending the majority of four years always planning the next rehearsal, concert, or tutorial has been a thrill. Thanks must go to those who provided me with teaching opportunities at Univ., New, and Keble Colleges; and to my students, hopefully you have had to think as hard as you have made me think at times.

In the musical side of things the names are too numerous to list, but thank you O.M.O., O.U.Phil., and G.Phil., and all my musical friends I have played alongside and not bossed around. Charlie for giving me an orchestra, Lara for running said orchestra, and my various housemates who have coped with orchestral clutter and noise, thank you.

Molly, I think I might be sussed too, which is wonderful.

Statement of Originality

I hereby declare that this submission is my own work and to the best of my knowledge it contains no materials previously published or written by another person, or substantial proportions of material which have been accepted for the award of any other degree or diploma at the University of Oxford or any other educational institution, except where due acknowledgement is made in the thesis.

Any contribution made to the research by others, with whom I have worked at the University of Oxford or elsewhere, is explicitly acknowledged in the thesis.

I also declare that the intellectual content of this thesis is the product of my own work, except to the extent that assistance from others in the project's design and conception or in style, presentation and linguistic expression is acknowledged.

David P. O'Neill.
Trinity Term, 2012.

Dissemination

Peer-Reviewed Journal Papers

O'Neill, D.P., Peng. T., Stiegler, P., Mayrhauser, U., Koestenbauer, S., Tscheliessnigg, K. and Payne, S.J. A three-state mathematical model of hyperthermic cell death. *Annals of Biomedical Engineering*, **39**: 570-579, 2011.

Payne. S.J., Flanagan. R., Pollari. M., Alhonnoro. A., Bost. C., **O'Neill, D.P.**, Peng. T., and Stiegler, P. Image-based multi-scale modelling and validation of radio frequency ablation in liver tumours. *Philosophical Transactions of the Royal Society A*, **369**: 4233-4254, 2011.

Peng. T., **O'Neill, D.P.**, and Payne, S.J. A Two-equation Coupled System for Determination of Liver Tissue Temperature during Thermal Ablation International *Journal of Heat and Mass Transfer* **54**: 2100-2109, 2011.

Payne, S.J., Peng, T. and **O'Neill, D.P.** Mathematical modelling of thermal ablation. *Critical Reviews in Biomedical Engineering*, **38**: 21-30, 2010.

Peer-Reviewed Conference Proceedings

O'Neill, D.P., Peng, T. and Payne, S.J. The response of hepatocyte cell volume to hyperthermia and its role in oedema. *Proceedings of 33rd IEEE EMBS conference*, 4305-4308, 2011.

O'Neill, D.P., Peng, T. and Payne, S.J. Comparison of two mathematical models for hyper thermic cell death. *Proceedings of 6th World Congress on Biomechanics*, Volume 31, Part 2, pp. 748-751, 2010.

O'Neill, D.P., Peng, T. and Payne, S.J. A two-equation coupled system model for determination of liver tissue temperature during Radio Frequency Ablation. *Proceedings of 31st IEEE EMBS conference*, 3893-3896, 2009.

Peng, T., **O'Neill, D.P.**, and Payne, S.J. Mathematical study of the effects of different intrahepatic cooling on thermal ablation zones. *Proceedings of 33rd IEEE EMBS conference*, 6866-6869, 2011.

Peng, T., **O'Neill, D.P.**, Payne, S.J., Bost, C. and Flanagan, R. Mathematical modelling of directional effects of perfusion on liver tissue temperature of radio frequency ablation. *Proceedings of 6th World Congress on Biomechanics*, Volume 31, Part 2, pp. 740-743, 2010.

Peng, T., **O'Neill, D.P.**, and Payne, S.J. 1-D steady state analysis of a two-equation coupled system for determination of tissue temperature in liver during Radio Frequency Ablation. *Proceedings of 31st IEEE EMBS conference*, 3385-3388, 2009.

CONTENTS

LIST OF FIGURES

LIST OF TABLES

CHAPTER 1

INTRODUCTION

1.1 BACKGROUND

Liver cancer is currently the fifth most prevalent cancer worldwide but it is disproportionately the second most frequent cancerous cause of death [54]. Annually more than 700,000 people are diagnosed worldwide, of which approximately two thirds are in China alone [11]. The past few decades have seen a strong research focus on both cancer diagnostics and cancer treatments, however while breast cancer, leukæmia and colorectal cancer have been key targets, liver cancer has yet to see improvements on the same scale. Due to the lack of obvious physical signs (such as breast or testicular 'lumps'), and because symptoms of liver cancer primarily appear later than those of other cancers, successful diagnoses for liver cancer are difficult to obtain in the early stages when tumours are easily treatable. Without treatment after diagnosis, sufferers are unlikely to live for more than one year and most die within six months.

Cancerous tissue in the liver can be primary (originating in the liver) or secondary (originating elsewhere in the body). The majority of primary liver cancers are hepatocellular carcinomata or cholangiocarcinomata which respectively are the result of typical cancerous developments in the hepatocytes (standard liver cells) and cancers in bile duct cells. Secondary cancers are highly common in the liver because of the physiological purpose of the liver, namely as a filter for the body's circulatory system [49]. Cancerous cells from tumours elsewhere in the body occasionally break off from the associated tumour and travel with the blood until being deposited in the liver; this is a metastatic cancer. Common metastatic tumours in the liver are associated with colorectal, lung, breast, and esophageal cancers amongst others; thus as incidence rates for these other cancers rise, so too will the incidence rates for liver cancer.

For primary liver cancers, tissue is often cirrhotic, where abnormally fibrous sections of tissue replace soft, functioning hepatocytes. Cirrhosis has a strong link with alcoholism [42] which is a factor that will likely see occurrence rates rise significantly in the coming decades as millions of people in China and sub-Saharan countries become more affluent and obtain greater access to alcohol.

Worldwide, liver cancer is a major cause of death and it is set to become even more prominent in the near future. It is likely that, unlike many other cancers, the best plan of action to deal with liver cancer is to focus research efforts upon treatment technologies and techniques rather than diagnostic methods and prevention practices.

1.2 CLINICAL ISSUES

The traditional method of treating a liver cancer is surgical resection, requiring several hours of surgery under general anæsthetic, a minimum of one surgeon, litres of blood for transfusion, several theatre nurses, and a ward bed for a number of nights to recover in and to be monitored. Amongst other considerations, the skill of the surgeon performing the resection is restricted to removing 'what the eye can see'. Even 99 % removal of a tumour is paramount to a failed operation as only a minimal number of cancerous cells are necessary for the cancer to regrow and return the patient to a similar, if not worse, situation than before the resection. The ideal solution is clearly a minimally invasive and quick treatment that guarantees near 100 % tumour cell destruction and requires far fewer medical staff man-hours.

RadioFrequency Ablation (RFA) is a technique that meets many of these criteria. The technique can be performed under local anæsthetic and involves inserting a needle (approximately the size of a large biopsy needle) through the skin and healthy tissue into the tumour to be treated. An oscillating voltage is applied to the needle's electrodes and heat is dissipated in the surrounding tissue. The accumulation of heat in the tissue causes a rise in temperature and results in cell death; treatment times range from ten minutes to more than half an hour dependent upon the desired ablation size. Furthermore, only one radiotherapist is required for the procedure, no blood transfusions are necessary, recovery time is typically less than 24 hours and there is minimal scarring for the patient. The shorter times for treatment and recovery permit a greater throughput of patients, and the cost of equipment and staff time is considerably lower. An additional benefit of RFA is that for many patients resection is not an option (due to limited hepatic reserve, vulnerability to general anæsthetia, or tumours that are too widely spread across the liver). Beard *et al.* [6] report as many as 75 % – 90 % of patients with liver tumours (col-

orectal metastases in this instance) do not receive potentially curative resections. A considerable number of these patients remain possible candidates for RFA, thus increasing the number of cancer sufferers who can be treated.

The obvious criterion not yet mentioned is the confidence of achieving 100 % destruction of cancerous cells. Statistical evidence exists to claims that RFA outperforms surgical resection with respect to patient survival rates. Hildebrand *et al.* [53] report achievable 2-year survival rates (the proportion of patients alive two years after treatment) of 89 % for RFA, whilst França *et al.* [41] report 2-year survival rates for surgical resection that range from 88 % to as low as 57 % across different reports. However, the study by Hildebrand *et al.* also noted the experience level of the radiotherapists and the high reported survival rate only applied to radiotherapists who had practised the treatment for more than two years. When considering only the radiotherapists with experience totalling less than two years, the survival rate dropped significantly to 46 % [53]. Thus, RFA was shown to outperform liver resection but was strongly dependent upon the radiotherapist performing the procedure.

Examination of the RFA procedure carried out by radiotherapists presents a comprehensive set of protocols for various tumour sizes and target ablation sizes, but little more. For example, the protocols associated with the RITA Starburst needle [128] used by the clinicians and experimentalists who were collaborators with the author specify a sequence of 'target temperatures' and heating durations to achieve a target ablation zone size. The power output by the needle is controlled by a 'black box' which contains a feedback loop based upon the mean temperature recorded across five prongs of the needle. In many cases the radiotherapist elects to turn off one sensor if he feels it is giving misleading information (such as a low temperature that might indicate a prong tip inside a large vessel cooled by the flowing blood). The difference in performance between experienced and inexperienced radiother-

apists derives from the decisions made mid procedure to deviate from the protocol, or to repeat an ablation.

With high success rates (89 % or higher [53]) possible there is clearly the potential to improve success rates across the field of radiotherapy. The challenge is to facilitate the accumulation of experience to aid the treatment decisions made by all radiotherapists. This clinical support can be provided though two different forms: real-time simulation code providing predictions of ablation success during treatment, and an 'offline' software package containing a library of past ablations for use as a training simulator. The facilitation of these two clinical aids constitute the target for the research project outlined in the following section.

1.3 PROJECT: FUNDING AND COLLABORATION

The research presented in this thesis was made possible by funding from the European Commission under the Seventh Framework Programme. Funding was granted for a small or medium-scale focused research project (STREP) consortium consisting of collaborators from the following institutions: Fraunhofer Institute (Bonn), Technische Universität Graz, Universitaet Leipzig, Medizinische Universität Graz, Teknillinen Korkeakoulu (Helsinki University of Technology), NUMA Engineering Services Ltd (Ireland), and the University of Oxford. In Oxford the research was carried out by the PUMMA group of the Institute of Biomedical Engineering; within the group the involved members are Dr. S. J. Payne (Principal Investigator for the group), Dr. T. Peng (a Postdoctoral Research Assistant), and the author of this thesis.

The full title of the project was **I**mage-based **M**ulti-scale **P**hysiological **P**lanning for **A**blation **C**ancer **T**reatment and is hereafter referred to as the IMPPACT project [131]. The major objective of the IMPPACT project was to create a patient

specific intervention planning system (IPS) for RadioFrequency Ablation (RFA). The IPS was to be based upon a patient specific physiological model of the liver under local hyperthermia intervention, and its functions were twofold: firstly to help all clinicians in their planning of treatments, and secondly to facilitate the dissemination of experience accumulated by experienced radiotherapists to train less experienced radiotherapists. Oxford's role in the IMPPACT project was to provide a new bio-heat equation, models of cell heating effects, and a mathematical model for the prediction of hyperthermic cell death.

1.4 THESIS SYNOPSIS

There are two facets to the modelling presented in this thesis, each with a novel mathematical model: the rate at which cells subjected to supraphysiological temperatures progress from alive to dead, and how temperature and cell death result in cell swelling.

The next chapter establishes the background information such that the models that are presented in the following chapters can be discussed in context. This literature review contains four parts. First, the physiology of the liver that is relevant to the thesis is discussed, providing details on the anatomical structure of the liver, its function, and the various cells that make up the liver tissue. Also discussed are some of the important pathologies that should be considered when modelling, including cirrhosis and liver cancer. For any thermal ablation modelling, the temporal and spatial development of the temperature field must be modelled or approximated. Much research has been published on heat-transfer modelling. Some of the more significant work is reviewed, after which is a review of literature pertinent to the models presented in the following chapters.

The next two chapters, 3 and 4, first present a novel mathematical model for thermally induced cell death and then show steps taken to refine, to develop, and to validate the model. A third chapter dealing with the cell death model follows, where the empirically based model is related to a mechanistic model from the literature for the purpose of furthering insight into the behaviour of cells during RFA in a multi-scale framework.

A model for thermally induced cell swelling is presented in chapter 6. This novel model was developed to try to predict a clinically observed phenomenon, that of the appearance of an annular ring, visible in intra- and post-operative imaging data and occurring in the region peripheral to the ablation volume. The model successfully shows that thermal variations can result in œdema (swelling). The thesis concludes with chapter 7 which assesses the modelling achievements and explains how the three models combine to form a larger 'global' model of thermal ablation. The issue of validation is also discussed which leads to a number of recommendations for the direction in which further work should be pursued.

CHAPTER 2

LITERATURE REVIEW

Some of the literature reviewed in this chapter — sections 2.3 - 2.4 — has also been reviewed in: Payne, S. J., Peng, T., and **O'Neill, D. P.**. "Mathematical Modelling of Thermal Ablation" *Critical Reviews in Biomedical Engineering*, **38:** 21-30, 2010.

That review paper was based upon the literature review presented in the Probationary Research Student Transfer Report written by the author in Trinity Term 2009.

2.1 INTRODUCTION

This chapter contains a review of the relevant literature in four principal parts. The first section details the physiology relevant to the research that is presented in the following chapters. Fundamental to all thermal ablation modelling is determining the development of the applied temperature field, and so a review of the literature of heat transfer models is included for a wider perspective of the field. The order of the remaining sections directly corresponds to the progression of the following chapters; thus the first section covers models for predicting heat-induced cell death and tissue damage, and the final section details models that deal with cell membrane potential and associated ion transfer.

2.2 LIVER PHYSIOLOGY

The liver is one of the major internal organs, considered alongside the heart, brain, lungs, and digestive system. It is situated in the upper abdomen, below the lungs and heart, but above and to the right of the stomach. The liver interacts directly with the gall bladder, and indirectly with other organs via the blood stream by way of blood vessels. Three vessel trees permeate the liver, the arterial tree which by definition transfers blood away from the heart (and thus *to* the liver), and the venous tree which transfers blood back. The third vessel tree is that of the hepatic portal vein — a vessel that carries blood that has previously traversed the gut, but, before joining the rest of the venous blood system, brings this nutrient-rich blood through the liver.

Etymologically, liver in Greek is *hepar* and this gives rise to the the medical prefix, *hepato-*, and the adjectival form, *hepatic* — two terms which will appear throughout the following sections.

2.2.1 Liver Function

Weighing in at approximately 2.5 % of an adult male's body weight (1300–1700 g) [2], the liver is possibly the most multidisciplinary organ in the mammalian body, providing a wide range of vital services to the rest of the body. Situated between the gut (and spleen) and the rest of the body, it serves to store large quantities of carbohydrates, amino acids, lipids, and vitamins and subsequently to regulate the controlled release of these into the vascular system. Simultaneously, it uptakes and disposes of pollutant xenobiotics (foreign bodies), foreign antigens and microbes that have managed to enter the blood stream [45]. So as to facilitate these and many other functions, the liver takes the form of a structurally complex tissue with a unique vascular network and consists of a number of different cell types [2].

2.2.2 Anatomy of the Liver

Approximately 80 % of blood flowing to the liver is delivered by the hepatic portal vein, with the remaining 20 % supplied by the hepatic artery [106]. The blood in the artery is fully oxygenated as it arrives at the liver having come directly from the heart, however, blood in the portal vein, having first traversed the gut, arrives at approximately 60 % oxygenation. It is important to remember that despite being named a 'vein', the hepatic portal vein is, in fact, a vessel transporting blood *to* the liver.

These three, sizeable blood vessels enter the liver in the porta hepatis, a short but deep fissure, approximately 5 cm in length, situated near the centre of the organ. Around this, the liver tissue is formed into multiple lobes of unequal sizes and varying shapes. Also present is the gall bladder, which has its own vessel tree of biliary ducts which also permeates the liver tissue.

2.2.2.1 Hepatic Blood Circulation [39]

Due to its nature as a storage organ and filtration unit, the liver is well perfused. The vasculature of the liver has a large capacity with a low resistance [48]. Approximately 22 % of the liver's volume is taken up by blood vessels [69], which at any instant contain roughly 12 % of the blood in the entire human vascular system [69]. This can be rapidly and easily reduced by nervous contraction of the many larger vessels should the body require the available hæmic reserve to be expanded.

Values of perfusion in the adult human lie in the range 1500–2000 ml/min [69] which equates to approximately one quarter of cardiac output [67]. Due to reasons explained in section 2.3, blood flow plays a significant role in the majority of the reviewed models of heat transfer.

The state of general anæsthesia for a patient may or may not directly alter the hepatic blood flow: there has been published work showing decreased blood flow [51] and [120], however there have also been other findings which show no change [46] [36]. Results of decreased blood flow may be caused by specific drugs used in anæsthesia, changes in blood pressure resulting from altered heart rates, and other indirectly related effects. One such effect of general anæsthesia that alters the flow of blood to the liver is posture; movement from an upright position to lying prone increases flow by an average of 40 % [20].

2.2.2.2 Liver Tissue [30]

The operational liver can be thought of as a continuous mass of cells, through which a widespread and fine network of vessels carry venous blood; the venous blood returns to the heart having previously traversed the network of vessels in the gut. These functioning liver cells are partitioned by a system of single-cell thick walls which classifies liver tissue as a muralium simplex (walls of brick-like construction that are one cell thick) [2]. The walls in the liver are also referred to as 'liver plates' or 'laminæ hepatis' and the spaces inbetween which house the vascular network are named 'lacunæ hepatis' [27]. Due to perforations in the laminæ, the lacunæ are continuous throughout the organ. The smallest of the lacunæ are occupied by the capillary-sized sinusoids which are discussed in the next section.

Bordering the organ, the liver parenchyma (the fundamental tissue of an organ) is surrounded by a single layer of hepatic cells which is continuous with the muralium and termed the 'subcapsular limiting plate' [28]. This in turn is surrounded by fibrous cells making up the fibrous capsule [2]. Since all of the laminæ are connected via the limiting plate and all of the lacunæ are similarly completely interconnected, the whole liver may be thought of as two continuous parallel plates

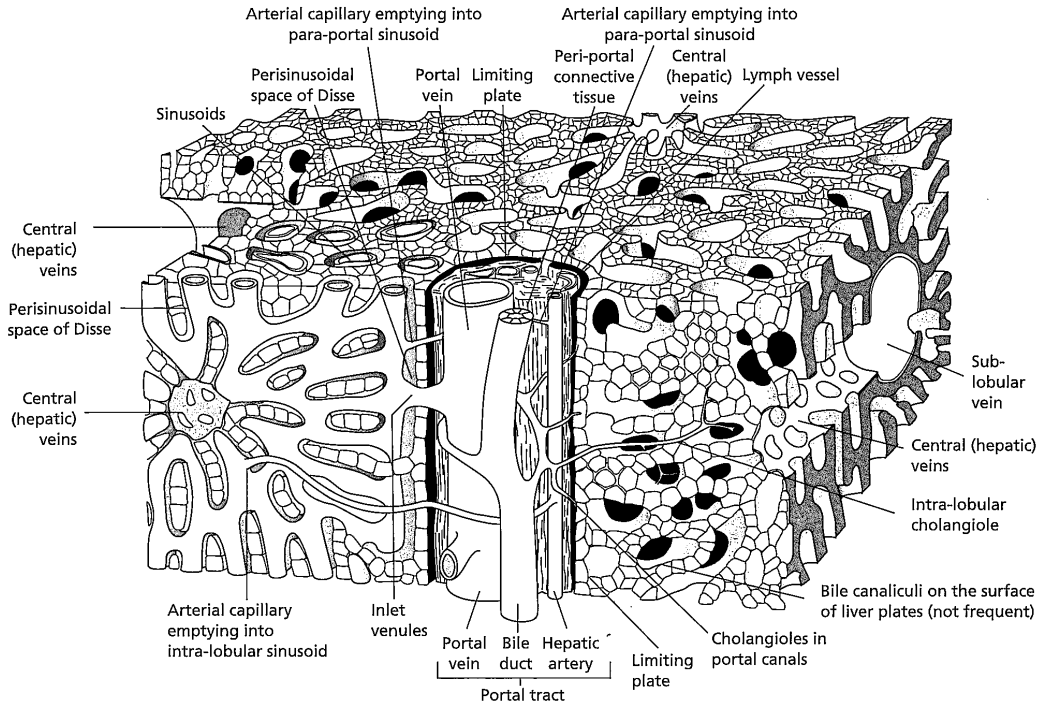

Figure 2.1: Example structure of the normal human, showing a single section of a portal tract, with single branches of the portal vein, hepatic artery, and bile duct. Surrounding the portal vein, the sinusoids are shown to permeate the parenchyma. Running horizontally, normal to the portal tract, are the hepatic veins; relative sizes are approximately correct. Also shown are the more minor structures: limiting plate, perisinusoidal spaces of Disse, lymph vessels, and arterial connections with the sinusoids. Figure reproduced from Sherlock and Dooley [122].

but shaped into a curious geometry that is continually branching and recurrent upon itself. Figure 2.1 (reproduced from Sherlock and Dooley [122]) shows many of the structural features of the physiology of liver tissue, including the perpendicular alignment of hepatic veins with respect to the core portal tract. The small-scale random distribution of the sinusoids, described next, through the parenchyma can be seen along with the even distribution that is obvious when the sub lobule is viewed as a whole. Also indicated are many of the smaller structures, some of which will be mentioned below.

2.2.2.3 The Sinusoids [30]

The laminæ of the liver are permeated by a three-dimensional network of specialised capillary-like vessels termed 'sinusoids'. The sinusoids, which account for 60 % of hepatic vascular volume [48], are the final hierarchical step of the portal vein distribution tree before recombination of vessels in the (true) venous tree. This tree starts with the first bifurcation of the hepatic portal vein into its two main branches soon after entry to the liver through the porta hepatis. Blood flow in typical capillaries is limited by high frictional forces that result from extremely narrow diameters; the flow in sinusoids has to be controlled via a different method as the sinusoids serve as (comparatively) large reservoir vessels. Common suggested mechanisms for controlling sinusoidal flow include regulation by sphincters and Kupffer littoral cells. Sphincters are present at the point of blood arrival from the preceding vessel, whilst Kupffer littoral cells are situated along the length of the sinusoid and are capable of protruding into the central void of the sinusoid in order to slow, or even to block, the flow of blood. However, this is not without controversy: some studies suggest regulation at both ends of the sinusoid [76], but others find no evidence of sphincter presence [88].

As the primary purpose of the liver requires it to be a well perfused organ, the liver can be usefully thought of as a combination of tissue volumes, each being supplied by a single portal vein branch. The region of tissue that surrounds a single portal vein branch is termed the vein's 'portal canal', or 'tract'. Each portal canal is typically also served by two or more branches of the arterial tree. These arterial branches anastamose with each other to generate a coarse mesh of arterial capillaries supplying oxygen to the parenchymal tissue; thus enabling it to function as required as the portal vein blood passes through each portal canal. The smallest vessels of the hepatic arterial tree flow not into the venous tree as would be typical

in other organs, but into the network of sinusoids. Thus sinusoids in liver contain well-mixed blood that is high in oxygen from the arterial tree and high in nutrients from the portal vein tree. A further set of regulatory sphincters are present at the terminal end of the sinusoids. Control of these sphincters in combination with the entry sphincters and the Kupffer cells can result in stasis — volumes of blood held stationary in the sinusoids that disrupt the hepatic circulation.

Whilst the portal vein and hepatic artery physical pairing produces the well defined region of a portal canal, the hepatic vein interacts over similarly well defined, but distinct areas [32]. For the most part, portal veins cross portal canals perpendicularly [30]. There are very few anastomoses in the hepatic venous tree which culminates in three large hepatic veins: the vena hepatica dextra, demia, and sinistra; all three of which drain into the inferior vena cava. The result of this 'cross-hatching' between the pre-sinusoidal and post-sinusoidal trees in the combined vessel network is an organ that is well perfused throughout but with strong flow heterogeneity resulting from the strongly directional flow of the portal canals and the later stages of the venous tree. This way, in which the liver is segmented purely by the presence of distinct hæmodynamic patterns that are determined by the portal canals, is different to all other glands which are primarily partitioned by connective tissue encased lobules [2].

2.2.3 Liver Cells

Hepatocytes make up almost 80 % of liver cell volume and approximately 60 % of liver cell numbers (approximately 100 billion in the normal adult human [10]). Taking a complex rhomboidal form with distinct surfaces that are tailored to performing different functional operations [107], hepatocytes are positioned such that approximately 37 % of their surface area is directed towards sinusoids. The majority of

the remaining surface area then contacts with adjacent hepatocytes [133], with the final 13 % contacting the bile canaliculi (the smallest vessels in the bile duct vascular network) [133].

In addition to the hepatocytes of the hepatic parenchyma, at least six other cell types are also present: cholangiocytes, sinusoidal endothelial cells, macrophages (including Kupffer cells), lymphocytes, dendritic cells and stellate cells [2]. These 'other' cells make up approximately 6.5 % of liver volume but account for 40 % of the total population of liver cells [63]. Of most interest here are the stellate cells, also known as Ito cells, lipocytes, perisinusoidal cells, vitamin A-rich cells, and fat-storing cells. They earn the last name because of their most characteristic structural feature: the existence of multiple fatty droplets. These lipid deposits vary in number and size but can be up to 4 μm radially [63]. The number, sizes and form of the lipid droplets depend upon a number of factors including the vitamin A content of the individual's diet [85], [86]. Typically, the overall content of the fat deposits in normal human liver stellate cells is approximately 20 % of cell volume [124].

Whilst stellate cells seem relatively insignificant in comparison to the large numbers and large size of hepatocytes (there numbers approximately 1 stellate cell for every 20 parenchymal cells), they have been found to exhibit marked enlargement in patients with progressive alcoholic liver disease [5]. Heptatic stellate cells are found primarily in the perisinusoidal space and perform a prominent role in processes with growth factors, and the generation of the extracellular matrix [119].

Myofibroblasts (cells with features of both smooth muscle cells and fibroblasts) that appear in liver cirrhosis have been suggested to originate from liver stellate cells [25] and this transformation of quiescent stellate cells into myofibroblasts is thought to be initiated by the release of substances from damaged hepatocytes, Kupffer, and/or endothelial cells [63]. The increased prevalence of myofibroblasts

and stellate cells varies depending upon pathology: in instances of acute liver injury stellate cell numbers increase prominently, whereas the number of myofibroblasts remain nearly constant; conversely, in liver with chronic damage, numbers of both myofibroblasts and stellate cells rise [64].

2.2.4 Fibroblasts

Due to certain restrictions that faced experimental collaborators, lung fibroblasts were used in some of the cell co-cultures of chapter 3 and chapter 4; thus, lung fibroblasts are discussed briefly here. Fibroblasts are principally responsible for the production of the macromolecules that make up the extracellular matrix whilst endothelial cells and contractile cells also contribute to the production of connective tissue [103]. They are typically spindle-shaped and in tissue; their migratory patterns define the resulting patterns of the collagen fibrils found [104]. In the lung, the collagen and elastin produced by fibroblasts are two of the main components of the interstitium in the alveolar wall [136]. Simple tissue cultures of fetal lung fibroblasts, such as the MRC-5 cell line, when not additionally treated with collagenase, grow in the structure of multilayered arrays [103] rather than in the more complex structures typically found elsewhere.

Fibroblasts perform a key role in the pathogenic condition of fibrosis. An occurrence of lung fibrosis, much like fibrosis of the liver in cirrhosis which will be discussed in subsection 2.2.6, results in an excess of connective and fibrotic tissue in and around the lung and produces an abnormally stiff tissue. Cases of idiopathic pulmonary fibrosis show upward of 50% of lung tissue consisting of fibrotic tissue which equates to more than thrice the expected mass in healthy lungs (~16 %) [103]. It is likely that the majority of the new fibrotic tissue is created following a path from

the death of epithelial cell death (for whatever cause), attempted replacement of the epithelial cells, and subsequent fibroblast proliferation.

2.2.5 Liver Cancer [31]

Across the body, all cancers are either primary or secondary, depending upon whether they are found in the tissue from which they originated, or they have metastasised (moved and settled) from elsewhere in the body. Of the primary liver cancers, there are two principal types and also several minor carcinomata that are considerably more rare; these are:

- Hepatocellular carcinoma (HCC): The most common primary cancer, making up at least 85 % of primary tumours; it is a cancer which is derived from hepatocytes. Whilst it is sometimes referred to as hepatoma, this term has been actively discouraged because it is sometimes inferred to be benign.
- Cholangiocarcinoma: A primary cancer deriving from cells of the bile ducts found in the liver. Similarly, the technically valid name cholangioma is discouraged for inferences of benignity. These carcinomata account for approximately 10 % of primary tumours.
- Angiosarcoma: Also known as hæmangio-endothelioma or hæmangiosarcoma, accounting for only 1 % of primary cancers, it is derived from the cells of the blood vessels and is most commonly found amongst elderly patients.
- Hepatoblastoma: A primary cancer normally found only in young children under the age of 4.
- Fibro-lamellar carcinoma: A cancer deriving from the fibrotic primary cells of the liver.

- Combined hepatocellular-cholangiocarnima: A carcinoma that exhibits traits of both HCC and cholaniocarcinomata. Different specimens show features of each in differing proportions.

In HCC, which by definition originates from liver cells, the muralium simplex previously described undergoes a transformation and they can result in any number of a plethora of alternative structures. Various shapes have been observed including tubular, fingerlike, and vesicular. These shapes are not mutually exclusive and can coexist in cohabiting tumours as well as in different regions of a single, larger, tumour [26].

Due to the physiological role of the liver as a highly perfused medium, it is the most frequent final destination for blood-transported metastases; approximately one third of all cancers involve tumours in the liver [121]. Metastatic carcinomata in the liver have been found to originate from all other primary cancers, including those found in tissue of the breast, lung, prostate, oesophagus, colon, stomach, and endometrium. In the liver, secondary (metastatic) cancers are at least 30 times more common than primary cancers [122]. Metastases found in the liver are often considerably larger than would be expected in their primary site. Additionally, Elias [29] found that parenchyma surrounding the metastasis can become malignant.

It should also be noted that, of course, HCC can metastasise to other organs; a particularly common destination being the lung. However, this is of minor interest here as the primary concern is with treatment of carcinomata in the liver.

HCC can be attributed to a number of ætiological factors including cirrhosis which is discussed in detail in the following section, hepatitis B, hepatitis C, excessive alcoholism, and a number of rarer causes. Considering occurrence of HCC worldwide, hepatitis B and C are the two greatest influences and this is evident by

the high rates of HCC in regions such as SubSaharan and West Africa, China, and Southeast Asia [38]. The exact mechanisms that lead from hepatitis and cirrhosis to the occurrence of HCC are not , however, well known [122].

The physiological performance of a liver containing HCC can be altered; the hepatic and/or portal veins may be thrombosed and can contain additional tumours, resulting in modified blood flow to some or all of the liver. Some tumour specimens, particularly those in non-cirrhotic livers of Japanese patients, may occur with their own fibrous capsule having developed around the tumour [122]; such tumours are normally of the 'expanding' type, rather than the 'spreading' or 'multifocal' types more common in the west and Africa which possess no capsule but instead have a finger-like exterior. Different formations of tumour appear distinctly in clinical imaging and have different implications for the planning of ablation therapies. Alcoholics in Northern Europe and North America have four times the the risk of primary HCC than those who have no alcohol-caused liver damage; cirrhosis is expected in all alcoholic cases [122].

2.2.6 Cirrhosis [106]

Cirrhosis, which is often coexistent with liver carcinoma, results in fibrotic lesions appearing in the liver tissue. In Britain, India, and North America, 10-20 % of cirrhotic livers are also cancerous, whilst in South Africa this rises to above 30 % [122]. Conversely, approximately 60 % of HCC cases occur in cirrhotic livers [122]; in these cases, patient prognosis is worse than in non-cirrhotic livers. Three characteristics common to all cirrhosis are the destruction of hepatocytes, generation of scar tissue, and regeneration of parenchyma cells. Many causes of cirrhosis have been identified, including viral hepatitis (B, C, and D), alcohol, and autoimmune hepatitis, as well as various toxins and drugs [122]. The nature of the processes leading

to cirrhosis is such that it forms a vicious cycle. Cells in tissue that is well perfused are at most risk as they are the best supplied with toxins responsible for cell destruction. With the generation of scar tissue and the regeneration of parenchyma that follow cell death, comes a corresponding degree of angiogenesis and thus an increased vasculature which improves the local circulation. This increased circulation in turn increases the delivery of damaging toxins and thus the destructive, cirrhosis-generating cycle is completed. In cases where this cycle is not sustained, cirrhosis can still occur: the generation of scar nodules disrupts blood supply which additionally results in necrotic cell death and therefore further fibrogenesis [122]. Also important to note is that because cirrhosis often requires high levels of toxin delivery and the liver is typically a well perfused organ, cirrhosis can occur throughout the organ, and is not confined to local regions.

The principal mechanical consequences of cirrhosis in the liver is that the ratio between hepatic and fibrotic tissue shifts towards more of the latter. Fibrotic tissue is typically a much stiffer and firmer tissue than the hepatic tissue; this is because its primary, naturally occurring purpose is to be a tissue providing structural support for functional tissue. Other consequences of cirrhosis in the liver are an increased blood content which is primarily contained in the increased arterial vascular network; increased portal pressure due to narrower and fewer sinusoids; and detrimentally increased heterogeneity of the vascular network due to vascular generation/regeneration being driven by cirrhosis instead of by the intention to create well perfused parenchyma. The increased vascularisation created by newly generated capillaries that bypass sinusoids can result in intrahepatic shunting of blood — blood draining prematurely into the venous tree. Shunted blood volumes range from 20 % of total blood flow in the liver in cases of light cirrhosis, to between 18 % and 78 % of total blood flow in severe cirrhosis [87], all of which significantly modify

the flow rates and directions from those in a healthy liver. Total hepatic blood flow in cirrhotic livers is variable [39]; mean values of blood flow are typically reduced, but large variations have been recorded.

2.2.7 Heat Shock Proteins

First discovered by Ritossa in 1962 [108], the heat shock response was observed when thermally induced chromosome puffs were induced in fruit fly salivary glands that had been exposed briefly to elevated temperatures. Similar puff appearances were observed in with cells treated with nitrophenol or sodium salicylate. Early work was focussed on showing that these puffs appeared in the first few minutes of treatment [3] [8], were found to appear in species other than *Drosophila busckii* and in different tissues [109] [7], and were caused by a number of other stress treatments [3] [8] [71]. Now termed *heat shock proteins*, these stress-induced puffs are categorised according to their molecular size, with categories covering a range of 10-kiloDaltons; the most widely studies families of HSPs are the Hsp60, Hsp70, and Hsp90 with respective weights of the order of 60, 70, and 90 kiloDaltons[74].

Whilst the causation and generation of heat shock proteins are well studied, their effects are still under investigation. HSPs are believed to control the path towards cell death and in some cases protect the cell against it [56]. The presence of HSPs can be detectable by the immune system and this has implications in drug-based anticancer treatments. Hsp90 in particular has been suggested as a target for cancer therapy [116]. The generation of HSPs protects the cell in two key manners; first, the energy taken up though the folding and denaturation of the heat shock protein is energy absorbed and no longer available to damage other, thermally sensitive, cell constituents. Secondly, the presence of HSPs are suspected to perform an important role in the regulation of the apoptotic pathways towards cell death,

acting as 'chaperones' in the renaturation or the destruction of damaged proteins [68]. Regarding heat treatment and thermal ablation, HSPs are known to have increased presence in cells exhibiting thermotolerance [94]. Thermotolerance is the increased resistance to heat damage shown by cells that have previously been exposed to thermally stressful, but nonlethal conditions. Consideration of the various roles HSPs play in the thermal ablation of cells must be given when examining the literature for heat transfer in the next section of this chapter, and for models of cell death which are reviewed subsequently.

2.3 HEAT TRANSFER

Many papers dealing with heat transfer have been published since Pennes' seminal paper of 1948 [102] which is first presented; some of the most significant modifications and alternatives to Pennes' bio-heat equation are then also discussed.

2.3.1 Pennes' model

By far the most referenced paper on biological heat transfer was published by Pennes in 1948 [102]. Based upon measurements in the human forearm, Pennes theorised that thermal changes in biological tissue were due to three heating contributions: a conduction term, a metabolic term and a perfusion term as shown in Equation 2.1:

$$\rho c \frac{\partial T}{\partial t} = \nabla \cdot k \nabla T + q_m + \left(\rho c\right)_b \left(T_{b,in} - T_{b,out}\right) \omega_b, \tag{2.1}$$

where T, ρ, c and k are the temperature, density, specific heat capacity and thermal conductivity of the tissue, and q_m is the heat generated per unit volume due to metabolic processes. The third term on the right-hand side represents a sink-effect contribution of blood flowing in the tissue; this is written such that $\left(\rho c\right)_b$ is the volumetric heat capacity of blood, $T_{b,in}$ is the temperature of blood entering a control

volume and $T_{b,out}$ is the temperature of blood exiting the same control volume, and ω_b is a 'perfusion' value which has dimensions of $\frac{volume}{time}\frac{1}{volume}$ (or a volumetric volume flow rate). The basis for this term is the heat transfer between perfused tissue and the blood contained in the capillaries. Capillaries are the smallest blood vessels in both length and radius, and have the slowest blood velocities due to their large number. Due to these small dimensions and the great number of capillaries, it is impossible to account for them individually. Instead, Pennes' model assumes blood enters a hypothetical pool at a rate of ω_b and at a spatial and temporally uniform temperature ($T_{b,in}$) and leaves at the same perfusion rate but at a temperature $T_{b,out}$.

By analysing experimental results, Pennes simplified Equation 2.1 by assuming that heat transfer between tissue and blood occurs solely across capillary walls. Thus, in the simplification, Pennes set the influx temperature ($T_{b,in}$) to T_a, the temperature of the blood in the main supply arteries (the vessels Pennes assumed were responsible for the volumetric volume flow rate) — normally taken to be 37 °C. Pennes further assumed that the rate of heat transfer is such that the blood instantaneously equilibrates with the surrounding tissue before exiting the pool into the venous system, thus tissue temperature (T) replaces $T_{b,out}$. The form of Pennes' findings after the simplifications has become widely known as the 'bio-heat transfer' BHT equation:

$$\rho c\frac{\partial T}{\partial t} = \nabla \cdot k\nabla T + q_m + \left(\rho c\right)_b \omega_b \left(T_a - T\right). \tag{2.2}$$

In conditions such as the human forearm, this functions as a directionless heat source; in heat treatments, this term functions as a directionless heat sink.

2.3.2 Pennes' model weaknesses and alternatives

Pennes' bio-heat equation is the most widely used model in the literature, however there have been several alternative models proposed to replace Pennes' model in addition to revisions and adaptations of Pennes' equation. One of the earliest major critics of Pennes' paper was Wulff in 1973 [140]. Wulff drew attention to four problems with the unsimplified form of Pennes' equation (Equation 2.1):

1. Local and global control volume systems are combined – energy storage, diffusion and generation represent a net deposition of heat at a specific location whereas the 'global' perfusion term models heat exchanged with blood on a global basis (over the total temperature change of blood accomplished during travel through the tissue).

2. The equation implies three media each with a different temperature (T, $T_{b,in}$, and $T_{b,out}$) simultaneously occupying the same point in space. Separate equations for the time varying blood temperatures are neither included nor made reference to.

3. Pennes' equation fails to represent the fact that blood is in motion and may convect heat in any direction, regardless of the local temperature gradient.

4. The equation also fails to account for the fact that the driving potential of heat transfer between stationary tissue and fluids is, in general, the difference between tissue and fluid temperatures, rather than the difference between two blood streams.

Wulff proposed an equation similar to that of Pennes, with a different derivation:

$$\left(\rho c\right)_t \frac{\partial T}{\partial t} = \nabla \cdot k \nabla T - \left(\rho c\right)_b \vec{V}_b \cdot \nabla T + q_m, \tag{2.3}$$

where $\vec{V}_b$ is the 'local mean apparent blood velocity'. The crucial difference in Wulff's equation is that, unlike Pennes' equation, energy is conserved; as the advection term removes heat from one finite volume, it is introduced to surrounding volumes. Whether supported by experimental data or not, Wulff's equation at least obeys the laws of physics.

2.3.3 Counter-current artery-vein pair models

It is well established from anatomical observations of various biological tissues that for each artery there exists a corresponding vein which serves to remove the blood delivered by the artery. Relative to their length, the arteries and veins in such pairs are frequently spaced close to each other. Due to their shared purpose, the flows in artery-vein pairs are in opposite directions; using heat-exchanger terminology this flow regime is referred to as counter-current. This artery-vein pairing is also present in smaller vessels — arterioles and venules. It is believed that this architecture functions as a thermal control mechanism. In cold conditions where blood returning from extremities or skin surfaces is below body core temperatures, heat is transferred from artery to vein such that returning blood is heated and thereby closer to body core temperature. Further, the arterial blood loses heat and is closer in temperature to the extracorporeal environment. Since the rate of heat transfer is proportional to temperature difference, a lower temperature of arterial blood flowing to extremities results in less heat lost to the surroundings and therefore less heat lost in general from the vascular system. This pairing doubly protects the body from thermal shock. Conversely the artery-vein pairing functions as a protective control mechanism where the external temperature is above a desirable level [17].

Separately and concurrently to the work by Klinger [62], investigations were carried out by Mitchell and Myers [82], amongst others, into heat exchange between

counter-current artery-vein vessel pairs. Although peripherally interesting, the derived results are not presented here as the liver is a well-perfused tissue and no consideration of tissue conductivity is made, furthermore the derivations assume constant blood flow. It is important to accommodate varying blood flows as tissue and blood vessel properties undergo changes during cell death and as previously explained, blood flow rates vary across different pathological conditions in the liver.

With Pennes' equation describing mixed flow capillary beds and models such as Mitchell and Myers describing heat flow from pairs of vessels, it is clear that different regions of tissue require different analyses and models depending on whether they are proximal to or remote from vessels. In the vicinities of major vessels, in particular in regions between vessel pairs, the thermal effects of the vessels are dominant as perfused blood flow is relatively low. Conversely, in areas remote from major vessels perfusion can be considered to be high and the major vessels have relatively little impact. Much of the remaining literature considers multiple regions of tissue and, reaches conclusions based upon the various authors' assumptions.

Keller and Seiler [60] include counter-current heat transfer as with Mitchell and Myers but additionally consider the transfer of energy to the surrounding tissue. The issues raised by Wulff are not addressed in that the hypothetical capillary 'pool' is used as in Pennes' model, and as such the sink causes a disruption to the principle of conservation of energy.

2.3.4 Chen and Holmes Model

Possibly the most significant paper since the work of Pennes describes the work carried out by Chen and Holmes [15]. In their work, they define the thermal equilibrium length of a vessel as the length at which the temperature difference between blood and tissue is reduced to $1/e$ of its initial value (assuming the blood is well

mixed within the vessel and thereby the blood temperature is invariant with radius). There is also the assumption that convective heat flow mechanisms are dominant over conductive heat transfer mechanisms. The resultant blood temperature within a vessel is given by:

$$\pi r^2 \left(\rho c\right)_b v \frac{dT_b}{ds} = 2\pi U r \left(T - T_b\right), \tag{2.4}$$

where r and s are respectively the radius of the vessel and the axial position along it, v is the local blood velocity, and U is the local overall heat transfer coefficient across the vessel wall (assumed to be thin). Thus the equilibrium length l_e is:

$$l_e = \frac{r\left(\rho c\right)_b v}{2U}. \tag{2.5}$$

Chen and Holmes then defined the total heat transfer resistance $1/U$ to be the sum of the thermal resistances in the solid tissue (RES_t) and in blood (RES_b):

$$\frac{1}{U} = RES_t + RES_b. \tag{2.6}$$

Solutions for heat transfer resistances through blood and through tissue were found in cylindrical co-ordinates using D as the characteristic length representing the heat transfer path length. Chen and Holmes used one half of the mean distance between the centrelines of two vessels to be the heat transfer path length. The resistances were thus found to be:

$$RES_t \approx \frac{r \ln\left(D/r\right)}{k_t}, \tag{2.7a}$$

$$RES_b = \frac{1}{\mathrm{Nu}} \frac{r}{k_b} \tag{2.7b}$$

where k_t and k_b are the thermal conductivities of tissue and blood respectively and Nu is the Nusselt number.

Using work by Kays [58] for steady state laminar flow of a Newtonian fluid in cylindrical pipes ($\mathrm{Nu} = hD/k = 2$ where h is the convective heat transfer coefficient, and k is the thermal conductivity), and typical anatomical dimensions of vascular

beds ($D = O(10r)$ and $k_b = O(k_t)$), Equations 2.7a and 2.7b suggest that RES_t dominates and hence:

$$U = \frac{1}{\Lambda}\frac{k_t}{r}, \tag{2.8}$$

where Λ is a coefficient determined by solutions of the detailed heat conduction equations. Λ is dependent upon k_b, k_t, v, and the geometry of the vascular bed in question (D and r). The authors suggest $\Lambda \approx 3$ by alluding to typical values of D/r and k_b/k_t. Thus, Chen and Holmes provide an expression for the equilibrium length of vessel j:

$$l_{e,j} = \frac{\Lambda}{2}\frac{(\rho c)_b v_j r_j^2}{k_t}. \tag{2.9}$$

From this, Chen and Holmes calculated equilibrium lengths for the whole range of vessels in the human body, from the aorta down to the capillaries and back up to the vena cava. The values of equilibrium length found span many orders of magnitude. Most significantly it was found that the vessels with equilibrium length of order their actual length are a set of intermediate vessels with radii of approximately 0.1–0.25 mm. The implication is that these arterioles are the vessels across which heat transfer takes place, not the capillaries as previously postulated by Pennes. Indeed, Chen and Holmes' equilibrium length analysis adduces that the flow in vessels shorter than their equilibrium lengths (large vessels with high velocities) passes through tissue without significant change in temperature. Conversely, vessels a few branching generations higher than capillaries, with short equilibrium lengths, reach complete thermal equilibrium with the surrounding tissue along their length and thus blood enters the capillary network bed already near equilibrium and therefore little heat transfer occurs at the capillary level. Chen and Holmes produced a schematic plot of blood temperature as it traverses the systemic circulation, as shown in Figure 2.2.

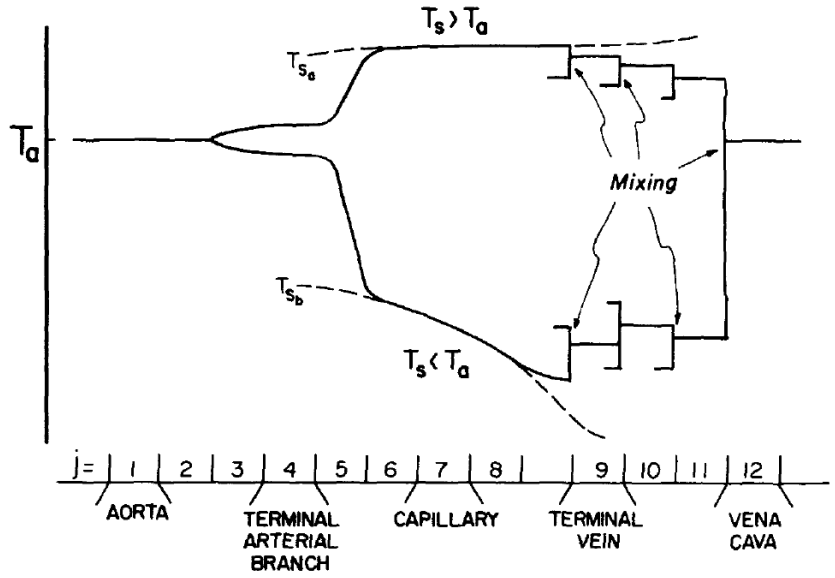

Figure 2.2: Schematic representation of the blood temperatures as the blood traverses the systemic circulation. Blood at arterial temperature (T_a) is distributed to solid tissues that are warmer (T_{s_a}) and cooler (T_{s_b}). Blood temperature rapidly equilibrates with T_{s_a} and T_{s_b} after leaving the terminal arterial branches, attaining the solid tissue temperature (T_s) prior to entering the arterioles ($j = 6$). Beyond the venules ($j = 8$), major changes in temperature are the result of mixing at venous confluences. Mixed vena cava blood will return to the heart at essentially the arterial temperature. Taken from Chen and Holmes 1980 [15]

Chen and Holmes then evaluated the microvascular contributions to heat transfer and concluded that:

1. Heat transfer from vessels larger than the terminal arterial branches and the precapillary arterioles should be calculated individually, not as part of a continuum.

2. Heat transfer in the perfusion term should consider the temperature of the blood leaving the last individually considered large vessel.

3. Microvasculature blood flow contributes to heat transfer with an additional term proportional to the local blood perfusion velocity.

4. Microvasculature blood flow affects the local thermal conductivity.

Chen and Holmes thus provided a revised bio-heat transfer equation:

$$\rho c \frac{\partial T}{\partial t} = \nabla \cdot k \nabla T + \omega_j^* \left(T_a^* - T \right) - \rho_b c_b \vec{V}_b \cdot \nabla T + \nabla \cdot k_p \nabla T + q_m, \tag{2.10}$$

where ω_j^* and T_a^* are the volumetric volume flow rate and temperature of blood exiting vessels of the j^{th} branch, and k_p is the local thermal conductivity due to perfusion effects.

The equilibrium length used by Chen and Holmes has been the focus of many subsequent papers; among others Chato [13] analysed vessel configurations with various geometries and reached the conclusion that vessel size is the most significant factor in determining thermal significance. In support of Chen and Holmes, large vessels are shown to be minimally affected by surrounding tissue and small vessels are almost in complete equilibration with the surrounding tissue. Despite detailed mathematical analysis, results regarding intermediate vessels remain inconclusive. Weinbaum *et al.* [135] also focused on a few specific vessel configurations and produced results that similarly support the work of Chen and Holmes. Baish *et al.* [4] furthered the analysis using regions of different equilibrium length and also suggested that large vessels operate as heat sinks for the proximal tissue zones. For regions where the equilibrium length is equal to the vessel length, Baish *et al.* proposed the use of a model using a Green's function approach that incorporates vessel-vessel heat exchange in addition to the equations for the surrounding tissue.

2.3.5 Weinbaum-Jiji models

Another significant approach is the Weinbaum-Jiji-Lemons (WJL) model [55]. Similar to the work of Keller and Seiler [60], the approach uses a three equation model. In addition to an equation describing the tissue temperature, a three equation model

contains equations concerning the volume of blood in the arterial tree and the volume of blood in the venous tree. The three equations contain terms representing the transfer of thermal energy from their respective volumes to one or other of the volumes, thus creating a model of three simultaneous differential equations. In the WJL model the vascular generations considered are those of thermally significant vessels and not of the large supply vessels. In their analysis, equilibrium lengths were first recalculated by the authors for thermally significant vessels, as the equilibrium lengths reported by Chen and Holmes [15] were only estimated (Λ in Equation 2.8 was suggested to be ≈ 3 based upon estimated calculations).

An assumption made in the derivation of the WJL model is that the volume of bleed off blood (the blood that flows from the counter-current pair of vessels, to the deeper layers of muscle tissue) is at venous temperature – something disproved by numerous experiments and the subject of several critics, most notably Wissler [139]. In later work, Weinbaum and Jiji revised the WJL model in an effort to produce a model that would be simpler to implement [134]. The simplified model requires assumptions such as that the mean tissue temperature can be replaced by the average temperature of artery-vein pairs when nearly equilibrated. The simplified Weinbaum-Jiji (WJ) model is more practical for numerical implementation.

2.3.6 Heat Transfer Models Summary

Since the work of Chen and Holmes there have been many publications investigating specific vessel configurations, geometries, densities and particular branching generation distributions. In each author's analysis, various assumptions are made to achieve a novel adaptation to either Pennes' original BHT equation, or to the Chen and Holmes model. In almost all cases, these various assumptions are the target of criticism in subsequent reviews. The result is a great number of papers

covering heat transfer in biological tissue, yet little development along a single line of analysis. The field post Chen and Holmes appears to have spread in breadth, but without major progression.

The principal reason for the abundance of sometimes subtly different heat transfer models is the difficulty of obtaining conclusive experimental data. Fundamental to evaluating a particular model is knowledge of the anatomical construction of the section of tissue being tested; the semi-hierarchical branching nature of blood vessels results in a non-discrete distribution of vessel size, and as such determining the thermal significance of each vessel tier is near impossible. Additionally, the variation between different tissue, and indeed between different tissue samples, is such that no two samples that could be used for testing are the same. Further, the size of vessels thought to be the most thermally significant is beyond the lower resolution limit of the majority of imaging techniques, whereas the geometries of larger veins and arteries span too large a distance for microscopy techniques, thus also making mapping the vessel architecture very challenging.

2.4 CELL DEATH

2.4.1 Physiological Processes to Death

In standard physiological understanding there are two modes of cell death: necrosis and apoptosis [50]. Necrosis is the premature death of cells caused by an external factor; in the case of RFA treatment, sustained temperatures that exceed the tolerance of the cell types is sufficient cause for cells to become necrotic. Such mechanisms that might directly or indirectly lead to necrosis include disintegration of the bilayers of the cell membrane, denaturation of the intracellular proteins, inhibition

of enzymes, and damage to ion channels and other cellular structures that exist in various different cell types [9] [19] [44] [70] [73].

In contrast, apoptosis is a naturally occurring process for cell death; it is a programmed path to cell destruction that is selected as a result of biochemical events. With regard to RFA treatments, apoptosis occurs as a result of changes in the biochemistries of both the cell in question and of the surrounding cells and tissue. During the procedure of RFA treatments a third method of cell death – carbonisation – also frequently occurs.

Carbonisation is a phenomenon specific to sudden and high temperature heating common in tissue during RFA. Under violent heating conditions, the organic matter of the cells is converted into carbon or a high-carbon residue. In RFA treatment, carbonisation is often present only in the immediately proximate area around the treatment needle tips. For a review that describes the physical effects of thermal damage, see that by Pearce [97] which also details some of the more common models for cell death, and corresponding parameter values from the literature.

Important to note is that normal adult body temperature is 37 °C and whole-body temperatures of 40 °C are life threatening with brain death occurring above 41 °C and guaranteed death above 45 °C. As a result, much of the literature on cell death from heating that deals with hyperthermic conditions includes only models that account for cell death at temperatures between 37 °C and 43 °C, and heating times in the order of hours. In comparison, RFA and other thermal ablation treatments heat violently with local temperatures exceeding 100 °C – the commercially distributed RITA protocol used by radiotherapist collaborators at the Medical Universities, Leipzig and Graz, sets a target temperature of 105 °C at needle tips for a heating time of 10 minutes.

These ultrahyperthemic conditions that exist in thermal therapies (times of the order minutes and temperature rises of the order 50 K and more) are so significantly different from the clinical problem of whole-body hyperthermia that the following literature review is restricted to primarily focus upon cell death models capable of accommodating these ranges of variables. More precisely, models that have been *implemented* with these variables values are reviewed below. Superficially, and ignoring secondary effects such as electric field influences (RFA) and acidosis (direct current), all thermal ablation treatments are designed and implemented to kill cells via the deposition of heat and thus most models for predicting cell death require variables of temperature and time only. The review below reflects this and is focussed upon all such models regardless of the specific thermal ablation therapy their authors were most interested in.

2.4.2 Discrete Threshold Model

The simplest model possible uses a single temperature threshold above which cells are instantaneously declared dead, and below which cells remain fully functioning [22]. Computationally by far the most simple model, these isotherm models have no ability to take account of the duration for which cells are at elevated temperatures. A commonly used threshold temperature is 55 °C, with such a model any cell that is brought to a temperature of 55 °C for any duration will be deemed effectively destroyed, yet a cell held at even 54.9 °C for a period of days would remain in the alive state. Thus, despite the minimal computational effort required, the model is of little use for any serious prediction of thermally induced cell death.

2.4.3 Theoretical Models

As a precursor to explaining and evaluating the literature of models describing cell death, the Arrhenius equation is explained. In 1889 the Swedish chemist Svante Arrhenius published his work on reaction rates of chemical reactions. Based upon data from several third parties, Arrhenius investigated the temperature dependence of reaction rates. He concluded that all reactions have a rate equation which is dependent upon the concentrations of the reactants and/or products and the rate of reaction, k. Arrhenius defined this as:

$$k = Ae^{-E_a/RT}, \tag{2.11}$$

where A is the probability of the reaction, E_a is the activation energy of the reaction, R is the molar gas constant, and T is the temperature (in Kelvin) at which the reaction takes place. The importance of the Arrhenius equation is evident when the literature of mathematical models of cell death is examined. There exist three principal groups of papers on cell death: those fitting the Arrhenius equation to experimental data and evaluating A and E_a, those utilising the Arrhenius equation in the derivation of a result to a more complex mathematical model, and those not assuming that the Arrhenius equation holds true for cell death and instead using an alternative equation for the rate constant. Of the three groups, the third contains the least literature.

2.4.4 Arrhenius Equation Models

Henriques and Moritz were the first to implement the Arrhenius equation for cellular damage when in 1947 they proposed applying the temperature-dependent Arrhenius law for chemical reaction rates to cutaneous skin burns [52] [83] [84]. This use subsequently dominated the field of cell death and although limitations exist

with Arrhenius based models, it has become the yardstick by which other models are compared and contrasted.

The two main limitations of such Arrhenius based models are firstly that the two governing parameters are very sensitive to experimental values. The constant of proportionality is especially sensitive with reported values ranging over tens of orders of magnitude [97], requiring large safety margins. The second limitation is that cell survival rates for different temperatures show a marked discontinuity at temperatures around 43 °C, the exact temperature break depending upon species of origin and cell line [22] [111].

2.4.5 The Whiting, Dowden and Kapadia Model

For a model to predict lesion boundaries from hyperthermic killing from laser heating, Whiting *et al.* [138] start with the premise that if tissue held at a constant temperature T dies after time $\tau(T)$ then for varying temperature, tissue death occurs at time t_d where:

$$\int_{T>T_{min}}^{t_d} \frac{dt}{\tau(T)} = 1, \tag{2.12}$$

where T_{min} is the minimum temperature required for cell death to occur. Using existing evidence on conventional hyperthermia [23], [37], an expression for the dependence of τ upon temperature is given as:

$$\tau(T) = A\alpha^T, \tag{2.13}$$

where A is a constant parameter and α takes the value $\frac{1}{2}$ if T is measured in °C. The above equations are used to define a function for cell viability A:

$$A(\alpha, T_\infty) = \ln \int_{T>T_{min}}^{t_d} \alpha^{T_\infty - T}\, dt, \tag{2.14}$$

where T_∞ is the temperature the tissue ultimately would reach if a steady state were to be achieved. The authors use 2.14 to show that $\alpha = \frac{1}{2}$ is unsuitable to model cell

death regardless of the selected corresponding value of τ. Plots are made against experimental data with best fit curves of A with $\alpha = \frac{1}{2}$. The authors then create a best fit line using least squares regression and conclude that an improved value would be $\alpha = 0.723$. The corresponding value of the time parameter for the best fit line is $\tau\,(46) = 3\,\text{min}\ 11\,\text{s}$, which the authors note is significantly different from standard hyperthermic values of τ — typically 7–10 minutes. The conclusion is drawn that the value of $\alpha = \frac{1}{2}$ was originally formulated for necrosis in a small range of temperatures and that their analysis has shown it is not suitable for application to higher temperature heating.

2.4.6 The Sapareto and Dewey Model

The concept of a thermal dose starts with the premise that if tissue held at a constant temperature T dies after time $\tau\,(T)$, under the correct transformation, heating times at other temperatures can be converted to equivalent minutes at 43 °C. This transformation was proposed in 1984 by Sapareto and Dewey [112] based on earlier experimental work [113] [114]. The expression for equivalent heating time at 43 °C is shown in Equation 2.15 where t_i and T_i are the heating time and heating temperature and α is a constant which is set to 0.5 for heating at temperatures above 43 °C and 0.25 for heating at temperatures below 43 °C:

$$t_{43} = \alpha^{43-T_i}\, t_i. \tag{2.15}$$

Sapareto and Dewey only deal in discrete, single temperature heating epochs; however a continuous form of Equation 2.15 which can be used for dynamically varying temperatures was derived by Whiting [138] based on different experimental data [23] [37]. They note that analysis of the cells killed by thermal treatments shows a ‘marked departure from the rule used in conventional hyperthermia to determine

the region treated'. In particular temperatures above 55 °C cause the greatest deviation from the standard model. Modern thermal treatments, however frequently involve significant regions of tissue exceeding 55 °C, with needle tip temperatures reaching 105 °C or higher [47].

2.4.7 The Uchida Model

Uchida *et al.* [125] note that plots of cell viability exposed to high hyperthermic temperatures [137] ($T > 43\,^{\circ}\mathrm{C}$) have traits similar to survival curves as functions of radiation – most significantly, the presence of a shoulder region before a monotonic decrease in viability. The authors use the similarity of these plots to suggest an analogy to cell death caused by radiation; the hypothesis is that death from hyperthermia is the result of an accumulation of sublethal damage. The model then derived uses the premise that the tail of the survival curve unique to hyperthermic heating below 42.5°C is due to thermotolerance [43], and it is postulated that the cause of thermotolerance is continual repair of the sublethal damage caused during heating. The authors follow the proposition of Connor *et al.* [18] to calculate the 'inactivation energy' (E_a) from Arrhenius' equation (2.11). In the analysis, Uchida *et al.* make the substitution:

$$\beta = \ln(A), \tag{2.16}$$

and evaluate the constant β from the data of Sapareto [113]. The derivation continues with the expression for probability that the cell will be damaged m times during a period of heating t. This probability (W) is given as:

$$W(T,0,t,m) = \frac{\left[\int_0^t e^{(-E_a/RT+\beta)\,dt}\right]^m}{m!} e^{\left[\int_0^t e^{(-Ea/RT+\beta)\,dt}\right]}. \tag{2.17}$$

A similar expression for the probability of a cell damaged m times not being to able repair itself in the damage repair time t_{rc} is given as:

$$W(T, t-t_{rc}, t, m) = \frac{\left[\int_{t-t_{rc}}^{t} e^{(-E_a/RT+\beta)dt}\right]^m}{m!} e^{\left[\int_{t-t_{rc}}^{t} e^{(-E_a/RT+\beta)dt}\right]}. \tag{2.18}$$

To fit the experimental data used, Uchida et al. select an arbitrary function for t_{rc}:

$$t_{rc} = t_0 + \int_0^t \sin(T - T_0)\, a t^b |T - T_0|^c \, dt \tag{2.19}$$

where t_0 is the start time of heating, T is the temperature of heating, T_0 is the critical temperature (the authors use $T_0 = 42.5\,^{\circ}\mathrm{C}$), and a, b, and c are three constant parameters.

This model fits the data of Sapareto [113] well and indeed accommodates the existence of the observed 'shoulder region'. However, the choice of the arbitrarily selected function for t_{rc} is not fully explained, which is an obstacle to using the model for further mechanistic understanding of cell death. One of the other significant limitations of the model is that it requires a large number of parameters which need to be optimised by the data fitting.

2.4.8 The Chen and Saidel, and the Breen Models

A model distinct from those mentioned above, is the one used by Chen and Saidel [16] in their investigation into predicting lesion boundaries for RFA treatments. The model for tissue damage depends upon the local temperature history:

$$A(t) = e^{\left[-\int_0^t \beta[T(\tau)]d\tau\right]}, \tag{2.20}$$

where A is the fraction of cells alive at time t, τ is the heating time, t is the time at which the cell viability is calculated and β is the damage rate which the authors

arbitrarily define as:

$$\beta[T] = \begin{cases} 0, & T(t) < T_c \\ \beta_0 [T - T_c]^{1.1}, & T(t) \geq T_c \end{cases}, \tag{2.21}$$

where β_0 is a constant damage rate coefficient and T_c is the critical temperature for protein denaturisation (the authors use $T_c = 42.5\,^{\circ}\mathrm{C}$). A point that is unclear in the paper is the value of the exponent, in Equation 2.21 shown to be 1.1, however in the text mention is made of "the square of temperature above a critical level T_c".

The work by Chen and Saidel was the follow up and simplification to a series of papers by Breen *et al.* [12] which aimed to produce a simple empirical model to predict cell death from MRI thermometry images. The original model included the parameters β_0 and T_c as with the simplified model but did not set a value for the exponent, instead leaving it as a parameter (N) to be decided from data fitting. Breen *et al.* also included a second part to the cell death model; they introduced a threshold for determining the final model output M. The model output which can be 0 or 1 represents two cell states, Alive and Dead respectively. The damage threshold governs the model output as:

$$M = \begin{cases} 0, & \Omega(t) < \Omega_c \\ 1, & \Omega(t) \geq \Omega_c \end{cases}, \tag{2.22}$$

where Ω is the accumulated destruction of tissue at time t, and Ω_c is a critical threshold value. For the purpose of validation for their model, Breen *et al.* compared their cell model output with known cell states from histological images. Each cell was accounted for once in one of four numbers: N_{TP}, N_{TN}, N_{FP}, or N_{FN}, which respectively denote the cell numbers of true positives, true negatives, false positives and false negatives. An objective function was created of the form:

$$f = W N_{FP} + (1 - W) N_{FN}, \tag{2.23}$$

where W is an adjustable weighting factor depending on the requirements of the model fit (or degree of conservatism). The authors then continued the data fitting exercise minimising f for four values of W — (0.50, 0.70, 0.85, and 0.95) — and published the corresponding minimising parameters. In the discussion, Breen *et al.* note that an absolute minimum was achieved with $W = 0.85$.

Whilst this may result in the closest numerical fit of the model to the data, it should be noted that modifying W in this way is not justifiable. If $W = 0$ were found to produce the best numerical fit and therefore used, then the weighting function would include no consideration for false positives. This would be in direct opposition to the priorities of clinicians whose highest priority is to be sure of fully ablating a tumour. Complete certainty of the destruction of cancer cells requires that no cells are thought to have been killed yet remain viable. A high degree of conservatism is necessary when treating cancer; as such the value of W should not be determined by the best quantitative fit to the data but rather by an expert clinician based upon clinical priorities.

2.4.9 The Jung Model

Another model based upon the same assumption that following the accumulation of sublethal lesions, one lesion becomes lethal and causes cell death is that proposed by Jung [57]. Jung outlines a compartment model where the compartment $S(n)$ contains the population of surviving cells that have n nonlethal lesions. The model has two reaction mechanisms; firstly when an alive cell with $n-1$ lesions has a single additional lesion created in it, it transitions irreversibly from the state $S(n-1)$ to the state $S(n)$. The rate constant of this transition is denoted as p which is assumed to be invariant with respect to time and independent of the number of nonlethal lesions already present in a cell. The second reaction mechanism ac-

counts for the transition from the alive state to the dead state. This is assumed to be constant with time and independent of the number of nonlethal lesions already present in the cell; the rate constant for this is denoted as c. Thus for each compartment $S(n)$ (other than the compartment when $n = 0$ and the compartment accounting for dead cells), there is one influx from compartment $S(n-1)$, Equation 2.24a, and two effluxes, one to compartment $S(n+1)$, Equation 2.24b, and one to the compartment of dead cells, Equation 2.24c:

$$\text{influx from } S(n-1) = p \cdot P(n-1), \tag{2.24a}$$

$$\text{efflux to } S(n+1) = p \cdot P(n), \tag{2.24b}$$

$$\text{efflux to death} = n \cdot c \cdot P(n), \tag{2.24c}$$

where $P(n)$ is the probability for a cell being in compartment $S(n)$. The change of $P(n)$ with respect to time is thus given as:

$$\frac{dP(n)}{dt} = p \cdot P(n-1) - p \cdot P(n) - n \cdot c \cdot P(n). \tag{2.25}$$

The equation for the change of $P(0)$ with respect to time is given as:

$$\frac{dP(0)}{dt} = -p \cdot P(0). \tag{2.26}$$

Using the initial conditions:

$$P(n) = \begin{cases} 1, & n = 0 \\ 0, & \text{otherwise} \end{cases}, \tag{2.27}$$

the solution for the system is found to be:

$$P(n) = \left(e^{-pt}\right) \frac{\left\{\frac{p}{c}\left[1 - e^{-ct}\right]\right\}^n}{n!}. \tag{2.28}$$

The surviving fraction of cells at time t is clearly:

$$S(t) = \sum_{n=0}^{\infty} P(n), \tag{2.29}$$

which the author uses to create the expression for cell viability at time t:

$$S(t) = exp^{\{\frac{p}{c}[1-ct-e^{-ct}]\}}. \tag{2.30}$$

After investigations into 'step-up' and 'step-down' heating (respectively heating at a low temperature initially followed by a higher temperature, and the reverse) involving temperatures from 39 ° to 45 °, Jung comments that this model explains corresponding cell viability plots. He notes that at the lower temperature fewer lesions are created (lower rate constant p), but the rate constant for a lesion becoming lethal (c) is unaffected. Step-up heating has little affect on final cell viability as the majority of lesions are created at the higher (second) temperature and only once created can the lesions become lethal. Step-down heating does however have an effect, as at the lower temperature (second) there exist many nonlethal lesions created at the higher temperature, and thus cell viability continues to decrease in the second section of step-down heating. Jung then examines the frequency distribution of nonlethal lesions; no significant conclusions are drawn but this form of analysis may elucidate the degree of thermal tolerance exhibited by cells under certain heating conditions.

The significant disadvantage with the model proposed by Jung is that as used, the parameter p contains no dependance upon temperature and thus assumes single temperature heating for the duration of the heating period. The author provides a subsequent derivation for successive heating at a second fixed temperature but the mathematics are significantly more complex and would not be suitable for heating at varying temperatures. Were Jung's model to have rate constants p and c that included a temperature dependence, such that they could be used for dynamic heating profiles, Jung's model would be of significantly greater use in cell death prediction; due to the complex mathematics and the theoretical possibility of an in-

finite number of states, however, implementation would necessarily be numerical with a truncated number of states.

2.4.10 Other multi-compartment models

In terms of mechanistic insight, models containing three or more compartments hold significant potential advantage over standard two state models whist avoiding the undesirable nature of models comprising of an infinite number of compartments. Breen *et al.* [12] propose such a three state model where cells are first moved to an intermediary state, a process which is reversible, before then suffering fatal, irreversible damage. Similarly Szasz and Vincze [123] incorporate an 'excited' state between intact and lethal states.

Aside from the models discussed above, it should be noted that there exist a number of statistical models which originate in the field of radiation. Fowler [40] clarifies the applicability of the single-hit, multi-target and the multi-hit, single-target models and Roti and Henle [110] make a comparison to the linear-quadratic. Although statistical models can be shown to fit experimental data, their statistical nature limits insight into mechanistic events.

It must be mentioned that the majority of the literature deals with first order reaction kinetics. Higher order models that are more intricate and complicated could be used; as Dienes [24] notes, "there is no conceptual difficulty in introducing bimolecular, or higher-order, reactions".

2.4.10.1 The Landry and Marceau Model

Early multi-compartmental modelling — dating from 1978 — was done by Landry and Marceau [66]. Starting out from a two-compartment, one-step model, the authors identify the primary issue with such models: that the resultant reaction equa-

tion “cannot fit the cell-survival-response curve to hyperthermia obtained over a wide temperature range". They also note that recovery from neither “sublethal nor potentially lethal damages" is not possible. Instead, the authors suggest use of a three-compartment, two-step model, or a four-compartment, three-step model; the main reason given for not progressing to a higher level model is that of the analytical complexity that would ensue.

2.4.10.2 The Feng Model

Recent work by Feng *et al.* was carried out to find a model that fitted a feature of experimental data [22], [111] unaccounted for in most previous models. Feng *et al.* noticed two transitional temperatures or ‘break points’ at approximately 43 °C and 54 °C. They suggest that these ‘break points’ might represent different damage mechanisms which come into play at and beyond these temperatures. They criticise the use of a single Arrhenius equation as although it can be fitted to the exponential drop-off in cell viability, it does not accommodate the ‘shoulder region’ exhibited in the early stages of heating at low temperatures. The authors acknowledge that a reasonable fit can be made by examining the data in three separate temperature regimes ($T < 43\,^{\circ}\text{C}$, $43\,^{\circ}\text{C} \leq T \leq 54\,^{\circ}\text{C}$, and $T > 54\,^{\circ}\text{C}$), but they assert the desire for a single unified model. Feng *et al.* proposed a two state model where all cells in the total population can be separated into two distinct states — Alive and Dead. Rather than create a reaction mechanism, the authors simply propose a expression for cell viability as a function of heating temperature (T) and heating time (τ):

$$A(\tau, T) = \frac{e^{-(\gamma/T + \alpha\tau + \beta)}}{1 + e^{-(\gamma/T + \alpha\tau + \beta)}}, \tag{2.31}$$

where A is the fraction of cells in the Alive state, whilst γ, α and β are parameter constants to be set in fitting the model to data. The paper concludes with estimations of these parameters from a data fitting exercise.

2.4.11 Cell Death Models Summary

In the literature there exist many cell death models that can be attributed to a number of distinct model fundamentals. A large proportion of models in the literature are based upon the assumption that cell death behaves as any simple chemical reaction and thereby require use of the Arrhenius equation to determine rate equations. The main issues that arise from this assumption have been raised above. Of the models that avoid use of the Arrhenius equation, many create an empirical equation to fit a set of experimental data rather than start from a position of first principles or examination of fundamental biological processes.

Due to historical reasons, the majority of the literature deals with naturally occurring hyperthermia where temperatures rarely exceed 43 °C. This is a distinct modelling scenario from predicting cell death from thermal ablation therapies where temperature rises are typically greater by an order of magnitude (60 °C compared to 6 °C). A number of authors acknowledge this fact by suggesting the use of discontinuous models which take different formulations for temperatures above, or below, a critical temperature — most frequently 43 °C.

The small section of the literature that investigates higher hyperthermic temperatures include a relatively wide range of proposed models, none of which have successfully achieved wide-spread use. The main obstacle to the success of any one model is the variance between experimental results; data from one experimental combination of cell line and heating regime frequently cause model parameters to vary widely and unpredictably. The latter is the greater issue because a model without predictable parameter values is of little use for clinical predictions.

In summary, in reviewing the literature, several important requirements for a cell death model have been identified:

- The model should fit the data continuously both above and below the transitionary temperature of 43 °C;
- The model should be dynamic in time, able to predict the instantaneous rate of cell death;
- The model should fit multiple sets of data with consistent, or predictable, parameter values.

By adhering to these criteria, any novel model for predicting cell death will not only be simple to comprehend and implement (criterion 1), but also hold distinct advantages for over existing models in the literature as far as the end user — typically a clinician — is concerned, due to the flexibility of such a model permitting it to be applied to a similar, but unique modelling scenario (criteria 2 and 3).

2.5 HEPATOCYTE MODELS

For hepatocytes to perform the tasks required for the liver to function correctly, a steady-state behaviour of the hepatocyte that maintains the correct balance between intracellular and extracellular ion concentrations and water potentials is particularly important. As noted by Kolb and Adam [65], ion transport processes are important to ensure correct control of osmotic processes and of basic metabolic functions.

Many equations that govern the behaviour of both passive and active transport of ions across the cell membrane involve a dependence upon temperature, often in the following (or related) form:

$$exp\left(\frac{ve}{kT}\right), \tag{2.32}$$

where v is a potential, e is the elementary charge, k is Boltzmann's constant, and T is the temperature. This form stems from the Arrhenius equation, where in this instance, the activation energy E_a is modelled as the product of a relevant potential and the elementary charge. As a direct result of the inclusion of this form, the equations that are used to model ion transport are often complex and highly nonlinear producing potentially complex relationships between cell temperature and status.

Much work has been done to model transport mechanisms such as ion gates, co-transporters, and exchangers; many of which are presented in detail by Keener and Sneyd [59]. The complexity of any modelling in this area is such that controlling the model to behave as required is a highly intricate task due to inherent non-linearities. Due to the difficulty of this modelling scenario, most of the modelling efforts both historically and today have been in cardiac or nervous system electrophysiology. As a result, the literature is very sparse with respect to models of hepatocytes at the ion-channel and cell-membrane level.

A clinical observation that often occurs during, or after, thermal ablation therapies is a hyperdense annular shell at the periphery of the ablation volume. Detectable though contrast-enhancement CT, or as a hyperechoic region in an ultrasound image, the volume occurs inside, at the edge of, or immediately outside the ablated tissue [72] [77] [126]. If it were possible to determine the correlation between the edge of the ablation and this hyperdense rim, then clinical observations of such a rim could have profound use as a method of determining final ablation volumes in real time. A hyperdense region may occur as the result of an influx of fluid, perhaps due to the alteration of the osmotic equilibrium; thus determining ion fluxes, intra- and extracellular volumes may provide a model tieing these observations and phenomena together.

2.5.0.1 Nernst Potential

Related to Equation 2.32, is the derivation of the Nernst equilibrium potential, first proposed by Nernst in 1888 [89]. The equation provides an expression for the electrical potential required to set a zero flux between two volumes with a non-zero concentration gradient. The Nernst potential, υ, for a particular species X can be expressed as:

$$\upsilon_{\mathrm{X}} = \frac{kT}{Ze} \ln \frac{\left[\mathrm{X}^{Z}\right]_{e}}{\left[\mathrm{X}^{Z}\right]_{i}}, \tag{2.33}$$

where k is the Boltzmann constant, T is the temperature in Kelvin, Z is the valence of the species, e is the elementary charge, and the subscripts e and i denote the extra- and intracellular nature of the ions. Such expressions determine the driving forces for the cross-membrane flux of ions and, as such, are fundamental to models of ion transport.

2.5.1 Melkikh and Sutormina Model [81]

A significant paper by Melkikh and Sutormina presents a model of mass transport specific to a hepatocyte. Other work by the authors has developed a more generalised theory for mass transport across various cell membranes [80] [79].

The model presented in this paper aims to track the resting potential of the cell membrane and with it, the concentrations of four different ions. The specific ions modelled are the cations of sodium and potassium, and the anions of chloride and carbonate — Na^+, K^+, Cl^-, and HCO_3^- respectively. The authors use only these four species as they are the ions that "play the basic role in forming the resting potential on the cell membrane". Known numerical values for the four concentrations of the species both in the intra- and extracellular volumes are given, along with the resting potential of the membrane.

The authors next present equations of the model via a process of "one ion – one transport" algorithm; whereby one species is selected (in this instance, chloride) and the distribution is solved for assuming that only the most important transport mechanism is responsible for the ratio of intra- and extracellular concentrations. For chloride, the authors assume that the ions penetrate the cell passively and therefore are determined solely by the Boltzmann distribution. The resultant value for intracellular chloride is close to the known value and the authors proceed to determine an equation for the next species, potassium ions.

Potassium ions, it is shown, cannot be modelled by the Boltzmann distribution, nor by assuming that the K^+/Cl^- symport is primarily responsible. By refusing to consider that active transport through the Na^+/K^+–ATPase active transporter is primarily responsible — because this mechanism will be required to predict the distribution of sodium ions — the authors utilise the following equation for the distribution of potassium ions:

$$\left[K^+\right]_i = \left[K^+\right]_e \exp\left(\Delta\mu_K - \frac{\upsilon_m e}{kT}\right), \tag{2.34}$$

where $\left[K^+\right]_i$, and $\left[K^+\right]_e$ are the intra- and extracellular concentrations of potassium ions, υ_m is the resting membrane potential, and $\Delta\mu_K$ is an artificially introduced factor which the authors explain as an "effective potassium EMF accounting of [sic] the sum action of pumps Na^+/K^+–ATPase, K^+/Cl^-, and passive flux through the membrane". This additional parameter is thus set such that the intracellular concentration of potassium fits the data.

The same parameter is subsequently used in an equation describing the distribution of sodium ions, which the authors assume to be overwhelmingly determined by the Na^+/K^+–ATPase pump operating in steady-state. With this condition of steady-state, the authors set zero flux for each ion. The resultant value for the intracellular concentration of sodium is 25 % lower than the data value of 29 mM.

The authors make two further assumptions in order to generate two further equations for the model. Firstly, a condition of intracellular electroneutrality is imposed such that the net charge of all considered intracellular species is zero; thus:

$$\left[Na^+\right]_i + \left[K^+\right]_i = [Cl^-]_i + \left[HCO_3^-\right]_i + Z_A\left[A^{-Z_A}\right]_i, \tag{2.35}$$

where $\left[A^{-Z_A}\right]_i$, the concentration of large anions that do not permeate the cell membrane are additionally considered. These ions have an averaged negative charge of magnitude Z_A and are thus multiplied by that factor in the equation.

Secondly, the authors note that the cell membrane of the hepatocyte, like many other cells, is not physically restrained by a cell wall and thus there must be a negligible pressure drop between the inside and the outside of the cell. An adverse pressure gradient would put the cell at risk of damage or death through membrane rupture. The result of this assumption is that the osmotic pressure contributions of the intracellular species must balance those of the extracellular species, thus the equation given is:

$$\left[Na^+\right]_i + \left[K^+\right]_i + [Cl^-]_i + \left[HCO_3^-\right]_i + Z_A\left[A^{-Z_A}\right]_i = \left[Na^+\right]_e + \left[K^+\right]_e + [Cl^-]_e + \left[HCO_3^-\right]_e. \tag{2.36}$$

However, the term Z_A should not be present in such an equation as ion valence is not valid in a consideration of osmotic pressure. The authors' subsequent step is to utilise the common occurrence of $\left[HCO_3^-\right]_i$ and $Z_A\left[A^{-Z_A}\right]_i$ in Equations 2.35 and 2.36 to eliminate these unknowns; a step which could have been unnecessary if an approximate value for Z_A was known and the given experimental concentrations were used together in order to calculate $Z_A\left[A^{-Z_A}\right]_i$.

Nevertheless, with the elimination (or knowledge) of $Z_A\left[A^{-Z_A}\right]_i$, a final expression for membrane potential can be derived which depends upon the extracellular ion concentrations, the parameter of the effective EMF of the Na^+/K^+–ATPase

pump and the parameter $\Delta\mu_K$. A value for the membrane potential is then determined which differs from the recorded value by 6%; the authors thus conclude that this "corresponds well to the experimental data". This is of no great surprise, because this is the product of a circular process where the experimentally recorded value for membrane potential was used to validate many of the equations that were subsequently used to 'calculate' the membrane potential.

Despite these mathematical issues, Melkikh and Sutormina's paper contains a number of useful concepts. The equation of the condition of intracellular electroneutrality is potentially important, as is the correct formulation of the condition of zero net osmotic pressure. Not only do the equations provide methods for eliminating variables, but they are both linear equations of simple summations and differences, and as such can be used for algebraic elimination of variables.

2.5.2 The Endresen Model [34]

The Endresen Model was created in an effort to model cardiac pacemaker cells. However, the authors first generate a more generic model for the membrane potential of a single cell, rather than the specific case of a cardiac pacemaker cell, hence it is detailed here. In fact, the model as initially presented requires subsequent modification to emulate a pacemaker cell.

Compared to the Melkikh paper, these authors more fully account for the intracellular concentrations of sodium, potassium and calcium by using five transport mechanisms for just three species: three separate single-species gates, the sodium-potassium pump, and the sodium-calcium exchanger. This final mechanism is an important mechanism for maintaining appropriate calcium concentration by extruding the calcium ions that flood in during periods of oscillations when calcium gates are open. The net energy change of this exchanger is deemed to be negligible

and it is thus dependent purely upon the membrane potential and the two Nernst potentials of sodium and calcium. The resulting exchanger current is given by:

$$i_{\mathrm{NaCa}} = k_{\mathrm{NaCa}} \sinh\left(\frac{e}{2kT}\left(v - 3v_{\mathrm{Na}} + 2v_{\mathrm{Ca}}\right)\right), \tag{2.37}$$

where k_{NaCa} is a constant of conductance to be determined by fitting the model. The hyperbolic sine form arises from an approximate model of the behaviour of the exchanger which the authors assume behaves in a similar manner to an ion gate, but without any condition of being 'open' or 'shut'.

In the Endresen model, the authors utilise the five ion currents to generate expressions for the instantaneous fluxes for each of the three species:

$$\frac{d}{dt}[\mathrm{K}]_i = \frac{2i_{\mathrm{NaK}} - i_{\mathrm{K}}}{FV}, \tag{2.38}$$

$$\frac{d}{dt}[\mathrm{Na}]_i = \frac{2i_{\mathrm{NaCa}} - i_{\mathrm{Ca}}}{2FV}, \tag{2.39}$$

and

$$\frac{d}{dt}[\mathrm{Ca}]_i = \frac{-i_{\mathrm{Na}} - 3i_{\mathrm{NaK}} - 3i_{\mathrm{NaCa}}}{FV}, \tag{2.40}$$

where F is Faraday's constant, and V is the volume of the cell which is assumed to be constant.

Endresen *et al.* conclude their model with a derivation involving the osmotic pressure term. However, this is taken no further as one assumption in the model is that the cell in question is of fixed volume, and this nullifies any osmotic effects. It is, nonetheless, worthwhile noting that were the Endresen model to be extended to accommodate cells of variable volume, then the osmotic pressure could be incorporated without conflict.

At no point in this paper do the authors acknowledge the presence of temperature in the majority of the equations, nor the assumption that temperature is a system constant. However, in a previous publication [35] that deals specifically with

resolving a known 'paradox' in the relationship between the voltage dependence of gate activation and the voltage dependence of the system dynamics, the authors make specific comments on the presence of temperature in the equations and the fact that, in this instance, it is assumed to be constant.

2.5.3 Hepatocyte Cell Models Summary

The current literature, is very sparse in the area of models specific to the cellular behaviour of hepatocytes. Whilst there exists a large number of models dealing with electrophysiology for the membrane potential of cardiac cells, this work is typically specific to the generation of action potentials that induce the operation of the heart muscles. As a result, the models are not transferable to attempts to model steady-state operational conditions of cells. The one model that has been created explicitly for the hepatocyte, that by Melkikh and Sutormina [81] has been explained here in detail. There exists, in this model, a number of mathematical issues with its formulation. Secondly, a model proposed by Endresen *et al.* that first describes equations for determining the membrane potential of a generic cell is detailed here, as these non-specific equations are suitable for adaption in the modelling of hepatocytes.

2.6 SUMMARY

This chapter has performed two roles; firstly, the physiology and some pathophysiology of the liver and its cells are detailed with the purpose of bridging clinical knowledge of the organ and the issues presented when applying thermal ablation therapies. Subsequently, this chapter reviews some of the significant models that are relevant to the modelling chapters that follow. This literature review is presented in three parts, each dealing with the core themes relating to modelling thermal ablation: models for the prediction of heat transfer through the liver tissue; models for

predicting the temporal progression of cell death and tissue damage that result from elevated temperatures; and finally, two models that are used for creating a model for the prediction of thermally induced tissue swelling.

The state of the literature varies greatly between the different modelling scenarios. There is a plethora of heat transfer models, each with a specific set of circumstances to which the model is most appropriate. The literature for models of cell death is dominated by models that use the Arrhenius equation for chemical reaction rates, and by models concerned with cell death at naturally occurring hyperthermia (low temperature rises of a few degrees). The models specifically constructed to deal with high temperature cell death theoretically are few. Finally, there has been extremely little work on cellular models for the prediction of cell swelling, or the tracking of ion transfer across hepatocyte cell membranes. Two relevant models have been reviewed in detail as elements from both will be utilised in creation of a model in chapter 6.

CHAPTER 3

CELL DEATH I: MODEL, INITIAL DATA, AND RESULTS

The work presented in this chapter has been amended from that which appeared as **O'Neill, D. P.**, Peng, T., Stiegler, P., Mayrhauser, U., Koestenbauer, S., Tscheliessnigg, K., and Payne, S. J. (2011). "A Three-State Mathematical Model of Hyperthermic Cell Death" *Annals of Biomedical Engineering*, **39**: 570-579, 2011

3.1 INTRODUCTION

The underlying principle of thermotherapy is that cells have a thermal tolerance, such that if sufficient heat is supplied, or if a critical temperature is exceeded for a critical duration, cells die. At the tissue level, this process manifests itself as the appearance of an ablated zone of dead cells surrounded by tissue, at some distance, that is unaffected by the ablating procedure.

Treatment protocols for power levels, durations, and probe particulars for thermal treatments are dictated by equipment manufacturers [128]. The decision to deviate from these to repeat ablations is at the discretion of the radiotherapist. The

learning curve for radiotherapists has been shown to be steep and to influence patient survival rates strongly [53].

In order to aid radiotherapists in their treatment planning much work has been done to model heat transfer in biological tissue with external heat sources and many of the most significant models have been discussed in chapter 2. The first conclusion arrived at from a review of the literature was that a model should be dynamic in both time and temperature to be of clinical use. Secondly, model parameters should be robust to small changes in experimental data, yet should still vary to reflect different expected outcomes. Finally, a model should be computationally simple so as to not detrimentally lengthen simulation times.

In this chapter, a novel mathematical model is proposed that meets the three key criteria outlined above. This chapter first details the experimental procedure implemented by European project collaborators at the Medical University, Graz (MUG); the minimal post-processing required to manipulate the data into a usable form is also detailed. The novel mathematical model for cell death is then presented and fitted to the data, and results from the fitting are given. A brief discussion is included in this chapter to highlight the areas where further work was recommended; this provides a segue into the following chapter which explains how the data set was expanded and the model was used to further understanding of damage mechanisms leading to cell death during thermal treatment.

3.2 EXPERIMENTAL DATA

Experiments were designed and carried out to a specification so as to produce data specifically for the purpose of creating and fitting the mathematical model described in the next section. The initial investigation consisted of constant tem-

perature heating experiments that were carried out on cultures from two cell lines: human liver hepatocellular carcinoma HepG2 and human lung fibroblast MRC-5.

Cells were cultured overnight at 37 °C in a culture medium of Minimum Essential Medium with 10 % fetal calf serum and 1 % penicillin/streptomycin. The volume concentration of cells was 3×10^4 cells/100 μL, and the cells were seeded in 96-well plates and cultivated overnight in a humified atmosphere (5 % CO_2). Experiments were performed on two pure cultures and three co-cultures (25/75, 50/50, and 75/25) of HepG2 and MRC-5. For each condition, a plate had four separate wells of each culture, the culture medium was replaced with a preheated medium and the plates incubated in a preheated heating cabinet. The preheated temperatures were 55, 65, 75, 85, and 100 °C and the heating times were 300, 600, or 900 s. Before use, the temperature of the heated medium was measured with a HI 935005 K-Type waterproof thermometer (resolution 0.1 °C, accuracy ±0.2 %); the medium was also spot checked during heating. After heating, the heating medium was replaced with a medium at 37 °C and spiked with 20 μL MTS reagent (Promega). After 2 hours of post-heating incubation at 37 °C the absorbance was measured at a wavelength of 490 nm, the recommended wavelength at which there is an absorbance peak. Absorbance was also measured at a wavelength of 650 nm, at which there should be no additional absorbance, thus providing a reference that accounts background contributions from cell debris, fingerprints and other nonspecific absorbance. Both measurements were measured in SpectraMax Plus 384 (accuracy:< 0.006 OD ±1.0 %, precision: < 0.003 OD ±1.0 %). Absorbance measurements were also taken 26 and 50 hours after heating; the recorded absorbance signifies the metabolic activity of living cells. For each time point, the absorbance data were normalised to a control value at 37 °C.

For statistical analysis, each experiment had five or six repeats; each datum was taken to be the mean of the readings from the four wells across all experiments. The data described in this section thus provides cell viability information as a function of heating time, heating temperature, incubation time as well as variations in co-culture cell line make-up.

The raw experimental data exhibited two features that were contrary to what might be logically expected when put in context with the rest of the data. Firstly, some data were recorded with values greater than 100 %; secondly, there occur instances where a datum was recorded to have a higher value than the corresponding datum with a shorter heating time, lower heating temperature, or shorter incubation time. Thus, the data were first filtered to remove instances of these counterintuitive trends.

Any datum with an experimental value greater than 100 % was hard limited to 100 %. Additionally, where a pair of reported cell viabilities increased with increasing temperature (rather than decreased as would be expected), the lower of the two viabilities was replaced with the value of the higher viability so as to give the most conservative result. For the initial data fitting described below, the five data points from the different cultures for each heating temperature (5+1 control), heating time (3), and incubation time (3) were averaged. The resulting 54 data points from combinations of three heating times, six heating temperatures, and three post-heating incubation times are shown in Table 3.1.

3.3 MATHEMATICAL MODEL

Examining the experimental data given in Table 3.1, three monotonic trends can be seen: that cell viabilities decrease with increased heating temperature, that via-

Heating time (s)	Heating temperature (°C)	Post-heating incubation time (hr)		
		2	26	50
300	37	100.0	100.0	100.0
	55	100.0	98.02	98.02
	65	100.0	98.02	98.02
	75	89.66	89.00	86.82
	85	52.89	25.48	9.56
	100	4.23	1.00	0.00
600	37	100.0	100.0	100.0
	55	94.71	83.75	83.75
	65	56.94	22.33	13.38
	75	7.89	1.47	1.47
	85	2.45	0.00	0.00
	100	1.19	0.00	0.00
900	37	100.0	100.0	100.0
	55	66.99	53.80	10.61
	65	10.75	1.33	1.65
	75	2.65	0.00	0.00
	85	2.51	0.00	0.00
	100	0.00	0.00	0.00

Table 3.1: Experimental data after simple post processing

bilities decrease with increased heating duration, and that viabilities decrease with increased duration of post-heating incubation. Since the heating duration and incubation time both have reductions in cell viabilities despite being drastically different time scales it was thought that there must be two or more different processes causing cell death. The mathematical model for cell death is presented in two parts: a fast cell death mechanism for reductions in viability that occur on durations of the order of minutes, and a slow cell death mechanism that occurs on durations of the order of days.

3.3.1 Fast Cell Death

The model includes a third 'vulnerable' compartment, which is located between the fully alive (A) and dead (D) compartments in the same way as proposed by

Breen *et al.* [12] and Szasz and Vincze [123]. In biological terms, it is intended to represent a state where the cell's normal functions may be impaired but where the cell is not yet fully dead. As shown in Figure 3.1, the three-compartment model has three possible compartment transitions: alive to vulnerable, vulnerable to alive, and vulnerable to dead.

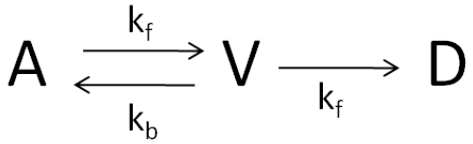

Figure 3.1: Schematic of model showing fast cell death transitions.

The transition from alive to vulnerable represents initial damage caused to an injured state, possibly a state where the cell is no longer functioning normally. Once past a critical point the cell progresses to a dead state from which the cell cannot return. The transition from vulnerable to alive represents the self healing process whereby an injured cell can recover to its fully functional alive state similar to Jung's lesion model [57].

As proposed, all complex stages of the path to cell death are modelled by a single damage mechanism, thus as the processes from alive to vulnerable and from vulnerable to dead are taken to be two stages of the same result of state change, a single forward rate constant, k_f, is assumed for simplicity. The biological process for healing (vulnerable to alive) is separate from the mechanism for thermal damage and is thus assigned a different, backward, rate constant, k_b, assumed to be invariant with temperature. Using standard reaction kinetics, the system can be described mathematically by three simultaneous differential equations, however as all cells are accounted for in one of the three compartments, i.e. $A + V + D = 1$, the system can be reduced to two simultaneous differential equations, the solution to

which describes the system with two degrees of freedom:

$$\frac{dA}{dt} = -k_f A + k_b (1 - A - D), \tag{3.1}$$

and

$$\frac{dD}{dt} = k_f (1 - A - D), \tag{3.2}$$

where A and D are respectively the fractional population of cells in the alive and dead states. To represent the fact that at normal body temperature there is no significant thermal damage, at 37 °C the forward rate constant must be small, thereafter increasing with temperature. A simple exponential curve fits these criteria of temperature dependence, mimicking the fact that tissue that is already highly damaged is most susceptible to further damage. To acknowledge the fact that the damaged state of surrounding cells may have a greater than linear influence on the reaction dynamics the volume fraction of cells in the vulnerable and dead compartments $(1 - A)$ is incorporated into the forward rate constant:

$$k_f = \overline{k_f} (1 - A) e^{(T/T_k)}, \tag{3.3}$$

where $\overline{k_f}$ is a scaling constant and T_k is a parameter that sets the rate of the exponential increase with temperature; both T_k and T have units of °C. Thus for each experiment with a fixed heating time and temperature, there are three independent variables dictating the dynamics of the system: $\overline{k_f}$, k_b, and T_k.

One result of the inclusion of $(1 - A)$ in the forward rate constant is that an initial condition of all cells being in the alive compartment would result in a static solution. The initial conditions were thus set such that a small portion of cells start in the vulnerable compartment. This was set to be 1 %, which is sufficiently small to have negligible effect on the intended dynamics of the system. The portion of cells initially in the dead compartment was set at 0 %.

3.3.2 Slow Cell Death

The part of the model that incorporates the modelling of cell death evident during post-treatment incubation is now presented. Although rapid and large changes in cell viability occur during thermal treatments, the experimental data show that cell viability continues to decrease in the 24, and 48 hours after heat treatment. The mathematical model presented in the previous section is temperature dependent and therefore cannot fully account for this additional cell death whilst the cells are in normothermia and so an extension is now proposed. Closer examination of the data reveals that cultures with significant reductions in cell viability (approximately < 80 % cell viability) caused by thermal heating subsequently progress over time to a fully dead state with 0 % cell viability. However, for lesser levels of thermal damage, the final value of cell viability is somewhat greater than zero.

The proposed extension to the model to account for cell death via a secondary, slow mechanism requires two further transitions in the model. These are both single direction transitions to a dead state – one from the alive compartment and one from the vulnerable compartment – as shown in Figure 3.2. Cells that are not dead can gradually progress from their current state to the dead state; there is no facility for dead cells to be healed. The conditions post heating (incubation at 37 °C) are such that the rate constant for fast cell death, k_f, is zero. Thus, when considering slow cell death, cells need only be considered in two compartments: 'dead' and 'not dead' as shown in rate equation form in Equation 3.4.

$$(A+V) \xrightarrow{k_s} D, \tag{3.4}$$

The resultant reaction dynamic of this rate equation is thus:

$$\frac{dD}{dt} = k_s (1-D), \tag{3.5}$$

where k_s is the rate constant for the transition from 'not dead' to 'dead'.

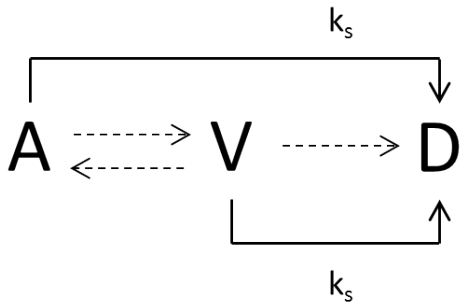

Figure 3.2: Schematic of model highlighting slow cell death transitions.

To fit the model to the data, the rate constant k_s was assumed to be solely a function of the fraction of cells in the dead compartment. The following restrictions were imposed on the rate constant, based on the experimental data:

1. $k_s > 0$ for all D so that no dead cells return to an alive state;
2. $k_s = 0$ at $D = 0$ such that no cells die when the tissue is 100 % alive;
3. $k_s = 0$ at some threshold value, D_τ, such that there is a value of maximum cell death for cultures which have suffered only minimal thermal damage.

Various forms of curve that satisfied these conditions were tried and qualities of fit examined; the form of curve found to give the best fit to the data was a quartic expression in D where conditions 1 and 3 combine to give a repeated root:

$$k_s = \overline{k_s} D\,(1-D)\,(D-D_\tau)^2\,, \tag{3.6}$$

where $\overline{k_s}$ is a baseline scaling value for the rate constant and D_τ is the threshold value described in the third criterion above. The final form for k_s is thus characterised by just two parameters, $\overline{k_s}$ and D_τ.

3.4 DATA FITTING RESULTS

As with the previous section, where the mathematical model for cell death was set out in two parts — one accounting for a fast cell death and one modelling a slower process — this section is similarly divided into results from fitting each part of the model to the data.

3.4.1 Fast Cell Death

The inclusion of $(1 - A)$ in Equation 3.3 makes the paired differential equations 3.1 and 3.2 nonlinear and without a simple analytical solution. To fit the 3-parameter model to the experimental data, the paired differential equations were first solved numerically over time for a fixed heating temperature using a fourth-order Runge-Kutta solver in MATLAB. A typical time course for fixed temperature heating is shown in Figure 3.3; a state of dynamic equilibrium is sought between the alive and vulnerable compartments whilst there is a continual leakage of cells from the vulnerable to the dead compartment. This increase lags behind the increase in the fraction of cells in the vulnerable state, and results in the 'shoulder region' found in experimental data. It is worth noting that the output from the model used to fit the observed experimental data is the total of the cells in the alive and vulnerable compartments, or $(1 - D)$.

To determine values for the three parameters the MATLAB function 'fminsearch' – which finds a minimum of an unconstrained multivariable function using a derivative-free method – was used to find the set of parameters that minimised an error function consisting of the root-mean-square error between each experimental data point and the value of 'alive+vulnerable' output from the numerical solution in MATLAB at the relevant time point. Experimental results were initially averaged across the five co-cultures for each heating temperature and heating duration.

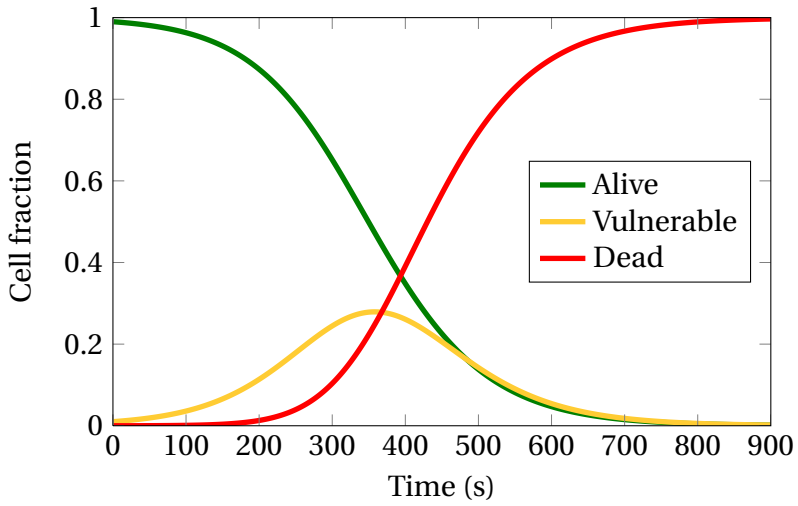

Figure 3.3: Typical time course for fixed temperature heating displaying fractions of cells in alive, vulnerable, and dead states

Table 3.2 gives the optimised parameter values, whilst in Figure 3.4 the resulting predictions are shown in terms of cell viability plotted against heating time, one line for each heating temperature. The experimental data and corresponding error bars – the standard error for each datum – are also included to demonstrate the closeness of the fit. The RMS error between the model with the optimal parameter set and the data is 1.40 %; this value is well within the tolerance of the experimental data at two hours incubation time which has an mean standard error of 3.39 %.

Parameter	Units	Value
$\overline{k_f}$	$\times 10^{-3}\,\mathrm{s}^{-1}$	3.33
k_b	$\times 10^{-3}\,\mathrm{s}^{-1}$	7.77
T_k	°C	40.5

Table 3.2: Optimised parameter values for minimum error

3.4.2 Slow Cell Death

To determine the two parameters $\overline{k_s}$ and D_τ, an error minimisation was again performed in MATLAB as in the previous section. The data were extracted as 18 sets

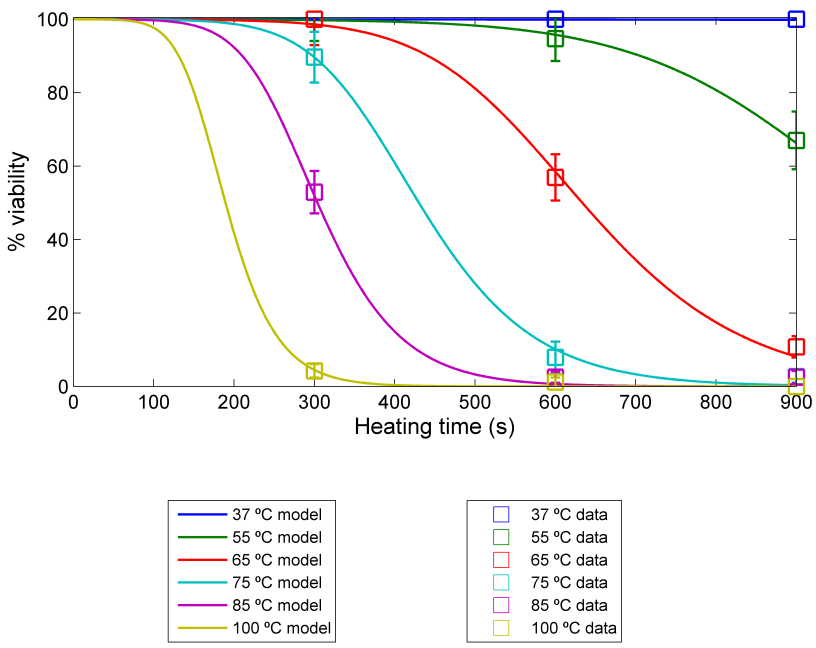

Figure 3.4: Predicted cell viabilities using parameters given by Table 3.2 for the Fast Cell Death Model.

of cell viabilities with three incubation time values; one set for each combination of heating temperature and heating time - as shown in Table 3.1. Since the rate for slow death is far smaller than the rate for fast cell death, it was assumed that negligible slow death would occur during the heating time and so the models were applied successively. The data point for 2 hours incubation was used each time as the initial condition required to solve Equation 3.2 numerically. The MATLAB function 'fminsearch' was applied to a root-mean-square error function for the errors for all 54 data points. The resulting parameter values are given in Table 3.3.

Figure 3.5 shows the 18 resulting theoretical plots from the model using the error minimising parameter values as given in Table 3.3 as well as the corresponding experimental data points and associated error bars. The RMS error between the fitted model and the experimental data for the entire data set of slow death plots is 2.80 %;

this is very similar to the mean standard error for the entire experimental data set (2.71 %).

Parameter	Units	Value
$\overline{k_s}$	$\times 10^{-3}\,\mathrm{s}^{-1}$	0.316
D_τ	-	0.208

Table 3.3: Optimised parameter values for minimum error

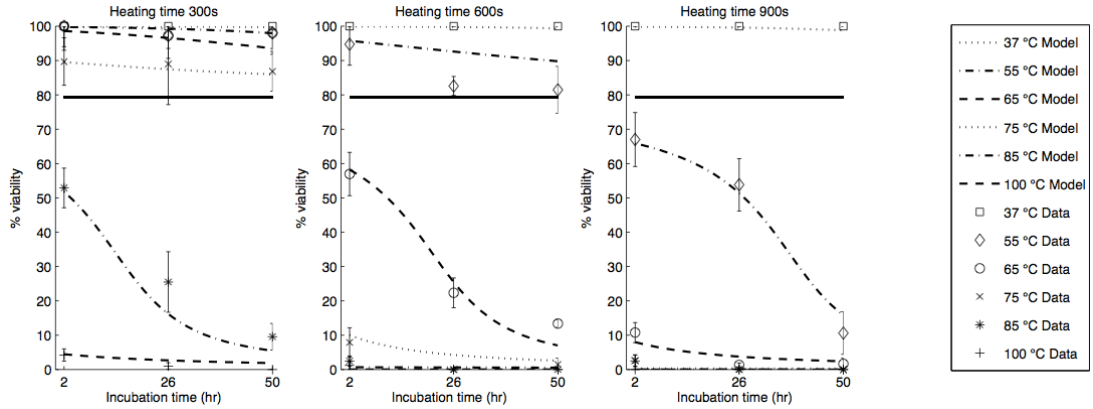

Figure 3.5: Predicted cell viabilities using optimised parameters for the Slow Cell Death Model.

Figure 3.5 shows the different cell viabilities during incubation at 37 °C. Cultures with cell viabilities greater than 80 % at 2 hours of incubation remain above 80 % cell viability, whereas cultures starting below 80 % cell viability all progress towards a final state with 0 % viability. This 80 % threshold is shown in the figure by the solid line and can be interpreted as a critical cell viability, one that can be utilised to determine the final cell viability from the cell viability at two hours of incubation and no other information.

3.5 DISCUSSION

The mathematical model proposed in the previous section contains a number of assumptions. The most significant limitation is that there are only two possible processes leading to cell death - heat induced fast cell death and subsequent cell viability dependent slow cell death; however, due to the good nature of the fit, this limitation does not seem overly restrictive. Other models consider the dynamic progression towards cell death over the time span of thermal treatments (10^3 s), but they cannot account for the continued progression to death exhibited by the experimental data post heating. To model cell death over this extended timescale (10^5 s) during which there is no additional thermal input, either the rate constants controlling instant thermal cell death must be reduced to zero magnitude, or a separate, slow death model must be introduced. A discontinuous pair of successive models is not ideal and thus the proposed model directly halts compartment transitions due to fast cell death by including a temperature dependence in the rate constant for fast cell death.

Common to the transitions for both fast and slow cell death in the proposed model, as well as in the majority of the literature, is the assumption that the transition to death is irreversible. This has been accounted for here through use of a vulnerable compartment from which they can heal and return to the alive compartment. This corresponds to the 'Marginally Damaged' state proposed by Breen *et al.* [12], or the 'excited' form proposed by Szasz and Vincze [123]. In all three models, only partially damaged cells can progress to death. In the slow cell death part of the model however it is assumed that past the criterion that determines that an individual cell will die there is no ability to reverse or halt the process.

The value of using a three state model can be assessed by comparing the results of the previous section with results from fitting the commonly used Arrhenius model as shown in Figure 3.6. Using the standard form for the rate constant of a two state, irreversible process:

$$k = Ae^{(-E_a/RT)}, \tag{3.7}$$

the two parameters A and E_a were determined by fitting to the same data with the same fitting process as described previously. The optimal values for minimum error were found to be $769\,\mathrm{s}^{-1}$ and $37886\,\mathrm{Jkg}^{-1}$; the RMS error was 20.59 % indicating a poor fit.

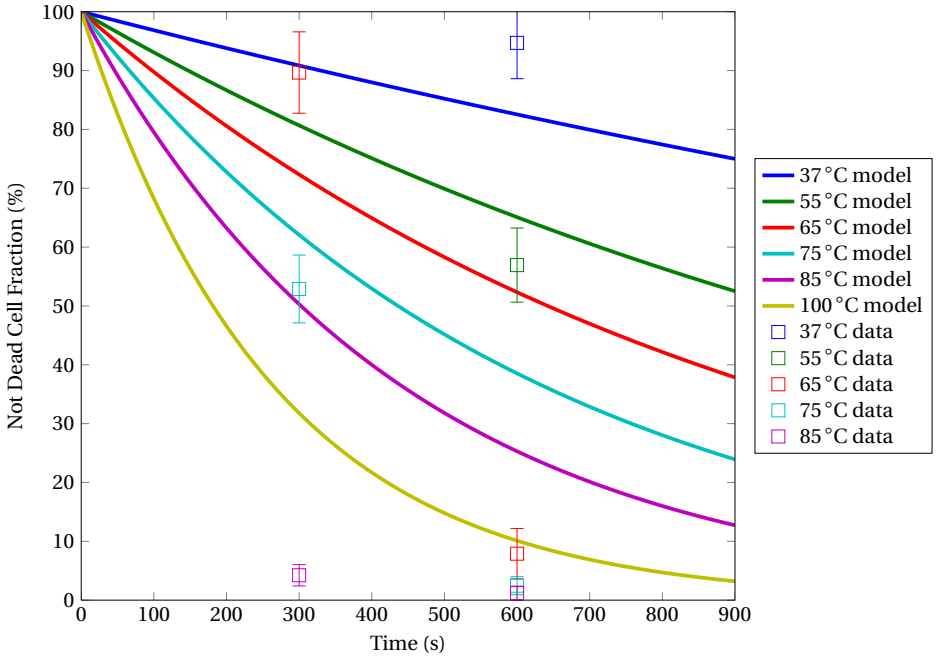

Figure 3.6: Arrhenius model predicted cell viability (continuous lines) and experimental data (symbols) with error bars.

It is thus shown that the simple two-state Arrhenius model is incapable of modelling the no-treatment condition of a continuous incubation temperature of 37 °C as the nature of the model predicts significant cell death even in normothermia. As a second comparison, the model of Jung [57] was fitted to the same data, however this is a considerably more substantial exercise which leads to some mechanistic

insight into modelling of the processes that lead to cell death and thus is presented in chapter 5.

Despite the low RMS error calculated here, indicating a high quality of model fit with only a few parameters, there are some limitations. The fast cell death part of the proposed model requires an initial fraction of cells to be in the vulnerable compartment. The choice of $A_0 = 0.99$, $V_0 = 0.01$, $D_0 = 0$, is a reasonable choice since 1 % of cells in the vulnerable compartment is a sufficiently small fraction to induce negligible 'acceleration' of the system. A smaller value would, however, generate greater dynamic 'inertia' and result in significantly higher values of the fitted parameter . Re-optimising the parameter values with $V_0 = 0.1$ %, the RMS error for the fast cell death data fitting becomes 2.71 %, whilst with $V_0 = 5$ %, the RMS error becomes 3.02 %, significantly worse fits than that proposed (RMS error of 1.4 %). Two issues arise from this inclusion of a non-zero V_0. Firstly, there is a problem in the physical interpretation: in well controlled small culture experiments of discrete cells it is theoretically possible to ensure that $V_0 = 0$; in this scenario, the proposed model would remain at its initial conditions of $A_0 = 0$, $V_0 = 0$, $D_0 = 0$, and no cell death would be possible. The second possible issue is that initial damage might be higher than $V_0 = 1$ %. In these cases the dynamic behaviour of the system would be significantly different to that simulated above. Such a scenario might arise in clinical thermal treatments where certain fractions of cells have already entered a vulnerable or dead compartment due to non-thermal causes such as physical trauma (needle induced damage) or chemical injury (chemotherapy drug induced damage). However this would be very difficult to quantify.

The fast cell death model has three possible transitions. To minimise the number of free parameters in the model, it was assumed that the forward rate constants governing the transitions $A \rightarrow V$ and $V \rightarrow D$ are the same. The physical interpre-

tation of this is that there is a single damage process which incorporates all physiological damage mechanisms. This mathematical simplification is justified as the vulnerable state is an arbitrarily set position along the fast path to cell death representing the 'point of no return' rather than a change in the mechanism of thermal damage, or a defined, physically different state of the cell.

The final assumption made in the mathematical model for slow cell death is that there is some threshold value of cell viabilities of the surrounding cells, below which cells progress to death, and above which cells settle at a non-zero level of viability. The concept for this threshold came from inspection of clinical radiofrequency ablation zones. Regions of ablated tissue were found to increase in size during a period of days following thermal therapies, however, the zones did not increase in size indefinitely. Inspection of the distribution of alive and dead cells around the ablated zones' border regions revealed that isolated alive cells with an ablated zone were not observed in tissue left for several days. Further, isolated dead cells in mostly alive tissue outside an ablated zone were still present many days later. A link has been shown between the presence of heat-shock proteins (created due to thermal stress) and apoptotic dead cells [115]. From this it was assumed that the variable governing slow cell death was the local cell viability, which may be modelled by a threshold value.

This cell viability threshold is of immense practical importance computationally. Cell death models are typically derived to complement heat transfer models in predictive computational simulations for planned ablative treatments. By defining a critical cell viability, a threshold is set such that following the simulation of the thermal therapy, the simulation can be halted and the final ablative zone can be calculated. This is possible using the proposed model since slow cell death is solely a function of the conditions at the end of the thermal treatment.

The data used for fitting the model described in section two were obtained from cell cultures assumed to be experiencing step change temperature heating. Additionally, the finite mass of the cell cultures and the finite rate of heat transfer means that a step change imposed temperature is an approximation. Steps were taken to minimise deviations from an ideal heating scenario such as working with pre-heated chemicals, close to the heating cabinet, and multiple practise-runs were undertaken so as to reduce wasted time. However these inherent uncertainties should be considered as potential sources of error. This raises another important consideration: tissue is neither isotropic nor homogenous; so far, the proposed model has only been fitted to data from cultured media, there is no information available on the possible effects of specific geometries and distributions of differing cell lines.

The isotropic and homogenous assumptions cause problems when the presence of two different types of cell is considered. Absorbance measurements cannot differentiate whether or not a mixed cell culture has the same ratio of cell types after heating relative the initial cell culture, or a different ratio. Different cell types will have different levels of metabolic activity, for example, anchorage-dependent cells that undergo contact inhibition might produce a non-linear relationship between cell number and absorbance. The recommended procedure for tumour cells and for fibroblast cells lines is the same, and although exact metabolic rates of the cells are not reported, the American Type Culture Collection recommended culture protocol is identical for both cell types [129][130], including quantities, from this it was assumed that the two cell lines have similar metabolic rates, and therefore similar contributions to the absorbance measurements.

3.6 CONCLUSION

In this chapter the work leading to the creation of a novel mathematical model for cell death was detailed, including an explanation of the bespoke experimental data, the fitting process and the mathematics of the model itself.

The model is capable of predicting fast cell death as a function of temperature during thermal treatments and is capable of accounting for further, slow death of cells in the days following treatments. Simulation results from the fast cell death model fit experimental data well as a function of both treatment temperature and treatment duration, and exhibit the 'shoulder region' of low dosage thermal tolerance reported in the literature. Slow cell death model simulation results also fit the experimental data well and confirm the hypothesis that there is a critical cell viability that determines whether cell cultures at non-zero, non-unity cell viabilities progress to a completely dead state or not.

Results of data fitting show this critical cell viability to be ≈ 80 % alive; this result is of practical importance with potential for more accurate prediction of cell death. That which is presented in this chapter is model creation, based upon an initial set of experimental data. More data was subsequently provided by collaborators at MUG and the next chapter deals with subsequent model development arising from an expanded data set.

CHAPTER 4

CELL-LINE EFFECTS

The results of section 4.3 and the corresponding discussion in section 4.5 that deal with HepG2 and MRC-5 cell line variations have appeared in part in **O'Neill, D. P.**, Peng, T., Stiegler, P., Mayrhauser, U., Koestenbauer, S., Tscheliessnigg, K., and Payne, S. J. (2011). "A Three-State Mathematical Model of Hyperthermic Cell Death" Annals of Biomedical Engineering, 39: 570-579, 2011

4.1 INTRODUCTION

Whilst the previous chapter presented a novel mathematical model for cell death resulting from thermal treatments, it also highlighted a number of areas for further investigation. This chapter contains three main parts; first, additional experimental data became available following the work presented in the previous chapter; this was used to fit the model as a form of model self-validation but also highlighted an area for further investigation. Next, the data that had previously been averaged before being used for model fitting in the previously presented results were used to fit the model to investigate parameter dependencies upon cell line type. Finally, a modified experimental technique produced one additional data set; these data

are also used to fit the model. A combined discussion of the three sections of this chapter follows before a short conclusion that relates this chapter's discoveries to the work of the previous chapter with implications for clinical implementation.

4.2 LIVER STELLATE CELL LINE DATA

4.2.1 Experimental Data

At a date subsequent to the initial investigation, alternative experimental data was gathered by collaborators from MUG. An identical experimental procedure to that described in the previous chapter was implemented, however whilst the inclusion of the HepG2 cell line was maintained, the human lung fibroblast cell line MRC-5 was replaced with a human liver stellate cell line LX-1. The resultant experimental data (not explicitly given) shows results that are qualitatively similar to the original experimental data, but are numerically different by more than the standard error of the experiments. In the same manner as previously, the new data were averaged across separate co-culture mixtures.

As explained in section 2.2, in addition to differing physiological roles, liver stellate cells such as those of the cell-line LX-1 have different physical properties to fibroblast cells such as the lung fibroblasts of the MRC-5 cell-line. It is therefore likely that the presence of fat deposits and the differing structural shape of various cells may result in similar, but distinct, parameter values for the model to best fit the experimental data.

4.2.2 Results of Fitting

First attempts to find optimum parameter values that produced cell death predictions with minimum error when compared to the experimental data showed that

the three parameters (forward rate constant scalar, $\overline{k_f}$, backward rate constant, k_b, and temperature constant, T_k) showed no consistent trend across the data. Thus the system was reduced to two parameters by setting the backward rate constant, k_b, at the value found in the previous chapter: $7.77 \times 10^{-3}\,\mathrm{s}^{-1}$. The results obtained by fitting the remaining two parameters to the data are given in Table 4.1. Plots of simulations run with these optimised parameters and the corresponding experimental data are shown in Figure 4.1.

Parameter	Unit	HepG2/MRC-5 (original data)	HepG2/LX-1
$\overline{k_f}$	$\times 10^{-3}\,\mathrm{s}^{-1}$	3.33	2.52
k_b	$\times 10^{-3}\,\mathrm{s}^{-1}$	7.77	7.77
T_k	°C	40.5	34.6

Table 4.1: Optimised parameter values for minimum error across both data sets

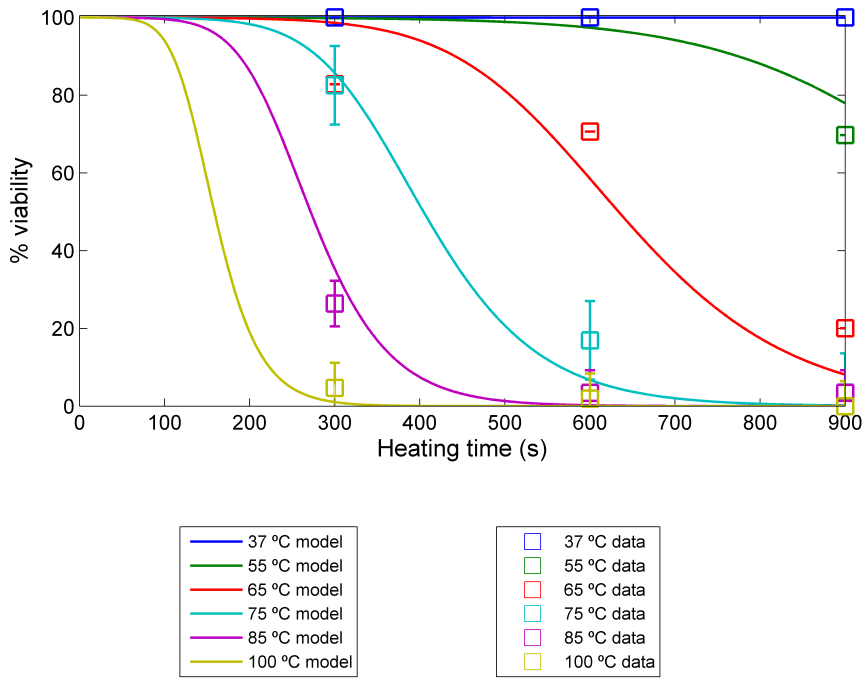

Figure 4.1: Predicted cell viability (continuous lines) and experimental data (symbols) with error bars for experiments with cells from the HepG2 and LX-1 cell lines.

It is clear that the data obtained from co-cultures involving the LX-1 cell line give consistent, but different parameter values to data obtained from co-cultures involving the MRC-5 cell line. Figure 4.1 qualitatively shows a good fit of the model to the new experimental data. For almost all data points, the lines of best fit are within the errors bars that represent the standard error of the experimental data. Where this is not the case — 900 s of heating at 75 °C and 85 °C for example — the deviation is no more than a few percentage points. As with the data and fitted model presented in the previous chapter, the data seem to represent well the range of possible time/temperature combinations; whilst many of the data record experimental results either before substantial cell death has occurred, or after major cell death, there are nonetheless 8 data points that lie in the range $5\% < x < 95\%$.

4.3 CELL LINE DEPENDENCE

4.3.1 Experimental Data

Upon a closer examination of the experimental data described in subsection 4.2.1, some variation is apparent in the raw data before averaging across different co-cultures: co-cultures with higher contents of the lung fibroblast MRC-5 are recorded to have higher cell viabilities than co-cultures with higher contents of hepatocellular carcinoma HepG2 cells for the same temperature and time. This feature suggests that fibrous tissue may be more resilient to heat treatments. Here, the fast cell death part of the model was fitted to the data at 2 hours of post heating incubation for individual co-cultures to examine the dependence of each parameter upon the HepG2 content of the co-culture.

4.3.2 Results of Fitting

Attempts to determine cell line dependence for all three parameters that control the O'Neill Model proved unsuccessful. Using the same error minimisation procedure used previously, the parameter value sets that resulted in minimal error showed little consistency of value across different data sets of single co-cultures; this was despite similar final RMS error values. Instead, each parameter was investigated in turn whilst the other two were fixed to a single value; for combinations of MRC-5 and HepG2 cell lines, the values used were those given in the previous chapter, and for combinations of LX-1 and HepG2 cell lines, the values from the previous section were used. Table 4.2 gives results from varying each parameter separately for the MRC-5/HepG2 experiments, whilst Table 4.3 gives corresponding results for the LX-1/HepG2 experiments. These parameter values are also plotted graphically in Figures 4.2 and 4.3 where the parameter values have been normalised to the optimised values from the averaged data given earlier. These results are discussed later in subsection 4.5.2 and general conclusions are drawn in the final section of this chapter.

		Co-culture cell line make-up (% content of HepG2)				
Parameter	Unit	0 %	25 %	50 %	75 %	100 %
$\overline{k_f}$	$\times 10^{-3}$ s^{-1}	3.09	3.18	3.26	3.47	3.69
RMS error	%	5.09	2.54	1.81	1.67	5.05
k_b	$\times 10^{-3}$ s^{-1}	9.21	8.65	8.16	7.05	5.90
RMS error	%	5.70	2.81	1.84	2.04	6.48
T_k	°C	42.3	41.6	41.0	39.5	38.1
RMS error	%	4.98	2.65	1.89	1.75	4.33

Table 4.2: Optimised parameter values and corresponding RMS errors for different co-cultures using the experimental data from HepG2 and MRC-5 cell lines

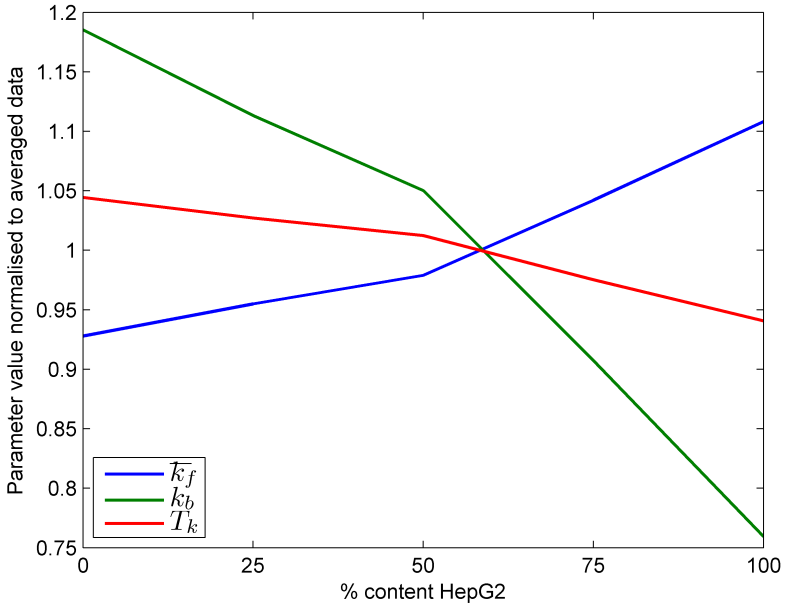

Figure 4.2: Optimised parameter values normalised to values from averaged data and corresponding RMS errors for different co-cultures using the experimental data from HepG2 and MRC-5 cell lines

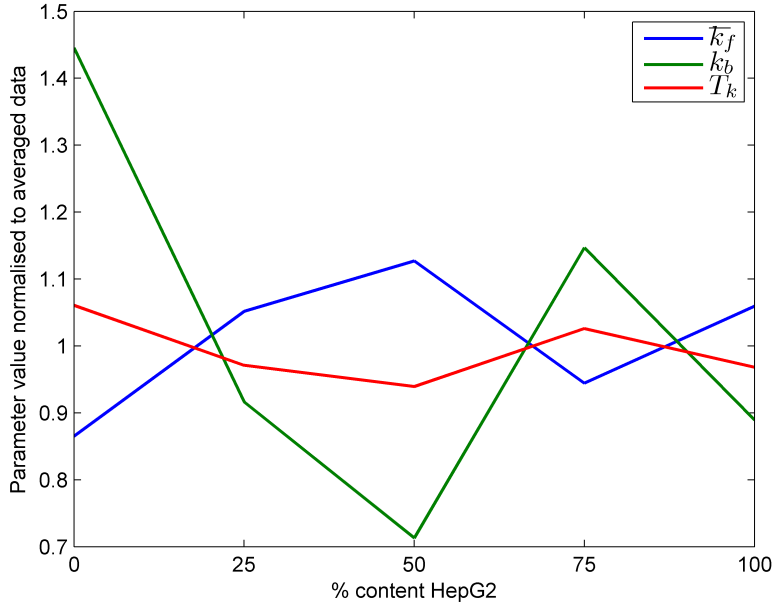

Figure 4.3: Optimised parameter values normalised to values from averaged data and corresponding RMS errors for different co-cultures using the experimental data from HepG2 and LX-1 cell lines

		Co-culture cell line make-up (% content of HepG2)				
Parameter	Unit	0 %	25 %	50 %	75 %	100 %
$\overline{k_f}$	$\times 10^{-3}$ s^{-1}	2.18	2.65	2.84	2.38	2.67
RMS error	%	12.02	7.11	8.36	8.50	7.28
k_b	$\times 10^{-3}$ s^{-1}	11.23	7.12	5.54	8.91	6.91
RMS error	%	10.61	8.08	8.74	8.68	8.17
T_k	°C	36.7	33.6	32.5	35.5	33.5
RMS error	%	12.81	6.39	8.81	8.53	6.73

Table 4.3: Optimised parameter values and corresponding RMS errors for different co-cultures using the experimental data from HepG2 and LX-1 cell lines

4.4 TRANSWELL MEMBRANE EXPERIMENTS

4.4.1 The Transwell Membrane

The Transwell membrane is a registered trademark of Corning Incorporated, a specialist glass and ceramics manufacturer [132]. Depending upon the specific Transwell product, the membrane consists of a single sheet of polycarbonate, polyester, or polytetrafluoroethylene of membrane thickness 10 μm or 50 μm. This structure permits the combined treatment of two different cultures that remain apart and unmixed, yet share the same environment of gaseous surrounds and thermal conditions. The membrane has good optical properties and does not interfere with cell visibility such as that required in determining cell viabilities. Transwell membranes were used to prepare and test combinations of two pure cultures that matched the cell-line ratios of the various co-cultures of LX-1 and HepG2 but here were kept separable.

4.4.2 Experimental Data

Experiments using an altered procedure resulted in a new data set from collaborators at MUG where the HepG2 and LX-1 cell lines were used but all plates were cul-

tivated as pure cultures. To obtain equivalent co-culture effects, a Transwell membrane was used to bring separate pure cultures of different masses together into one thermal mass for the heating duration whilst being kept separable for the subsequent analysis. Mass ratios for the paired pure cultures were the same as for the co-cultures in the previous experiments; i.e. 100/0, 75/25, 50/50, 25/75, and 0/100.

4.4.3 Results of Fitting

Due to the part-cultures that were combined for heating being separated for the subsequent analysis, the results are displayed in Table 4.4 and Table 4.5 separately for each individual part-culture. Graphs of the simulation results produced with the optimised parameters are shown in Figures 4.4 and 4.5.

Parameter	Units	% content of HepG2			
		25	50	75	100
$\overline{k_f}$	$\times 10^{-3}$ s^{-1}	0.009	0.007	0.009	0.605
k_b	$\times 10^{-3}$ s^{-1}	7.77	7.77	7.77	7.77
T_k	°C	8.72	8.46	8.67	18.0
RMS	%	8.43	6.44	3.68	7.62

Table 4.4: Optimised parameter values for minimum error across the HepG2 cell line Transwell experimental data

Parameter	Units	% content of LX-1			
		25	50	75	100
$\overline{k_f}$	$\times 10^{-3}$ s^{-1}	0.018	0.018	0.009	0.002
k_b	$\times 10^{-3}$ s^{-1}	7.77	7.77	7.77	7.77
T_k	°C	9.81	9.86	8.90	7.21
RMS	%	9.62	6.77	6.19	10.3

Table 4.5: Optimised parameter values for minimum error across the LX-1 cell line Transwell experimental data

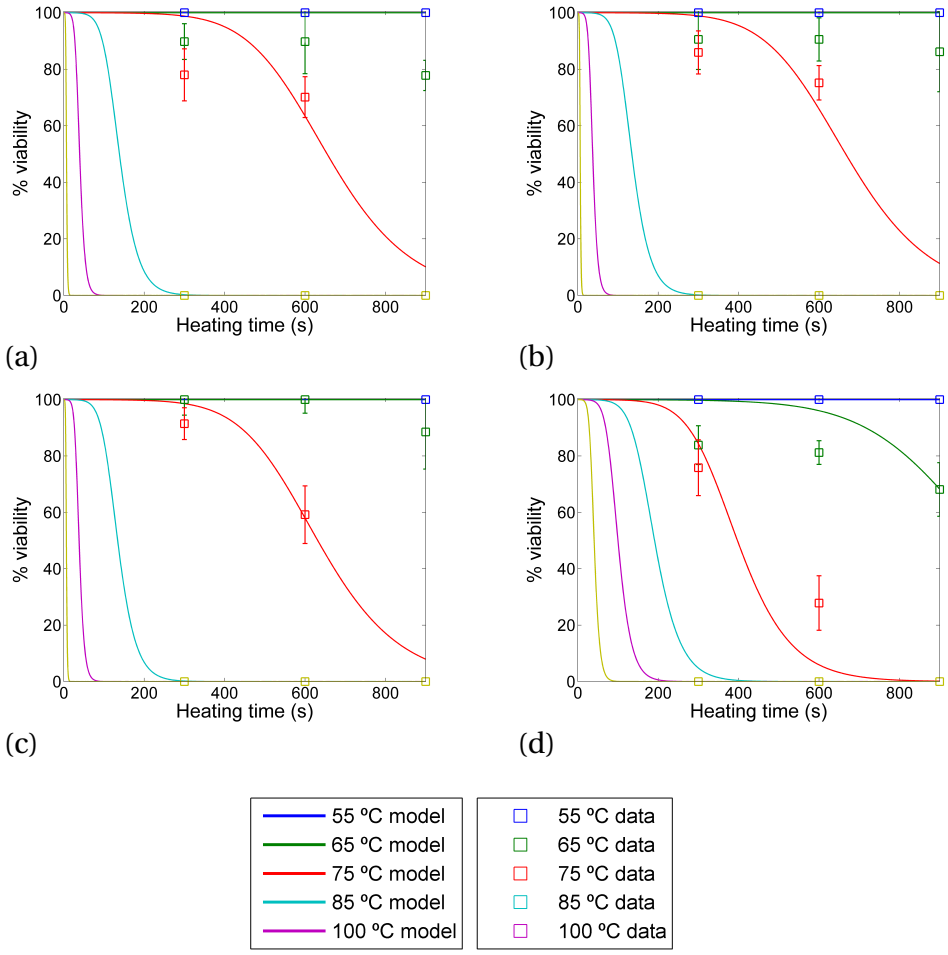

Figure 4.4: Predicted results (continuous lines) obtained from fitting the two-parameter O'Neill Model to the experimental data (boxes) for various contents of HepG2 cell in the co-cultures of the Transwell membrane experiments (a) 25 % HepG2, (b) 50 % HepG2, (c) 75 % HepG2, (d) 100 % HepG2

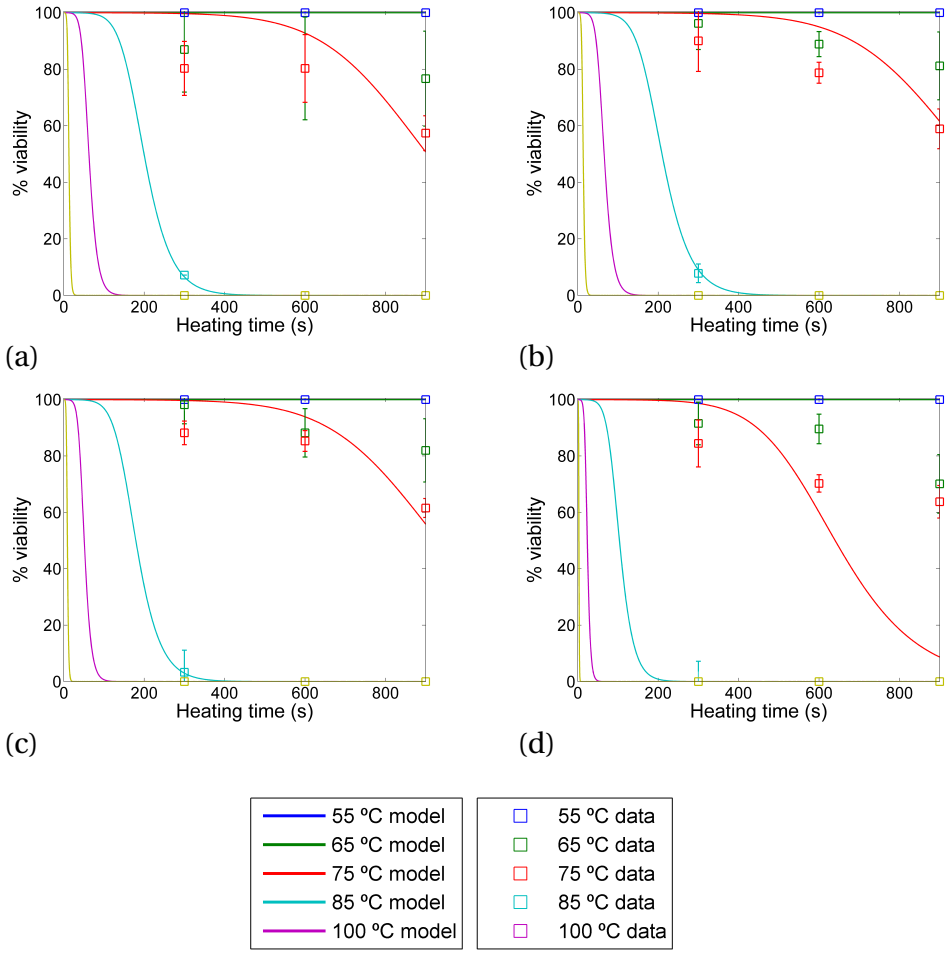

Figure 4.5: Predicted results (continuous lines) obtained from fitting the two-parameter O'Neill Model to the experimental data (boxes) for various contents of LX-1 cell in the co-cultures of the Transwell membrane experiments (a) 25 % LX-1, (b) 50 % LX-1, (c) 75 % LX-1, (d) 100 % LX-1

Numerical results obtained from fitting the two-parameter model to the experimental data obtained from the Transwell experiments are considerably different, and therefore somewhat inconclusive. Figures 4.4 and 4.5 show that much of the data from the experiments that used the Transwell membrane have either negligible reduction in cell viability, or reductions to 0 % or a few per cent. In each plot there were, at most, 2 heating temperatures that produced data with values between 20 % and 90 %. Due to of the requirement to ensure temperatures of 75 °C or higher resulting in near-complete cell death by 300 s, the optimised value for T_k was small relative to that found in the previous chapter and in sections 4.2.1 and 4.3 — values for T_k reported here are ≈ 30 % of values reported previously.

The direct consequence of lower reported values for T_k is lower reported $\overline{k_f}$. This is because of a combination of two features of the experimental data. Firstly, the data from heating at a temperature of 55 °C show similar cell viability reductions from the Transwell membrane experiments as with data from the original two experiments. Secondly, as previously mentioned, the reductions in cell viability at higher temperatures are much greater in the data from the Transwell membrane experiments than previously. In order to accommodate the feature of the Transwell data that has greater damage with increased heating temperature, the values for T_k are lower and therefore the component e^{T/T_k} in the forward rate constant is higher. Thus, to produce similar total rate constants for lower temperatures, the values of $\overline{k_f}$ are correspondingly lower than previously. Actual values for $\overline{k_f}$ are less than 1 % of those reported for experiments not involving the Transwell membrane.

Subfigures (a), (b), and (c) in Figure 4.4, and all four subfigures in Figure 4.5 each have only one predicted plot that neither stays at 100 % viability, nor proceeds rapidly to ≈ 0 % viability. The other subfigure, of Figure 4.4(d), which produces two 'intermediate' plot lines has a pair of parameter values that sit between the other

values given in Table 4.4 or Table 4.5, and those values given in previous sections; $\overline{k_f}$ is an order of magnitude greater than the rest of Table 4.4 and Table 4.5, whilst T_k is approximately twice the values found for the other data sets. In qualitative terms, the graphical result shown in subfigure Figure 4.4(d) is more similar to the graphs plotted previously in the first part of this chapter and in the previous chapter.

The values of RMS errors reported in Tables 4.4 and 4.5, with the exception of the 75 % HepG2 data, are noticeably larger than those from the previous sections and chapter. However, the values are still all below 10 %, which, considering the sparse nature of the data seems reasonable. It should be noted, however, that the good fit of the 37 °C data (always 100 % viability) and the seemingly good fit of the $T \geq 75$ °C data (approximately 0 % by 300 s) heavily influence the reported RMS error. These four heating temperatures that are fit well by the model combined have twice the influence on the implemented error function than the two plots with relatively poor fit (those plots attempting to fit intermediate cell viabilities of 55 °C and 65 °C heating temperatures. Further interpretation and implications of these results are now discussed.

4.5 DISCUSSION

4.5.1 Liver Stellate Cell Co-cultures Experiments

The additional experimental data from the experiments on LX-1/MRC-5 cell co-cultures were used in the first steps for both model validation and model refinement. The optimised parameter values for the model when fitted to the further experimental data were $2.52 \times 10^{-3}\,\mathrm{s}^{-1}$ and 34.6 °C, for $\overline{k_f}$ and T_k respectively. The value for k_b used for fits of the new experimental was fixed at the value found in chapter 3. A robustness analysis was performed on the choice of fixing the value

for k_b as that found in the previous chapter. Various alternative values for k_b were tested and, for each, complementary values of $\overline{k_f}$ and T_k were found that produced similar qualities of fit. The parameter space was determined to have an additional degree of freedom and thus one parameter, k_b, was chosen to be fixed. When compared to the optimised parameter values from the original data set, these new values are found to differ from the values in the previous chapter by 24.3 % and 14.6 %, which are within the same order of magnitude. Consistency of parameter values to this extent is a strongly positive indication for model validation especially when compared to variations in parameter values used for other models, notably Arrhenius-based models where parameter values can range over many tens of orders of magnitude [97].

Model fits to the co-cultures of HepG2 and LX-1 cell lines highlighted that co-cultures of cells from different cell lines do result in different parameter values. It was these noticeably different parameter values that led to the investigation into cell line dependence that followed in section 4.3.

4.5.2 Cell Line Dependence

Results obtained from investigating the dependence of parameter values upon cell line make-up of co-culture for mixes of MRC-5 and HepG2 clearly showed that optimised parameter values varied as the make-up of cell co-culture changed. These variations were displayed clearly in Figure 4.2. It is clear that $\overline{k_f}$ increases with increasing content of HepG2 in the co-culture, whilst k_b decreases. As these two rate constants control processes that operate in opposite directions, these two trends indicate that co-cultures with higher content of HepG2 cells are more rapidly damaged. Additionally T_k is shown to decrease with increasing content of HepG2, sug-

gesting that HepG2 cells are increasingly more sensitive to heat as the heating temperature is raised than MRC-5 cells are.

Whilst the results shown in Figure 4.3 appear to show consistent variations less clearly than those in Figure 4.2, the same general trends are evident: that k_b and T_k decrease with increasing HepG2 content, whilst $\overline{k_f}$ increases, and therefore the same conclusions that were drawn for MRC-5/HepG2 co-cultures can be drawn here. In both cases, HepG2 appears to be the cell line that is more at risk to thermal treatment. As HepG2 is the hepatocyte cell line and MRC-5 and LX-1 are fibrous cell lines, the presence and direction of a trend is potentially the most significant result, regardless of magnitude. In the treatment of HCC the principal targets for destruction are the hepatocytes. In complex cases where liver cirrhosis results in the presence of fibrous tissue (cells akin to MRC-5 or LX-1 cell lines would likely be present) higher treatment temperatures or longer heating durations may be required. In these scenarios, knowledge that the target cells are most at risk adds a conservative degree of reassurance that there is a lower chance that dangerous cancerous cells may be left undamaged.

For most fits, the RMS error obtained with the MRC-5/HepG2 data is lower than that for the LX-1/HepG2 data. This feature that suggests that the O'Neill Model struggles to fit the new data as closely as it does to the original data and may, in part, explain why the trend shown in Figure 4.3 is less clear than that shown in Figure 4.2. Without further experimental data to produce a better assessment of the fit of the O'Neill Model to the data, further speculation into LX-1 cell line dependence is not appropriate. It should be noted that the raw (before preprocessing) experimental data set for the LX-1/HepG2 experiments contained more data that appeared counterintuitive than in the original data set, i.e. more data were adjusted in the preprocessing step prior to fitting the model for the LX-1/HepG2 data than

for the original data. This suggests that the quality of the data may have been lower than that of the data used for fitting the model in the previous chapter.

4.5.3 Transwell Membrane Experiments

In the data generated from the experiments using the Transwell membrane, it is notable that experiments conducted at temperatures exceeding, but not equal to, 65 °C have very low cell viabilities. This feature of the experimental data from the Transwell experiments can be expressed qualitatively as having a sharp cut-off threshold at approximately 70 °C. The implication of this feature is evident in the optimised parameter values which show T_k to be considerably lower than that found for the previous data, and also show $\overline{k_f}$ to be greatly lower than before. The implication of these results is that there is a considerably greater dependence upon temperature, suggesting that cells are increasingly more vulnerable to increasingly higher temperatures. Secondly, it is likely that the low values of $\overline{k_f}$ result directly from the heightened temperature sensitivity and as such are required to fit the low levels of damage in data sets recorded at lower heating temperatures.

As Table 4.4 and Table 4.5 show, the RMS errors between fitted values and experimental data are of the order of the mean standard error of the data (3.39 %) albeit higher for every data set; considering the sparse nature of the data, this is a good quality fit. However, the graphical plots of simulation results with optimised parameter values and experimental data (Figures 4.4 and 4.5) qualitatively show the issue arising from attempting to fit the model to data with such a delayed and sharp drop-off in cell viability. Clearly high temperature plots fit the data well because the overall shape of the plot is not assessed, only the start point and three 'end points' all in the decayed tail of the graph. Where a fit of the whole viability curve has been

attempted (red and green lines of lower heating temperatures), the optimised parameter values clearly provide a relatively poor fit.

It is likely that the lower cell viabilities for experiments using the Transwell membrane at higher heating temperatures when compared to the larger cell cultures of the original experiments are the result of additional influences of the experimental set-up rather than significant change in cellular response to heat. This is highlighted in the results of the 25 % Transwell cultures which show greater deviations from the original data than the 50 % or 75 % cultures. During all times other than during the heating period, the experimental procedure used for the experiments with the Transwell membrane involved significantly smaller masses of the cultures than were used in other experiments; thus it may be that the reduced masses of the cultures are primarily responsible for the difference in the data rather than the difference having been caused directly by the presence of the Transwell membrane and the segregation of the different cell lines. There might exist a minimum threshold (in mass or cell number), below which cells lose the thermal tolerance exhibited in the previous experiments here and elsewhere in the literature. Perhaps in this instance, the cells in the smaller cultures (of 25 % and 50 % by mass) were brought below a minimum threshold which resulted in greater sensitivity to heat than would have been expected from the preceding results.

As the results obtained from fitting the model to the Transwell experiments may have been adversely affected, directly or indirectly, by use of the Transwell membrane and thus be less representative of clinical scenarios than the previous data, no further analysis was carried out using the Transwell experimental data, and no further conclusions are drawn on the results obtained. The Transwell membrane may however, be of use for further experimentation the results here suggest that considerably larger masses for should be involved for each pure culture such that

overly vulnerable small masses do not limit the usefulness of the data. Careful characterisation of the influence of the Transwell membrane must be determined so as to separate these effects, for changes in the cellular response to heat.

4.6 CONCLUSION

This chapter detailed additional work that was performed upon the O'Neill model presented in the previous chapter. Using more experimental data, further validation was carried out. An investigation into the survival rates of cells from different cell lines was performed by partioning the experimental data into its original sets of data. Cultures containing a high proportion of cells from fibrotic cell lines were found to be more resistant to cell death. Due to difficulties discerning between different cell viabilities of cells in co-cultures, the true significance of the trends for parameter values shown in Figures 4.2 and 4.3 must be treated with caution. The overall differences between parameters arising from pure cell cultures is a particularly important and significant result clinically; cirrhotic liver tissue is highly fibrotic and a large proportion of HCC are coexistent with cirrhosis of the liver.

The following chapter is the third of those that deal with the prediction of cell death. To this point the O'Neill Model has been presented for the purpose predicting cell death, however one significant draw back with an empirical model such as this is that it adduces no insight into the processes resulting in cell death. To address this lacking, the next chapter presents a commonality between a mechanistic model that is preexistent from the literature and the O'Neill Model, resulting in developments towards a multiscale model for cell death.

CHAPTER 5

A MECHANISTIC INTERPRETATION

The work presented in this chapter has appeared as **O'Neill, D. P.**, Peng, T., and Payne, S. J. (2010). "Comparison of Two Mathematical Models for Hyperthermic Cell Death" Proceedings of 6^{th} World Congress on Biomechanics, 31(2): 748-751, 2010.

5.1 INTRODUCTION

The previous two chapters presented a novel mathematical model for hyperthermic cell death, and then showed how the parameters of the model vary with respect to the cell line under investigation and the experimental techniques used. Whilst this model successfully provides a good prediction of the cell death occurring in the experimental data, because of it's purely empirical nature, it does not lend any insight into the mechanistic processes that lead to cell death. The 'vulnerable' state used by the model is arbitrary in nature; as such, the model previously presented does not contribute any understanding as to the nature of this transitionary state of cells.

In this chapter, the empirically based O'Neill Model proposed in chapter 3 and implemented in chapters 3 and 4 is compared to a mechanistic model from the literature, that proposed by Jung. The Jung Model is modified to provide a better fit with the experimental data and the two models are compared.

5.2 MECHANISTIC MODELS

Thus far, the modelling of cell death has been an empirical process with the development of a lumped state model that assumes large numbers of cells and a per-cent content of 'alive', 'dead', or 'vulnerable' cells. These three states have been given no greater definition than that explained in section 3.3. Whilst this approach may be sufficient to satisfactorily predict cell death in clinical ablations, it is clearly desirable to link the model to mechanistic events to provide greater scientific understanding of the underlying biological processes that lead to cell death. In this section, one such mechanistic model from the literature is explained; it is then modified to resemble closely the O'Neill Model. Both forms of the model are fitted to the experimental data and optimal parameter values are presented.

5.2.1 Original Jung Model

The model proposed by Jung in 1986 is a theoretically developed mathematical model based upon a two step process. In the first step, an alive cell develops a non-lethal lesion which has no direct affect on cell viability; a cell may have any number of lesions without any inhibition in function. Then, in the second step, any non-lethal lesion can convert to a lethal lesion causing the irreversible death of the cell. The model is based upon the following five assumptions.

Firstly, it is assumed that nonlethal lesions are created at a random rate, constant in time for a given temperature. Thus the number of lesions in a cell exhibits a Poisson distribution; the rate is independent of the number of existing lesions; and the average number of lesions per cell increases linearly in time. Secondly, nonlethal lesions do not reduce in number, neither during heating, nor after. Thirdly, the probability of a nonlethal lesion becoming lethal is independent of the number of other nonlethal lesions within the cell, and is constant in time. Further, only one nonlethal lesion need become lethal to kill the cell. Finally, the two probabilities are solely dependent upon temperature and not upon the state of surrounding cells.

Jung's model is a multi-compartmental model consisting of an infinite number of alive states, S_n, which have n nonlethal lesions ($0 \leq n \leq \infty$); and one additional compartment containing the population of dead cells, D. Initially all cells are alive with no nonlethal lesions present, i.e. $S_0 = 1$. Cells progress incrementally from S_n to S_{n+1} with a probability p; and cells move from S_n to D with a probability of nc – the product of the number of lesions and the probability of any single lesion becoming lethal. A schematic for this model is shown in Figure 5.1.

5.2.2 Modified Jung Model

Prior to attempting to fit this model to the data, the results of which are given later, it was decided to modify the model in two ways. Firstly, the probability for lesion creation was altered from a constant, p, to include a linear dependence upon the fraction of lesion-free cells: $p = \overline{p}\,(1 - S_0)$, where $\overline{p}$ becomes the constant to be optimised. Thus cells surrounded by already damaged cells (where S_0 is low) are more likely to generate an additional legion than cells in sourrounds that are in near-perfect health (where S_0 is high).

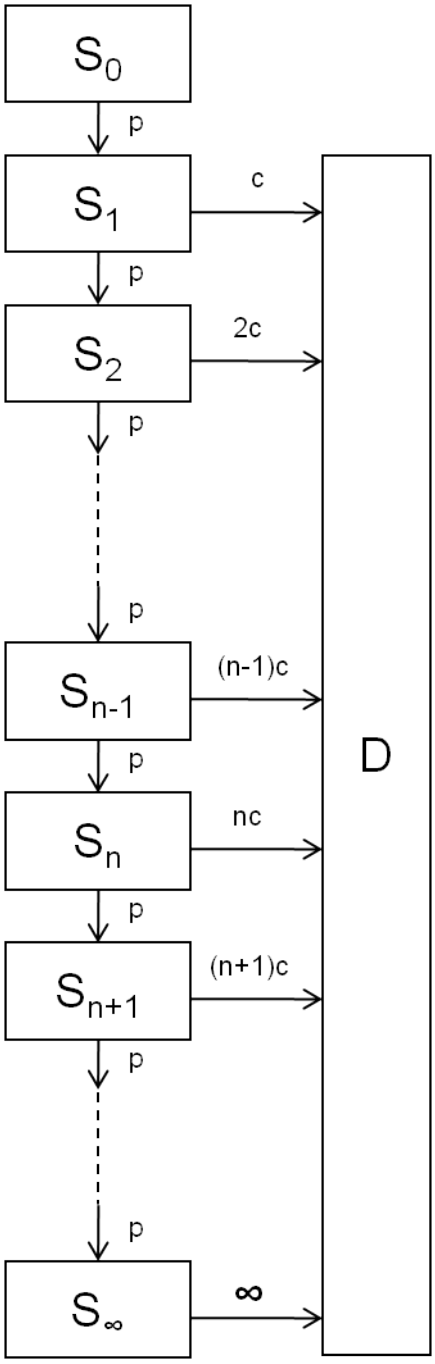

Figure 5.1: Schematic showing compartments and transitions for the Original Jung Model

Accordingly, it was necessary to modify the initial conditions such that a small fraction of cells were not lesion free, i.e. that $S_0 \neq 1.0$, otherwise $p = 0$ and the system would be static at the initial conditions and for all time. 1% was assumed to be a sufficiently small percentage of cells to be probabilistically reasonably not lesion free; these cells were assigned to the single lesion compartment, S_1.

Secondly, a lesion removal process was included to account for a possible cell healing process. The rationale for this is that there should be a probability that some cells will continue to survive with nonlethal lesions. In the form of the model proposed by Jung, all cells with nonlethal lesions will die from the process of a lesion becoming fatal as time is extended indefinitely because the lesion transformation probability remains finite. The probability of a lesion being healed is assumed here to be randomly occurring, constant in time for a given temperature, and linear with the number of lesions present in a cell. Additionally, each healing event heals only a single lesion, thus moving a cell from compartment S_n to compartment S_{n-1} with probability nq for each lesion present. Lesions that have become lethal and thereby moved a cell to the dead compartment cannot be healed. A schematic for this 'Modified Jung Model' is shown in Figure 5.2.

From this graphical representation it should be clear that the Modified Jung Model has a number of similarities to the O'Neill Model. These are:

- The path for a cell from a healthy state to dead is multi-step process consisting of two (or more) state transitions
- All state transitions except for that to the dead state are reversible
- Damaging processes are linearly influenced by the volume-averaged state of surrounding cells

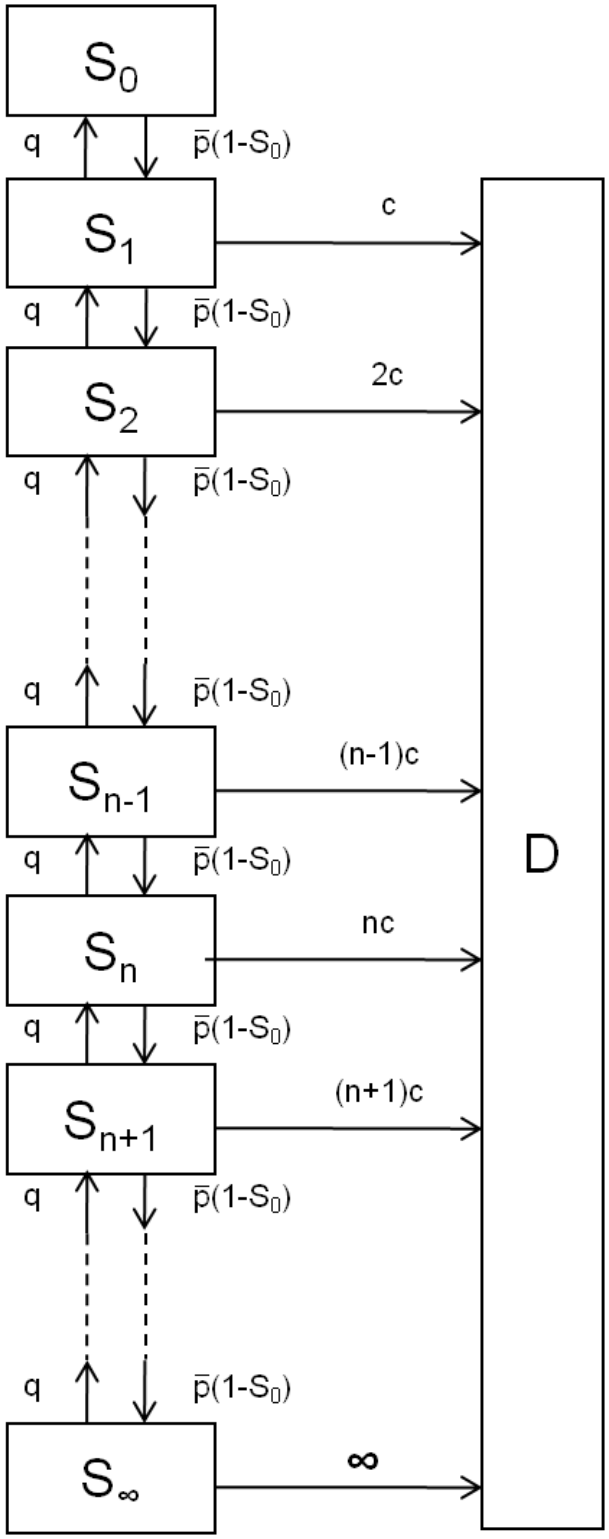

Figure 5.2: Schematic showing compartments and transitions for the Modified Jung Model

With these properties, the Modified Jung Model can be viewed as being made multi-scale; modelled processes of lesions occur on a single lesion, subcellular level, but also considered is 'higher', mutlicellular level which incorporates the volume averaged local cell health $(1 - S_0)$ into the likelihood of lesion creation.

5.3 RESULTS OF FITTING

The Original Jung Model and the Modified Jung Model were both evaluated for states S_0 to S_9; this choice is explained in the discussion. The models were numerically evaluated in the form $d\mathbf{S}/dt = [M]\,\mathbf{S}$ using a fourth-order Runge-Kutta method, where $[M]$ is a 10×10 matrix containing relevant combinations of p, c, and q; for the Original Jung Model this is given by Equation 5.1, and for the Modified Jung Model by Equation 5.2.

$$[M]_{OJM} = \begin{bmatrix} -p & 0 & 0 & \cdots & 0 & 0 \\ p & -p-c & 0 & & 0 & 0 \\ 0 & p & -p-2c & & 0 & 0 \\ \vdots & & & \ddots & & \vdots \\ 0 & 0 & 0 & & -p-8c & 0 \\ 0 & 0 & 0 & \cdots & p & -9c \end{bmatrix} \tag{5.1}$$

$$[M]_{MJM} = \begin{bmatrix} -p & q & 0 & \cdots & 0 & 0 \\ p & -p-q-c & q & & 0 & 0 \\ 0 & p & -p-q-2c & & 0 & 0 \\ \vdots & & & \ddots & & \vdots \\ 0 & 0 & 0 & & -p-q-8c & q \\ 0 & 0 & 0 & \cdots & p & -9c \end{bmatrix} \tag{5.2}$$

However, in Equation 5.2, p depends upon $\mathbf{S}$ and as a result, $d\mathbf{S}/dt = [M(\mathbf{S})]\mathbf{S}$ cannot be inverted, and necessitates use of a numerical solver.

The Original Jung Model and the Modified Jung Model were both fitted to the averaged experimental data from both the data given in chapter 3, and the data described in subsection 4.2.1. Using the same method as before, the closeness of fit was assessed using least squares error; the optimised parameters were determined by use of this error function with the MATLAB function 'fminsearch'.

Since neither the Original Jung Model, nor the Modified Jung Model include any explicit temperature dependence, the data for experiments at different temperatures were treated separately for the fitting exercise, i.e. the models were fitted to 15 data sets, each of length 4. Ideally, any temperature dependence of parameters would thus be assessed subsequently by inspection of trends in the optimised parameter values.

The error-minimising parameter values and associated RMS errors are given in Tables 5.1 and 5.2, whilst Figures 5.3 and 5.4 show comparisons between the predictions and experimental data.

Two of the sets of parameters given in Table 5.1 are the results of constrained optimised error-minimisation. The data sets of 100 °C heating for MRC-5 cells and for HepG2 cells produced values for the parameter p that were restrained by a hard limit of $150\times 10^{-3}\,\mathrm{s}^{-1}$ that was manually set; these values are denoted by the superscript asterisk in the table. A further two data sets both had values of p that were close to the hard limit — 100 °C heating for LX-1 cells ($128.34\times 10^{-3}\,\mathrm{s}^{-1}$) and 85 °C heating for HepG2 cells ($150.0\times 10^{-3}\,\mathrm{s}^{-1}$). Additionally, the parameter values were constrained such that $p \geq c$ always; examples of this limitation influencing the optimised parameters are: 55 °C heating temperature for HepG2 cells, and 55 °C and

			Heating Temperature (°C)				
Data Set	Parameter	Unit	55	65	75	85	100
MRC-5	p	$\times 10^{-3}$ s^{-1}	4.26	7.39	11.62	12.64	150*
	c	$\times 10^{-3}$ s^{-1}	0.07	0.43	0.75	0.87	1.51
	RMS error	%	3.08	14.20	17.15	12.79	0.47
HepG2	p	$\times 10^{-3}$ s^{-1}	1.91	8.88	12.45	149.9	150*
	c	$\times 10^{-3}$ s^{-1}	1.91	0.62	0.83	1.02	1.41
	RMS error	%	10.90	7.11	13.0	2.07	0.88
LX-1	p	$\times 10^{-3}$ s^{-1}	1.01	1.34	10.95	16.35	128.34
	c	$\times 10^{-3}$ s^{-1}	1.01	1.34	0.77	1.43	9.43
	RMS error	%	9.17	4.55	6.71	2.25	0

Table 5.1: Optimised parameter values and corresponding RMS errors for fits of the Original Jung Model to the data from experiments with pure cultures

			Heating Temperature (°C)				
Data Set	Parameter	Unit	55	65	75	85	100
MRC-5	$\overline{p}$	$\times 10^{-3}$ s^{-1}	8.21	13.04	21.52	24.23	75.06
	c	$\times 10^{-3}$ s^{-1}	0.25	1.44	2.11	2.26	5.29
	$\overline{q}$	$\times 10^{-3}$ s^{-1}	0.001*	0.001*	0.001*	0.001*	0.25
	RMS error	%	1.52	8.67	10.81	7.80	0.30
HepG2	$\overline{p}$	$\times 10^{-3}$ s^{-1}	25.24	24.24	23.32	54.54	68.42
	c	$\times 10^{-3}$ s^{-1}	0.17	0.57	2.33	8.70	6.46
	$\overline{q}$	$\times 10^{-3}$ s^{-1}	0.001*	0.001*	0.001*	1.02	0.25
	RMS error	%	15.33	5.31	7.61	0.12	0.60
LX-1	$\overline{p}$	$\times 10^{-3}$ s^{-1}	138.70	150*	24.99	41.56	150*
	c	$\times 10^{-3}$ s^{-1}	0.30	0.04	1.19	1.64	6.49
	$\overline{q}$	$\times 10^{-3}$ s^{-1}	0.31	0.001*	0.001*	0.001*	0.35
	RMS error	%	0.02	3.66	2.57	2.10	0.18

Table 5.2: Optimised parameter values and corresponding RMS errors for fits of the Modified Jung Model to data from experiments with pure cultures

65 °C heating temperatures for LX-1 cells. The method of constraining certain parameters to a user-defined region of values was by imposing an additional 'cost' to

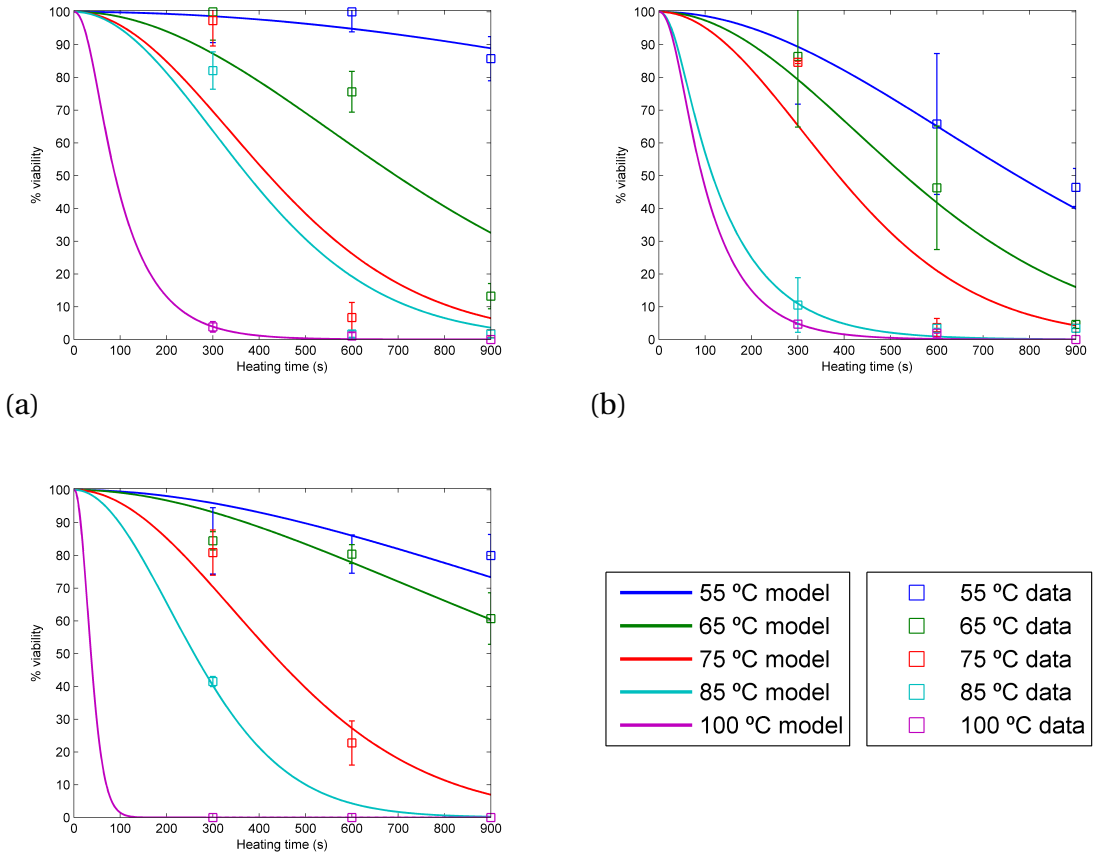

Figure 5.3: Predicted cell viabilities produced with optimised parameters for the Original Jung Model given in 5.1 with corresponding experimental data. Panels show: a) MRC-5 cell cultures, b) HepG2 cell cultures, c) LX-1 cell cultures.

the error function for parameter values outside the predetermined range. The use of manually imposed hard limits is discussed in section 5.4.

Considering the heating of MRC-5 cells, only the model fits for 55 °C and 100 °C of heating fit the data particularly well; RMS errors of the optimal fit for the three other data sets are 12 % or greater. The closeness of fit for the highest and lowest temperatures, and the poorness of fit for the intermediate three heating temperatures are clearly seen in the corresponding panel in Figure 5.3. In all three cases, the model overpredicts the amount of cell death (underpredicts the viability) at 300 s yet two of them (75 °C and 85 °C) underpredict the degree of cell death at 600 s, and to

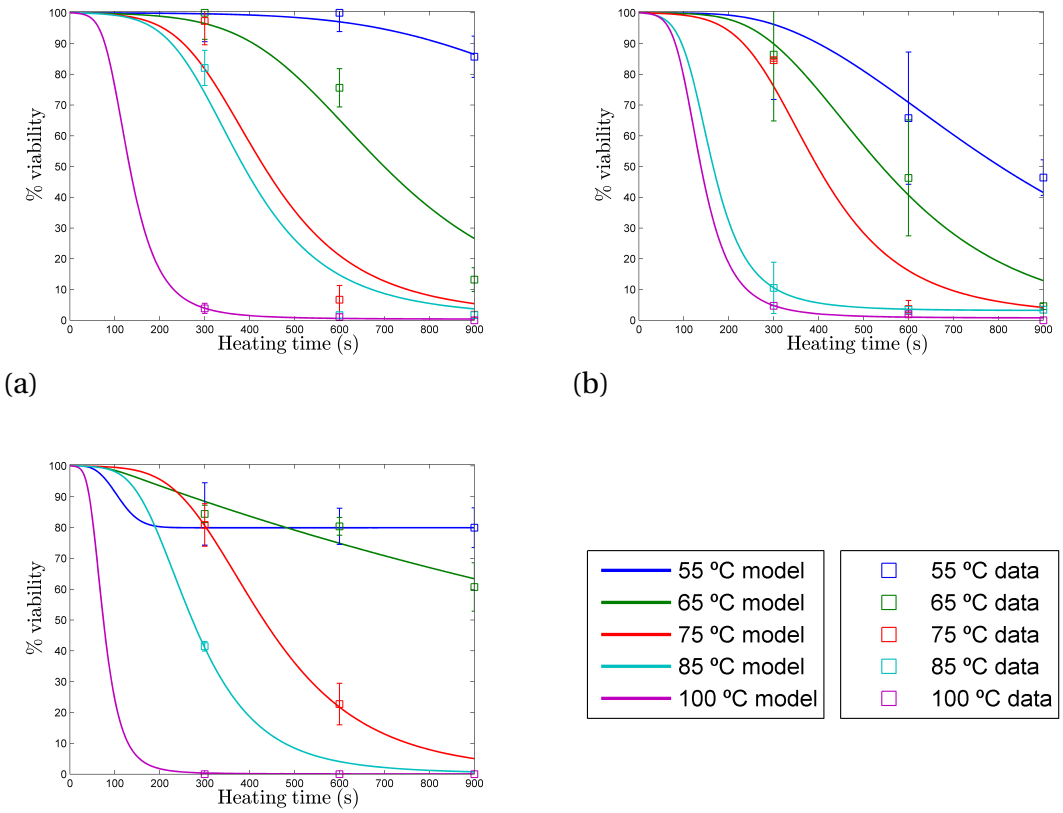

Figure 5.4: Predicted cell viabilities produced with optimised parameters for the Modified Jung Model given in 5.2 with corresponding experimental data. Panels show: a) MRC-5 cell cultures, b) HepG2 cell cultures, c) LX-1 cell cultures.

a lesser extent, underpredict cell death at 900 s. Qualitatively, the model predictions of cell viability drop-off could be described as insufficiently 'sharp' for this temperature of heating.

The numerical evaluation for the fits of the Original Jung Model to the HepG2 data appears to be quite poor — Table 5.1 shows three fits having RMS errors above 5 % with two of these fits having errors above 10 %. However, examining the experimental error of the data it is clear that there is a large uncertainty in values reported for the experimental data; this is graphically shown by the large errors bars in the corresponding panel of Figure 5.3.

Most of the data points from heating LX-1 cells are fitted within the experimental errors, as shown by the reported RMS error values in Table 5.1 where the largest value is 9.17 % and three of the values are below 5%. This closeness of fit is also shown clearly in the corresponding panel of Figure 5.3 where only three data points sit noticeably outside the error bars: those for 300 s of heating at 75 °C, 600 s of heating at 85 °C, and 900 s of heating at 75 °C. Indeed, across all three cell types, the experiments at 75 °C have the least good fit as shown qualitatively by the three plots.

Examining the closeness of fits of the Modified Jung Model given by the RMS errors in Table 5.2, it is clear that the data for experiments on cells from the MRC-5 cell line fit well for 55 °C and 100 °C, but less well for the intermediate temperatures. However, compared to fits of the Original Jung Model, the errors are much lower; the reductions are of 50 %, 39 %, 37 %, 39 %, and 36 % respectively. Graphically, it is clear from comparing the corresponding panels in Figures 5.3 and 5.4 that the plots in the latter achieve a greater degree of 'sharpness' as was highlighted previously as being lacking. Despite this, the plots for the three intermediate heating temperatures remain insufficiently 'sharp' such that there are over predictions of cell death at 300 s of heating for all three temperatures and underpredictions of cell death at 600 s of heating 75 °C or 85 °C.

The RMS errors for fits of the Modified Jung Model to the other experimental data also show large reductions signifying closer fits across all heating temperatures and cell types with three exceptions — those of a 55 °C heating temperature for HepG2 cells and for LX-1 cells, and of a 100 °C heating temperature for LX-1 cells. The other relative reductions are 25 %, 40 %, 94 %, and 32 % respectively for HepG2 cells and 24 %, 28 %, and 62 % for LX-1 cells. Of the improved fits, the maximum RMS error is 10.80 % for heating MRC-5 cells to a temperature of 75 °C; this is the only RMS error greater than 8 %, whilst eight of the fits achieve RMS errors be-

low 5 %. The two poorer fits of 55 °C heating temperature can be seen in Figure 5.4 to have unusual shaped data. The data point for HepG2 cells at a time of 300 s and a heating temperature of 55 °C was artificially raised from a lower recorded experimental value in the pre-processing described previously in section 3.2.

The fact that this adjustment was necessary suggests that the original data may have had poor reliability; the same is true of the data point corresponding to the heating of LX-1 cells for a time of 600s at a temperature of 55 °C. The knock-on effect in both cases is a resulting set of 4 data points that require a fitted line of a different shape to those required by the other data sets. Thus, the Modified Jung Model, which was created to fit the majority of the data sets more closely, is unable to produce a line that fits these two, unusual data sets well. Finally, it should be noted that 10 of the 15 data sets to which the Modified Jung Model was fitted, resulted in values for the parameter q of $0.001 \times 10^{-3}\,\mathrm{s}^{-1}$ which was the imposed minimum limit. Further, the fitting to one data set produced a parameter value for the parameter p that was restrained by the imposed upper limit of $150 \times 10^{-3}\,\mathrm{s}^{-1}$.

Some of the sets of parameter values given in Tables 5.2 and 5.3 showed monotonically increasing parameter values with temperature. Additionally, a number of of data sets resulted in no good fit, or parameter values that were constrained by hard limits,as denoted with an asterisk. Since no simple temperature-dependent trends are obvious across the data sets other than a generally increasing trend, further modification was required to produce conclusive fitting results. Two options were available and both were attempted.

Firstly, the Modified Jung Model was simplified such that only two parameters were varied in a repeat fitting exercise. As q was assumed invariant with temperature in the O'Neill model, the healing parameter was fixed at a constant value and the reduced model was fitted to the data. Initially q was set to zero in order to show

the effect of the inclusion of $(1 - S_0)$ in isolation, and then q was set to an arbitrarily constant value of 0.1. Results from these fittings are given in Table 5.3 and Figure 5.5 for $q = 0$ and in Table 5.4 and Figure 5.6 for $q = 0.1$.

			Heating Temperature (°C)				
Data Set	Parameter	Unit	55	65	75	85	100
MRC-5	$\overline{p}$	$\times 10^{-3}$ s^{-1}	8.22	13.04	21.45	24.14	73.39
	c	$\times 10^{-3}$ s^{-1}	0.25	1.44	2.17	2.29	5.38
	q	$\times 10^{-3}$ s^{-1}	$0^{\dagger}$	$0^{\dagger}$	$0^{\dagger}$	$0^{\dagger}$	$0^{\dagger}$
	RMS error	%	1.52	8.67	10.80	7.80	0.30
HepG2	$\overline{p}$	$\times 10^{-3}$ s^{-1}	150*	24.24	23.32	52.47	67.17
	c	$\times 10^{-3}$ s^{-1}	0.07	0.57	2.33	9.79	6.99
	q	$\times 10^{-3}$ s^{-1}	$0^{\dagger}$	$0^{\dagger}$	$0^{\dagger}$	$0^{\dagger}$	$0^{\dagger}$
	RMS error	%	7.72	5.30	7.61	0.12	0.60
LX-1	$\overline{p}$	$\times 10^{-3}$ s^{-1}	18.00	150*	25.00	41.55	150*
	c	$\times 10^{-3}$ s^{-1}	15*	0.04	1.19	1.64	6.49
	q	$\times 10^{-3}$ s^{-1}	$0^{\dagger}$	$0^{\dagger}$	$0^{\dagger}$	$0^{\dagger}$	$0^{\dagger}$
	RMS error	%	7.38	3.67	2.57	2.10	0.18

Table 5.3: Optimised parameter values and corresponding RMS errors for fits of the Modified Jung Model to data from experiments with pure cultures where q is fixed at $q = 0$

Secondly, the Modified Jung Model was further amended to include a temperature dependence such that the model could be fitted to the whole data set simultaneously, thereby fitting parameters to sets of 24 data points rather than to sets of 4 data points. The temperature dependence was taken from that used in the O'Neill model; the rate constants p, c, and q therefore becoming:

$$p = \overline{p}\,(1 - S_0)\exp^{(T/T_k)} \tag{5.3}$$

$$c = n\overline{c}\exp^{(T/T_k)} \tag{5.4}$$

$$q = q \tag{5.5}$$

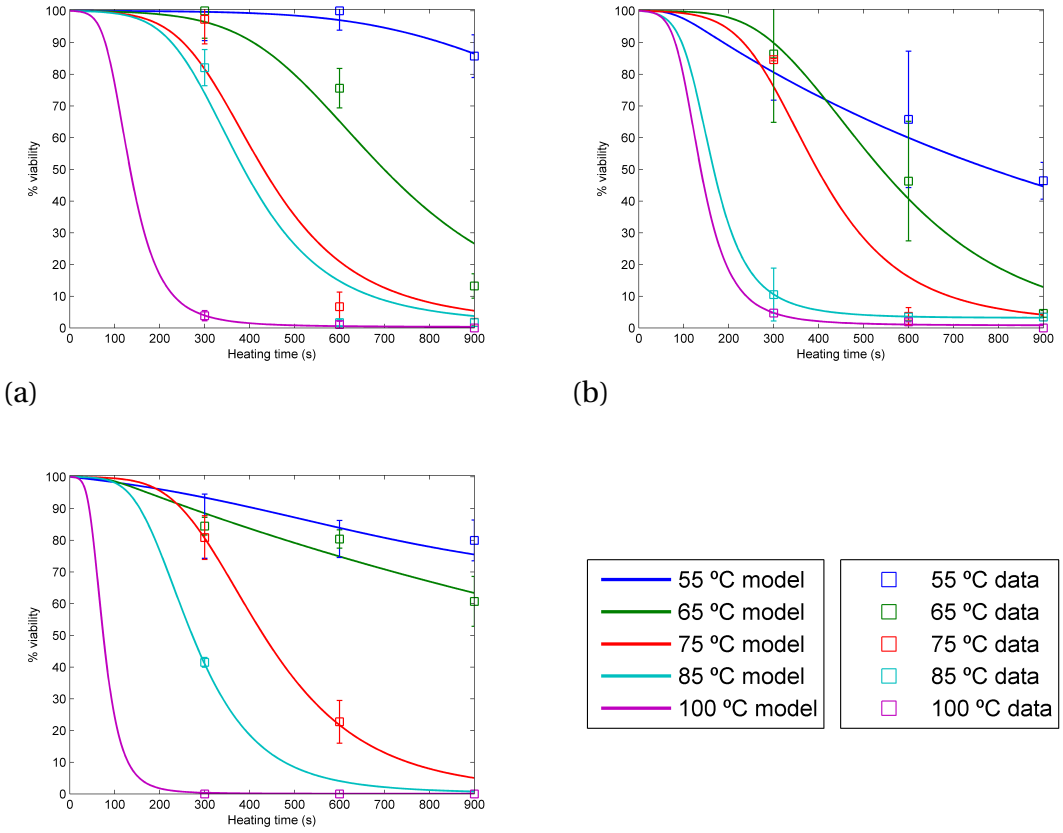

Figure 5.5: Predicted cell viabilities produced with optimised parameters for the Modified Jung Model given in 5.3 with corresponding experimental data. Panels show: a) MRC-5 cell cultures, b) HepG2 cell cultures, c) LX-1 cell cultures.

Results from fitting the model with this temperature dependence are given in Table 5.5, whilst Figure 5.7 shows theoretical plots created with these parameter values with the experimental data.

With the backward rate constant set to zero (results given in Table 5.3 and Figure 5.5), the data for all temperatures and cell cultures were fit with $\leq 10\,\%$ RMS error with one exception (75 °C). However, four further data sets had either p or c restrained by imposed hard limits. The three with p limited at $150\,s^{-1}$ are obvious graphically: as the high value of p results in very low values of c, the plots are graphically very different. Heating temperatures of 100 °C resulted in good quality

			Heating Temperature (°C)				
Data Set	Parameter	Unit	55	65	75	85	100
MRC-5	$\overline{p}$	$\times 10^{-3}$ s^{-1}	8.30	13.16	21.59	24.28	73.69
	c	$\times 10^{-3}$ s^{-1}	0.25	1.46	2.18	2.30	5.53
	$\overline{q}$	$\times 10^{-3}$ s^{-1}	0.1†	0.1†	0.1†	0.1†	0.1†
	RMS error	%	1.53	8.79	10.91	7.91	0.30
HepG2	$\overline{p}$	$\times 10^{-3}$ s^{-1}	150*	23.39	23.46	52.64	67.53
	c	$\times 10^{-3}$ s^{-1}	0.16	0.63	2.34	9.69	6.43
	q	$\times 10^{-3}$ s^{-1}	0.1†	0.1†	0.1†	0.1†	0.1†
	RMS error	%	6.35	5.41	7.70	0.12	0.60
LX-1	$\overline{p}$	$\times 10^{-3}$ s^{-1}	18.11	150*	24.86	41.65	150*
	c	$\times 10^{-3}$ s^{-1}	15*	0.13	1.24	1.66	6.47
	q	$\times 10^{-3}$ s^{-1}	0.1†	0.1†	0.1†	0.1†	0.1†
	RMS error	%	7.37	3.70	2.67	2.17	0.19

Table 5.4: Optimised parameter values and corresponding RMS errors for fits of the Modified Jung Model to data from experiments with pure cultures where q is fixed at $q = 0.1$

		Cell Line		
Parameter	Unit	MRC-5	HepG2	LX-1
$\overline{p}$	$\times 10^{-3}$ s^{-1}	0.86	1.04	0.61
$\overline{c}$	$\times 10^{-3}$ s^{-1}	0.10	0.11	0.10
$\overline{q}$	$\times 10^{-3}$ s^{-1}	0.001	0.001*	2.07
T_k	$^{\circ}$ C	24.5	23.2	21.12
RMS error	%	22.5	16.5	19.1

Table 5.5: Optimised parameter values and corresponding RMS errors for fits of the Modified Jung Model with temperature dependence to experimental data

fits (below 1 % RMS error). The LX-1 data produced three data sets with fits having RMS errors under 4 %, but the MRC-5 and HepG2 data each produced three data sets with RMS errors greater than 5 %. The results in Table 5.3 do not differ greatly from those in Table 5.2, which on closer examination should not be a surprise because 10 of the 15 data sets in Table 5.2 had an optimised value of q of 0.001, which

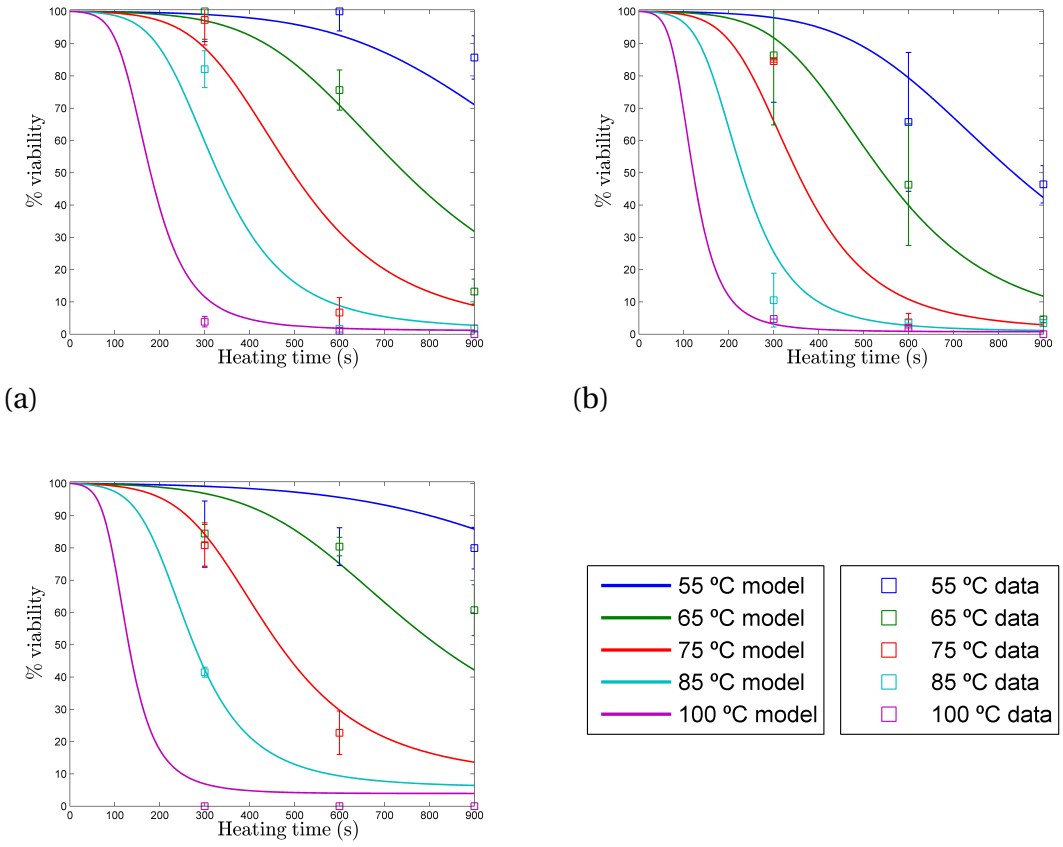

Figure 5.6: Predicted cell viabilities produced with optimised parameters for the Modified Jung Model given in 5.4 with corresponding experimental data. Panels show: a) MRC-5 cell cultures, b) HepG2 cell cultures, c) LX-1 cell cultures.

was the imposed minimum value and of almost negligible magnitude compared to the other parameter values.

For the results produced with the backward rate constant set to a fixed value of $0.1 \times 10^{-3}\,\mathrm{s}^{-1}$ (Table 5.4 and Figure 5.6) the quality of fits showed little change with respect to those in the previous table. The majority of RMS errors indeed increased, albeit by less than one percentage point each. As previously, three sets of data had a value for the parameter p that was restrained by the manually imposed upper limit of $150 \times 10^{-3}\,\mathrm{s}^{-1}$ and one set of data had a restrained value for the parameter c. Graphically, Figure 5.6 shows three data sets with fits that are of inconsistent shape

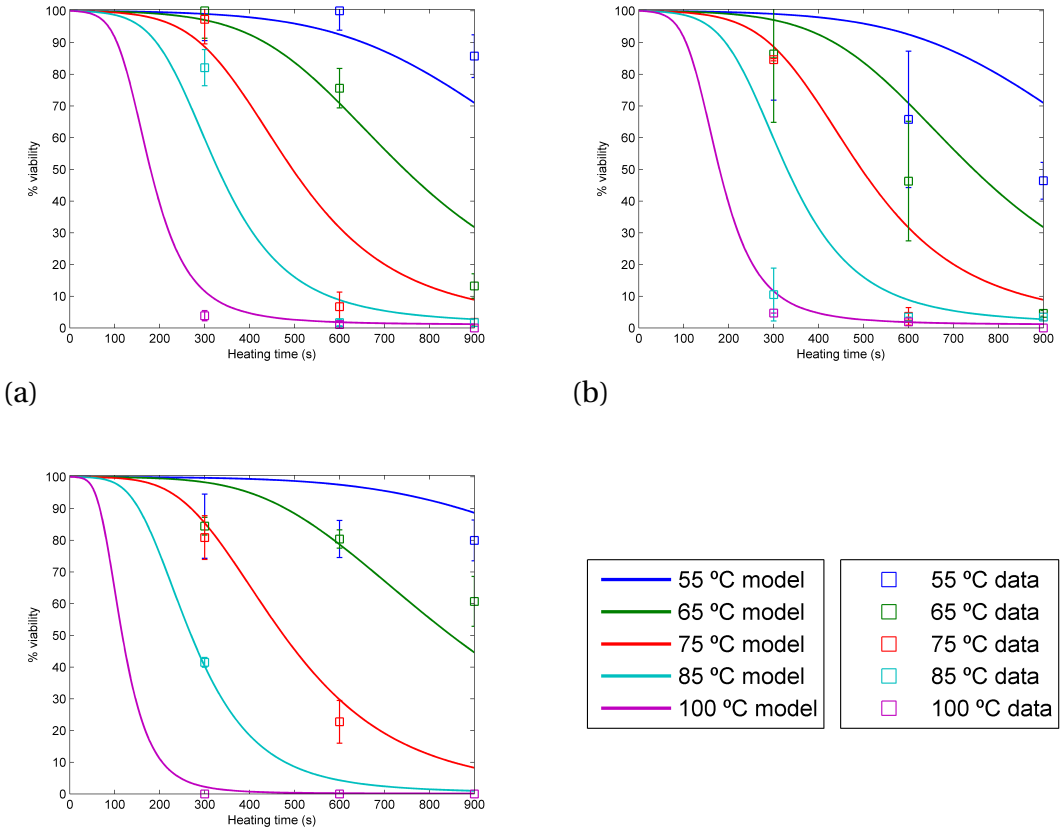

Figure 5.7: Predicted cell viabilities produced with optimised parameters for the Modified Jung Model given in 5.5 with corresponding experimental data. Panels show: a) MRC-5 cell cultures, b) HepG2 cell cultures, c) LX-1 cell cultures.

with respect to the other fits. Further discussion and conclusions, including the inclusion of the parameter q, are made later in section 5.4.

At first inspection, the results from fitting the rate constants with a postulated temperature dependence to the data (Table 5.5 and Figure 5.7) initially appear poor. RMS values for all three cell types are in excess of 15%. However, considering that these results arise from fitting a 4-parameter model to a 24-point data set, rather than a 3- or 4-parameter model to a 4-point data set, this is less surprising. With the exception of the backward rate constant, q, the numerical values of the parameters

are broadly consistent across the three data sets. $\overline{p}$ varies by less than a factor of two, whilst $\overline{c}$ and T_k are consistent to one significant figure.

5.4 DISCUSSION

Before commenting on the results obtained from fitting the Jung models to the data, it is important to note that there are a number of assumptions included in section 5.2. In the coding of the two Jung models, the infinite number of states was truncated to a system with 10 alive states and one dead state. In simulations it was found that the largest value for the fraction of cells in state S_9 at any point was 0.0005 and this was deemed sufficiently small such that more states were not required. More states, whilst reducing truncation errors, would increase the size of the numerical system to be solved and thereby increase computational time.

Secondly, with the inclusion of the dependence upon the health of surrounding tissue (the factor $(1 - S_0)$ in the expression for p), the initial conditions for the Modified Jung Model required $S_0 < 1.0$, for if S_0 were to be unity, p would be null for all time and thereby S_0 would stay at unity for all time. This is the same requirement as for the O'Neill Model to function and so the same initial conditions that were used successfully in the O'Neill Model were used in the Modified Jung Model where $S_0 = 0.99$; for simplicity the initial condition $S_1 = 0.01$ was used to account for all other cells.

Thirdly, the error function used to fit the models to the data included some hard limits on parameter values. Limits were set such that parameter values were kept within a few orders of magnitude of each other. Instances of results being affected by these limits were denoted by asterisks in the corresponding table element. Cases where such limits were not implemented resulted either in parameter values

becoming negative (which is non-physiological) or heading toward infinite values which are similarly unrealistic. Additionally, simulation times increased by orders of magnitude for seemingly little gain. The tendency of the optimisation function to search for extreme parameter values arose primarily in the sets for the highest, or the lowest heating temperatures and is a direct result of the lack of a temperature dependence in the rate constants. For the final investigation where a postulated temperature dependence is assumed for p and c, the restraints on parameter values were not necessary.

Additionally, some of the figures show lines of best fit that are dissimilar to the typical shape shown by the majority of lines of best fit — see the blue line corresponding to a heating temperature of 55 °C in panel (a) of Figure 5.5 for an example. Such instances are direct results of fitting to short data sets (of length 4 data). Notably, no lines in Figure 5.7 behave in this way which is a direct result of fitting to a large data set (of size 20 data). Instances only occur in data corresponding to heating temperatures of 55 °C, and 65 °C, where cell viabilities do not reach low values. The data here correspond only to the 'shoulder' region of the heating curve and this fitting issue would not arise if experiments at these temperatures had been carried out with heating times exceeding 900 s where the second half of the heating curve would have been sampled. When examining consistency of optimised parameter values, these fitted lines would be best removed from consideration as the plot presented does not represent more than the initial stages of cell death.

As shown by the Tables 5.1 and 5.2 and Figures 5.3 and 5.4, both the Original Jung Model and the Modified Jung Model can be fitted to the experimental data in the same way as the O'Neill Model was. However, as is evident both qualitatively from the graphs and numerically from the tables, the Modified Jung Model can be fitted more closely to the data than the Original Jung Model. The fit of the Modified

Jung Model however is still a poorer quality fit than the fit to the data than is the O'Neill Model.

The Modified Jung Model has one additional variable compared to the Original Jung Model, and thus this finding would be expected. To generate a fairer like for like comparison, only two parameters from the Modified Jung Model should be adjusted to generate fits — recall that the O'Neill Model is a three parameter model, but for fitting to a data set at a fixed heating temperature, the model is reduced by one parameter. Tables 5.3 and 5.4 and Figures 5.5 and 5.6 showed fits of the Modified Jung Model to the data where only two parameters of the model were optimised. In these fits, the healing parameter, q, was set at a constant value as this is the parameter that was most frequently forced against an manually imposed limit in the initial fits of the Modified Jung Model. Separately q is fixed at 0 and at 0.1. The latter was arbitrarily selected as a small value representative of typical values found in the initial fits; the arbitrary selection of the value for q is justified because in this exercise the other parameters scale, albeit non-linearly, with the fixed numerical value of q. The fits with $q = 0$ show how the Modified Jung Model behaves with only one of the two proposed modifications. Again, fits consistently closer match the data than those achieved with the Original Jung Model, but are outperformed by the O'Neill Model.

To eliminate the issue of overly sparse data sets and to facilitate a closer like for like comparison with the O'Neill model, Table 5.5 and Figure 5.7 incorporate a temperature dependence into the Modified Jung Model. To draw similarities between the two models the temperature dependence used was the same as in the O'Neill model. Numerically, these results achieved fits that were less close to the data than the fits achieved with the O'Neill model but the parameter values are broadly consistent across the three data sets. Whilst the RMS errors are not particularly satisfactory, the consistency of the parameter values demonstrates that the Modified Jung

Model with temperature dependant rate constants treats the three different data sets approximately equally well.

A different temperature dependence was also tested, as is used in traditional Arrhenius based models:

$$k \propto e^{-E_a/T}, \tag{5.6}$$

however, 'optimised' parameter values showed no consistency in values across different fits and varied over many orders of magnitude. As discussed in chapter 2 such results are of little practical use because in order to utilise models in predictive capacities, models must be capable of producing reliable predictions. Inconsistent parameter values that vary by many orders of magnitude mean it is very difficult to generate appropriate parameter values for a previously unmodelled scenario such as are encountered clinically.

The main problem with all 'Jung Models' is qualitatively obvious from the figures. It is that the models cannot mimic the rapid acceleration of cell death as cell death starts to occur, nor do the models display the necessary decrease in rate of cell death at high cell fractions of dead cells. The data of intermediate heating temperatures of 75 °C and 85 °C generally are the least well fit. The inclusion of the (1-S_0) term addresses this issue to some extent hence its inclusion in the Modified Jung Model; however, as the graphs show, this characteristic is not captured as well by the Modified Jung Model as by the O'Neill Model.

The modelling presented in subsection 5.2.2 was deliberately limited to simple modifications of the Original Jung Model presented in subsection 5.2.1; specifically, through alterations that drew similarities to the form of the O'Neill Model. Whilst it may be possible to modify the Jung Models differently in order to obtain closer

fits, this would not be without either additional parameters or deviation from the purpose of linking the mechanistic Jung Model to the empirical O'Neill model.

The commonality of all three models is that they each have one compartment for perfectly healthy, alive cells, and one compartment for dead cells. Whilst the Jung models have an infinite number of compartments for cells with lesions, the O'Neill Model has a single, vulnerable, compartment. Using the Jung models as mechanistic analogies for the empirically-derived O'Neill Model, it is proposed here that the middle, vulnerable compartment accounts for many different cells in varyingly damaged degrees. Thus the vulnerable state in the O'Neill Model can be thought of as analogous to the sum of states S_1 to S_∞. This does not conflict with how the model was developed, because this vulnerable compartment was defined at the outset to be arbitrary in nature. Thus, by use of Modified Jung Model, a degree of insight has been acquired into the mechanistic events that occur on, and are observable at, the cellular level and are encompassed within the state transitions of the O'Neill Model.

5.5 CONCLUSION

In this final chapter that deals with the modelling of cell death, the O'Neill Model was compared to a pre-existing model from the literature — that as proposed by Jung in 1986. The Jung Model was used in its original form and in a form modified for this thesis. Both forms are mechanistic and are based around single events, observable on the scale of a single cell, unlike the empirically derived O'Neill model. The modifications made for the Modified Jung Model cause qualitative changes to the lines of best fit such that the Modified Jung Model might suggest an explanation for mechanistic behaviour behind the O'Neill Model. Similarities are shown between the Modified Jung Model and the O'Neill model, the result of which is that the

two models, both of which have been shown to fit the same experimental data, can be incorporated together as part of a single, unifying, multiscale model. Through the Modified Jung Model, this multiscale model is capable of predicting the singularly occurring events of lesion creation and through use of the O'Neill Model, tissue level computation of predicted cell death is easily implementable. Further development of the multiscale model is contingent upon obtaining more, and different experimental data.

CHAPTER 6

THERMAL ŒDEMA MODEL

The work presented in sections 6.2 - 6.4 has appeared with minor amendments as **O'Neill, D. P.**, Peng, T., and Payne, S. J. (2011). "The Response of Hepatocyte Cell Volume to Hyperthermia and its Role in Oedema" Engineering in Medicine and Biology Society, EMBC, 2011 Annual International Conference of the IEEE, pp. 4305-4308, Aug. 30 2011 - Sept. 3 2011

6.1 INTRODUCTION

Amongst the many equations that have been proposed to model the passive and active transport of ions across cell membranes, some of which were described in chapter 2, a substantial number include a dependence upon temperature. To date, there appear to be no implementations of these models where temperature is used as a variable rather than as simply a parameter, nor even any investigations into their performances under varying temperature. Similarly, but less surprisingly, there is no evidence of a model for active transport that includes any consideration of cell damage or death. As explained previously in chapter 2, existing models have been developed primarily for the purpose of predicting normal homeostatic cellular be-

haviour. In homeostasis, no pathological conditions arise, however this is clearly not the case for RFA treatments.

There exist a number of morphological side effects that arise from RFA, many of which are covered in detail by Ni *et al.* [90]. However, the focus there is the determination of morphology through experimental post-operative histological analysis of excised tissue. Some side effects of RFAs are also detectable through imaging, either intra- or post-operatively. Ultrasound and contrast CT methodologies are more frequently used than MRI due to issues of ablation equipment compatibility with the high magnetic fields of MRI machines. A common clinical observation in ultrasound images is that of a hyperechoic rim as described and shown by Uehara *et al.* [126], Leifer *et al.* [72], and McGahan and Dodd III [77], example images being reproduced in Figure 6.1. The hyperechoic region, which shows up brighter in the ultrasound images reproduced in Figure 6.1, indicates an increased density. Postulated reasons for increased density include an influx of extracellular fluid, increased blood flow, hæmorrhaging blood, and hardened ablated tissue.

Immediately after treatment, contrast-enhanced CT scans are able to detect regions of hyperæmia (increased blood flow). Kim *et al.* [61] show an typical CT image (reproduced in Figure 6.2) where not only is there a hyperechoic rim, but there is also arterioportal shunting resulting for damage caused during either needle insertion or removal. This shunted blood flows directly from the arterial tree to the venous tree that bypasses the capillary and sinusoidal network stages.

In contrast-enhanced CT images taken some time after treatment, similar features are often observed, where a bright annulus surrounds the darker, successfully ablated zone. Such features are sometimes observed in scans taken immediately after treatment, and are frequently still present in the following months post treatment after which significant tissue regeneration, resorption or the presence of scar

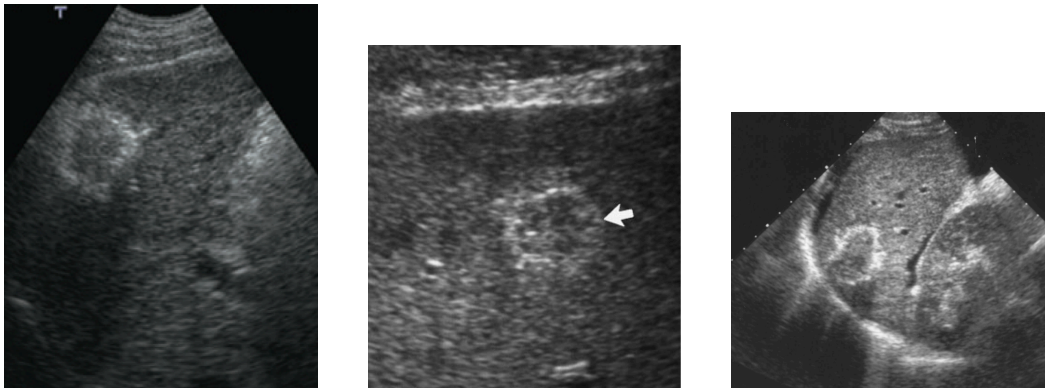

(a) (b) (c)

Figure 6.1: Three examples from the literature of hyperechoic rims observed in ultrasound images. Reproduced from: (a) Uehara *et al.* , Hepatol Res **39**: 954-962; (b) Leifer *et al.* , Radiology **214**: 167-172, arrow shows isoechoic lesion with a hyperechoic rim; (c) McGahan and Dodd III, Am J Roentgenol **176**: 3-16

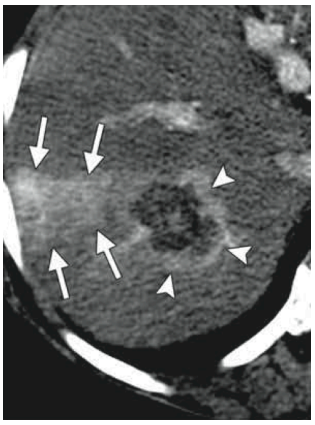

Figure 6.2: Example of hyperæmia immediately after thermal ablation where arrowheads show a relatively thick rim of transient periablational hyperæmia and arrows indicate arterioportal shunting around the RFA zone as a result of injury to smaller vessels; Reproduced from Kim *et al.* , RadioGraphics **31**: 377-390

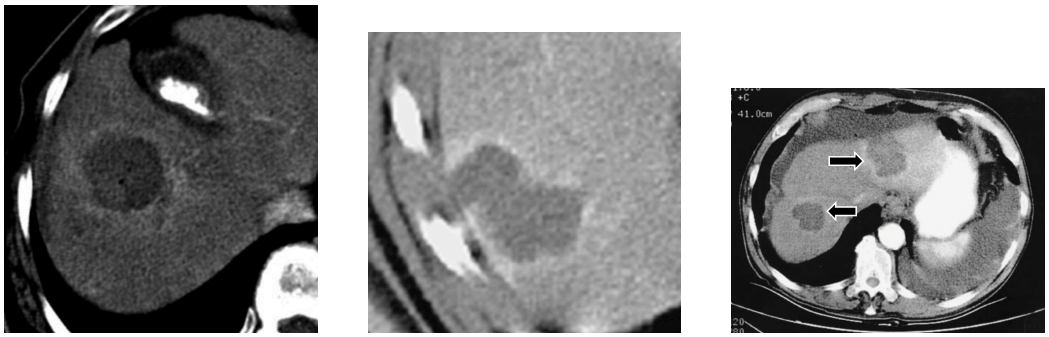

(a) (b) (c)

Figure 6.3: Three examples from the literature of enhanced contrast rims observed in CT images at successively longer times after ablation. (a) 20 mins, Park *et al.* , RadioGraphics **28**:379-392; (b) 10 days, Vogt *et al.* , J Nucl Med **48**: 1836-1844; (c) 1 month, arrows show contrast-enhancing tissue representing inflammatory changes that evolve over time on subsequent CT scans; Curley, Ann Surg Oncol **10**:338-347

tissue diminishes their presence. Example images taken 20 minutes, 10 days, and 1 month after ablation as presented respectively by Park *et al.* [93], Vogt *et al.* [127], and Curley [21] are reproduced in Figure 6.3. Compared to the ultrasound images in Figure 6.1, it is noticeable that the ablated zone inside the bright rim is considerably darker than tissue remote from ablation. Whilst the bright ring in the CT images is present even 1 month after treatment (as shown in the third panel of Figure 6.3), examples from the wider literature show negligible reduction in the width of the rim over the first month, but by 6 months post-treatment, very few patient scans exhibit any bright rims. Notable from all seven images in these figures is the range of ablation shapes possible, not one being the section of a sphere.

Tying the presence of these annular shells to the final lesion size could prove to be of great use clinically, as suggested by Andreano *et al.* [1]. However, there, the authors solely look at correlations between lesion size and ring size and not at any method for predicting the size of such rings. There is no existing literature for the modelling of cellular swelling at the periphery of RFA zones; this chapter thus

contains a novel mathematical model of a hepatocyte to predict the occurrence of œdemata resulting from supraphysiological temperature rises.

The model is assembled from pre-existing nonlinear equations in the literature as well as simple equations that arise from fundamental physical assumptions. The model includes the additional variables of intracellular and extracellular volume fractions in order to model any swelling or shrinkage that result from spatially and temporally varying temperature profiles. First, this new hepatocyte model is detailed; the analysis steps necessary to run simulations with the model and the form of these simulations are next given. Finally, simulation results of this model are presented. In the second part of this chapter, the hepatocyte model is modified to incorporate the cell death model detailed in chapter 2; results from this extended model are then presented. The chapter concludes with a discussion about both the initial model and its extended form.

6.2 INITIAL MODEL

6.2.1 Volume

The model proposed here is derived from the consideration of the volume of a single hepatocyte cell fixed in space and surrounded by a smaller extracellular volume. Thus, per unit volume, V, the intracellular volume V_i and extracellular volume V_e are related by:

$$\frac{V_i}{V} + \frac{V_e}{V} = 1, \tag{6.1}$$

where the substitutions $\frac{V_i}{V} = \phi_i$ and $\frac{V_e}{V} = \phi_e$ are used subsequently, i.e.:

$$\phi_i + \phi_e = 1. \tag{6.2}$$

6.2.2 Ion Currents

Matthews [75] lists the principal cations that have an effect on cell volume as sodium and potassium. Considering the schematic of a cell shown in Figure 6.4 where sodium and potassium are active species that can be transported across the cell membrane, the model presented here uses equations proposed by Endresen *et al.* [34]. In this model, because the rate of heating is slow (of the order of minutes) compared to the time constants of the dynamic equations proposed by Endresen *et al.* (on the order of seconds) the equilibrium concentrations of ion species are of most interest and thus the equations governing ion transport are derived from a steady-state (equilibrium) analysis of Endresen's model. Three

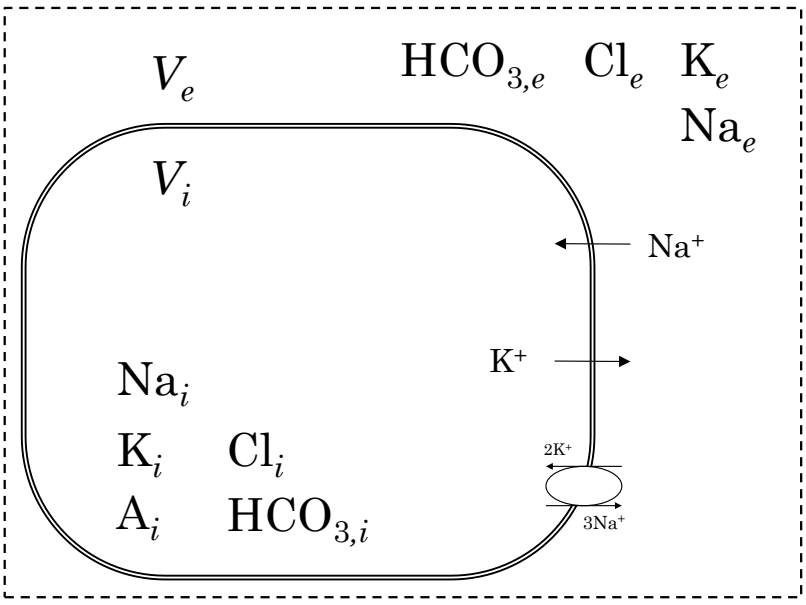

Figure 6.4: Model schematic showing those ion species and transport mechanisms across the cell membrane considered here.

ion transport means are modelled: passive transport through the potassium channels and sodium channels and active transport through the ATP-driven sodium-potassium pump. Each transport has an associated current equation derived by Endresen *et al.* [34] which, assuming steady-state operation and a net outward current being defined as positive, become:

$$i_{\mathrm{K}} = k_{\mathrm{K}} \frac{1}{2} \left(1 + \tanh\left(\frac{2e(v - v_x)}{kT}\right)\right) \sinh\left(\frac{e(v - v_{\mathrm{K}})}{2kT}\right), \tag{6.3}$$

$$i_{\mathrm{Na}} = k_{\mathrm{Na}} \frac{1}{4} \left(1 - \tanh\left(\frac{2e(v - v_h)}{kT}\right)\right)\left(1 + \tanh\left(\frac{2e(v - v_m)}{kT}\right)\right) \sinh\left(\frac{e(v - v_{\mathrm{Na}})}{2kT}\right), \tag{6.4}$$

$$i_{\mathrm{NaK}} = k_{\mathrm{NaK}} \tanh\left(\frac{v + 2v_{\mathrm{K}} - 3v_{\mathrm{Na}} - v_{\mathrm{ATP}}}{\frac{2kT}{e}}\right), \tag{6.5}$$

where k_{K}, k_{Na}, and k_{NaK} are conductance parameters, e is the elementary charge, k is the Boltzmann constant, and T is the temperature. In equations 6.3 and 6.4 the hyperbolic sine term reflects the passage of charges through an open gate. The current of species S, i_{S}, is zero when the driving voltage of S, $(v - v_{\mathrm{S}})$, is zero. Either side of this, the differential is one, thereafter increasing, reflecting the rapidly increasing ease at which electrons pass through the gate at large positive voltages. The hyperbolic tangent terms represent the activation, or inactivation, of gates with increasing membrane potential. A closed gate will prevent the flow of electrons, and must have a conductance of zero, whilst a fully open gate, has a conductance of unity. Hyperbolic tangent functions offset by +1 (and halved in magnitude) provide suitable characteristics for such gates, hence their presence in the above expressions.

Equation 6.5 is derived from an energy balance of the sodium-potassium pump, and also from the assumption that the pump operates around a balance point where the forward and backward reaction rates of ATP breakdown and transport of sodium and potassium against their potential gradients are equal. The hyperbolic tangent results from the devision of an hyperbolic sine, associated with the forward rate

constant, by a corresponding hyperbolic cosine associated with the backward rate constant.

In these equations, the membrane potential is denoted by v, whilst Nernst potentials are given by:

$$v_{\mathrm{Na}} = \frac{kT}{e} \ln \frac{[\mathrm{Na}]_e}{[\mathrm{Na}]_i}, \tag{6.6a}$$

$$v_{\mathrm{K}} = \frac{kT}{e} \ln \frac{[\mathrm{K}]_e}{[\mathrm{K}]_i}, \tag{6.6b}$$

where [Na] and [K] are respectively the concentrations of sodium and potassium ions; subscripts e and i denote extra- and intracellular respectively. Finally, v_x is the half-activation potential for the 'x-gates' which are the primary mechanism by which potassium passively enters the cell. Sodium passively enters the cell through a two-step process (the activation of 'm-gates' and the simultaneous inactivation of 'h-gates', thus v_m is the half-activation potential for the 'm-gates' and v_h is the half-inactivation potential of the h gates. v_{ATP} is the potential corresponding to the ATP-ADP breakdown energy used in the sodium-potassium pump.

Continuing with a steady-state analysis of a single cell, the model does not permit any net influx or efflux of potassium or sodium. Thus, as the sodium-potassium pump operates by pumping out $3\mathrm{Na}^+$ in exchange for pumping in $2\mathrm{K}^+$ and the ion channels transport single ions, dynamic equilibrium for the movement of sodium ions can be expressed as:

$$-3i_{\mathrm{NaK}} - i_{\mathrm{Na}} = 0, \tag{6.7}$$

and similarly for potassium ions:

$$2i_{\mathrm{NaK}} - i_{\mathrm{K}} = 0. \tag{6.8}$$

6.2.3 Osmotic Pressure

The system presented so far consists of seven variables (ϕ_i, ϕ_e, $[\mathrm{Na}]_e$, $[\mathrm{K}]_e$, $[\mathrm{Na}]_i$, $[\mathrm{K}]_i$, and v). In addition to the two active species of sodium and potassium, consideration is given here to the passive species of chloride and bicarbonate and also to the large non-permeating ions present within the cell as these species are modelled and values are given by Melkikh and Sutormina [81] and Matthews [75]. It is assumed that these latter two ions are maintained at constant concentrations by exchangers, gates, and transporters that have negligible effect on the active species modelled.

By assuming the cell wall to have negligible stiffness, the mechanical forces within the cell membrane wall can be neglected and thus the osmotic pressure across the cell membrane is set here at zero:

$$\left([\mathrm{Na}]_e + [\mathrm{K}]_e + [\mathrm{Cl}]_e + [\mathrm{HCO_3}]_e\right) - \left([\mathrm{Na}]_i + [\mathrm{K}]_i + [\mathrm{Cl}]_i + [\mathrm{HCO_3}]_i + [\mathrm{A}]_i\right) = 0, \quad (6.9)$$

where $[\mathrm{Cl}]_i$, $[\mathrm{Cl}]_e$, $[\mathrm{HCO_3}]_i$, $[\mathrm{HCO_3}]_e$ and $[\mathrm{A}]_i$ are respectively the concentrations of intra- and extracellular chloride ions, intra- and extracellular bicarbonate ions and the non-permeable ions. As the large ions are non-permeable the total number of such ions inside the cell does not vary; the concentration can be replaced with the substitution:

$$[\mathrm{A}]_i = \frac{\phi_i^0 [\mathrm{A}]_i^0}{\phi_i}, \quad (6.10)$$

where the superscript ^{0} denotes the parameter value at the initial temperature T^0.

6.2.4 Electro-neutrality

In the model, extracellular volume has constant electro-neutrality, i.e. a net charge of zero for the summation of all extracellular ions. The extracellular electro-

neutrality is written by:

$$([\mathrm{Na}]_e + [\mathrm{K}]_e) - \left([\mathrm{Cl}]_e + [\mathrm{HCO_3}]_e\right) = 0. \tag{6.11}$$

The condition of extracellular electro-neutrality was used by Endresen *et al.* who formed the equation to be consistent with standard assumptions in the literature [33]. Also stated by Endresen *et al.* is that:

> The voltage across the membrane of a cell is caused by, and is directly proportional to, the surplus of charge inside the cell, and due to the

Because the transmembrane voltage as used by Endresen *et al.* is linearly dependant upon the difference between the net extracellular charge and the net intracellular charge, with a constant of proportionality equal to $\frac{FV}{C}$ where F is Faraday's constant, V is the volume of the cell, and C is the capacitance. For Endresen *et al.* this is approximately $20{,}000 mV\ C^{-1}$; as such the difference between net charges is very small relative to concentrations of the species modelling. A condition of intracellular electro-neutrality is therefore another equation given by:

$$([\mathrm{Na}]_i + [\mathrm{K}]_i) - \left([\mathrm{Cl}]_i + [\mathrm{HCO_3}]_i + z_{\mathrm{A}}[\mathrm{A}]_i\right) = 0. \tag{6.12}$$

Both equations of electro-neutrality were used to determine the baseline parameter values in section 6.3.3, however for modelling the dynamics of the system, only two of equations 6.9, 6.12 and 6.11 are required.

6.2.5 Extracellular Diffusion

For the final two equations required, the cell is considered as part of a continuum where extracellular ion concentrations can vary spatially. In this model, extracellular ion motion is dominated by diffusion, thus the remaining two equations are the

diffusion equations for sodium and potassium. For each point in space, there are both intra- and extracellular ions, however diffusion only occurs in the extracellular volume, thus the diffusion equations can be expressed as:

$$\frac{\partial}{\partial t}\left(\phi_e \left[\mathrm{Na}\right]_e\right) = \nabla D_{\mathrm{Na}} \nabla \left[\mathrm{Na}\right]_e + S_{\mathrm{Na}}, \tag{6.13}$$

$$\frac{\partial}{\partial t}\left(\phi_e \left[\mathrm{K}\right]_e\right) = \nabla D_{\mathrm{K}} \nabla \left[\mathrm{K}\right]_e + S_{\mathrm{K}}, \tag{6.14}$$

where D_{Na} and D_{K} are variable diffusion coefficients for sodium and potassium. S_{Na} and S_{K} are source terms which account for the efflux of ions into the extracellular volume from inside the cell. Thus considering sodium ions:

$$S_{\mathrm{Na}} = -\frac{\partial}{\partial t}\left(\phi_i \left[\mathrm{Na}\right]_i\right), \tag{6.15}$$

and similarly, the source term for potassium ions is:

$$S_{\mathrm{K}} = -\frac{\partial}{\partial t}\left(\phi_i \left[\mathrm{K}\right]_i\right). \tag{6.16}$$

Values for coefficients of diffusion are given in the literature with respect to the net fluxes crossing the surface of a control volume which, in relation to the model presented here, includes the combined areas of the extra- and intracellular volumes. However, diffusion occurs solely in the extracellular space; hence as cells swell and the extracellular volume decreases, so too must the effective coefficient of diffusion. By assuming that the effective coefficients of diffusion are linear-weighted averages, the effect of changing extracellular volume can be included by using the following first-order approximations to relate diffusion coefficients to their baseline reported values:

$$D_{\mathrm{Na}} = \frac{\phi_e}{\phi_e^0} D_{\mathrm{Na}}^0, \tag{6.17}$$

$$D_{\mathrm{K}} = \frac{\phi_e}{\phi_e^0} D_{\mathrm{K}}^0. \tag{6.18}$$

Removing the time and space dimensions in equations 6.13 and 6.14 through use of a non-dimensional time, $t' = \frac{t}{\tau}$, and a non-dimensional distance, $r' = \frac{r}{R}$, converts equation 6.13 to:

$$\frac{\partial}{\partial t'}\left(\phi_e [\mathrm{Na}]_e + \phi_i [\mathrm{Na}]_i\right) = \nabla \frac{\phi_e}{\phi_e^0} D'_{\mathrm{Na}} \nabla [\mathrm{Na}]_e, \tag{6.19}$$

using a non-dimensional coefficient of diffusion:

$$D'_{\mathrm{Na}} = \frac{R^2}{\tau} D^0_{\mathrm{Na}}. \tag{6.20}$$

Similarly for potassium, the final expression is:

$$\frac{\partial}{\partial t'}\left(\phi_e [\mathrm{K}]_e + \phi_i [\mathrm{K}]_i\right) = \nabla \frac{\phi_e}{\phi_e^0} D'_{\mathrm{K}} \nabla [\mathrm{K}]_e, \tag{6.21}$$

where the non-dimensional coefficient of diffusion is similarly given by:

$$D'_{\mathrm{K}} = \frac{R^2}{\tau} D^0_{\mathrm{K}}. \tag{6.22}$$

At this point, the system is fully defined with the seven variables listed previously and eight equations: continuity of volume (Equation 6.1), current balances for sodium and for potassium (Equations 6.7 and 6.8), zero osmotic pressure (Equation 6.9), electro-neutrality (Equations 6.12 and 6.11), and diffusion of sodium and of potassium (Equations 6.19 and 6.21). From hereon, since only concentrations are dealt with, the square bracket notation is no longer used, i.e. Na_e replaces $[\mathrm{Na}]_e$ et cetera.

6.3 INITIAL MODEL ANALYSIS

6.3.1 Computational Formulation

The model detailed in section 6.2 contains two partial differential equations, four simple algebraic, and two highly nonlinear constraint equations. Equation 6.2 can

be used as an algebraic substitution to reduce the system, by one variable, to six variables. By differentiating the remaining equations with respect to time it is clear that equations 6.9, 6.12 and 6.11 are linear combinations of each other and only contain two unique equations. Here, equations 6.9 and 6.11 were selected and thus it is possible to formulate the system of six unique equations into the form:

$$\mathbf{M}\dot{\mathbf{u}} = \mathbf{F}_{diff}(\mathbf{u}) + \mathbf{F}_{temp}(\mathbf{u}), \tag{6.23}$$

where $\mathbf{M}$ is a mass matrix for the temporal derivative vector of six variables, $\mathbf{u}$, whilst $\mathbf{F}_{diff}(\mathbf{u})$ is a forcing function that derives from the extracellular diffusion and $\mathbf{F}_{temp}(\mathbf{u})$ is a forcing function that depends upon $\mathbf{u}$ and the temporal derivative of temperature.

The elements variables contained in $\mathbf{u}$ are arbitrarily ordered as:

$$\mathbf{u} = \begin{bmatrix} \mathrm{Na}_e \\ \mathrm{K}_e \\ \mathrm{Na}_i \\ \mathrm{K}_i \\ \phi_i \\ v \end{bmatrix},$$

and the equations used to construct $\mathbf{M}$ are written in the following order:

1. Conservation/diffusion of extracellular sodium (6.13 with the substitutions mentioned above)
2. Conservation/diffusion of extracellular potassium (6.14 with substitutions)
3. Condition of zero osmotic pressure ($\frac{\partial}{\partial t}$ 6.9)
4. Condition of constant extracellular electroneutrality ($\frac{\partial}{\partial t}$ 6.11)

5. No accumulation of intracellular sodium ($\frac{\partial}{\partial t}$ 6.7)

6. No accumulation of intracellular potassium ($\frac{\partial}{\partial t}$ 6.8).

6.3.1.1 Equation manipulation

The two equations dealing with diffusion are already in differential form, however, the spatial derivatives must be converted into the source term $\mathbf{F}_{diff}$. These diffusion terms are linear and so by using the 'method of lines' [117], the spatial derivatives are replaced by finite difference approximations. Due to the geometry of the probes used and of the tumours to be ablated, many target thermal ablation shapes are approximately spherical. Thus, in rotationally symmetric spherical polar coordinates, the extracellular sodium diffusion term of the modified Equation 6.13 becomes:

$$\frac{D'_{\mathrm{Na}}}{\phi_e^0}\nabla\left(\phi_e\nabla\mathrm{Na}_e\right)=\frac{D'_{\mathrm{Na}}}{\phi_e^0}\frac{\partial}{\partial r'}\left(\phi_e\frac{\partial}{\partial r'}\mathrm{Na}_e\right)+\frac{2}{r'}\frac{D'_{\mathrm{Na}}}{\phi_e^0}\phi_e\frac{\partial}{\partial r'}\mathrm{Na}_e. \tag{6.24}$$

At the origin, the singularity of the second term on the right hand side can be dealt with using l'Hôpital's rule such that for $r=0$:

$$\frac{D'_{\mathrm{Na}}}{\phi_e^0}\nabla\left(\phi_e\nabla\mathrm{Na}_e\right)=3\frac{D'_{\mathrm{Na}}}{\phi_e^0}\frac{\partial}{\partial r'}\left(\phi_e\frac{\partial}{\partial r'}\mathrm{Na}_e\right). \tag{6.25}$$

Similarly, the expressions for the diffusion of extracellular potassium are given by:

$$\frac{D'_{\mathrm{K}}}{\phi_e^0}\nabla\left(\phi_e\nabla\mathrm{K}_e\right)=\frac{D'_{\mathrm{K}}}{\phi_e^0}\frac{\partial}{\partial r'}\left(\phi_e\frac{\partial}{\partial r'}\mathrm{K}_e\right)+\frac{2}{r'}\frac{D'_{\mathrm{K}}}{\phi_e^0}\phi_e\frac{\partial}{\partial r'}\mathrm{K}_e, \tag{6.26}$$

$$\frac{D'_{\mathrm{K}}}{\phi_e^0}\nabla\left(\phi_e\nabla\mathrm{K}_e\right)=3\frac{D'_{\mathrm{K}}}{\phi_e^0}\frac{\partial}{\partial r'}\left(\phi_e\frac{\partial}{\partial r'}\mathrm{K}_e\right). \tag{6.27}$$

The differential forms of equations 6.9 and 6.11 can be shown simply as:

$$\frac{\partial\mathrm{Na}_e}{\partial t}+\frac{\partial\mathrm{K}_e}{\partial t}-\frac{\partial\mathrm{Na}_i}{\partial t}-\frac{\partial\mathrm{K}_i}{\partial t}+\frac{\phi_i^0\mathrm{A}_i^0}{\phi_i}\frac{\partial\phi_i}{\partial t}=0, \tag{6.28}$$

and

$$\frac{\partial\mathrm{Na}_e}{\partial t}+\frac{\partial\mathrm{K}_e}{\partial t}=0. \tag{6.29}$$

Owing to the highly non-linear nature of equations 6.7 and 6.8, the differential forms are omitted here for reasons of space; a complete definition of all elements of $\mathbf{M}$ and $\mathbf{F}_{temp}$ is given in Appendix A. Provided that the imposed temperature distribution is continuous in time ($\frac{\partial T}{\partial t}$ is computable), then equation 6.23 can be solved numerically using a stiff solver.

6.3.2 Imposed Temperature Function

For simulations, a temporally and spatially varying temperature function is required as an input to equation 6.23. The spatial variation was set to be a maximum at $r' = 0$ and to tend to zero as $r' \to \infty$, the temperature 'turning off' at r_c. Similarly, in time, the temperature function 'turns on' at $t_{c,1}$ and subsequently 'turns off' at $t_{c,2}$. Modified hyperbolic tangent functions were used for this and the full imposed temperature function is given by:

$$\mathbf{F}\left(r', t'\right) = T^0 + \frac{\Delta T}{8}\left(1 - \tanh\frac{r' - r_c}{r_s}\right)\left(1 + \tanh\frac{t' - t_{c,1}}{t_{s,1}}\right)\left(1 - \tanh\frac{t' - t_{c,2}}{t_{s,2}}\right), \quad (6.30)$$

where T^0 is the baseline tissue temperature, ΔT sets the maximum temperature rise, r_c, $t_{c,1}$ and $t_{c,2}$ set the offsets of the centrepoints of the hyperbolic tangent functions, and r_s, $t_{s,1}$ and $t_{s,2}$ scale the stretches of the hyperbolic tangents. The set of parameter values used to generate the representative temperature profile for the primary simulation in the next section are given in Table 6.1; Figure 6.5 shows the temporal and spatial development of this temperature profile graphically based on parameter values used in Table 6.1.

6.3.3 Parameter Values

Normothermic (T^0) values for intra- and extracellular ion concentrations and the membrane potential of a hepatocyte are reported by Melkikh and Sutormina [81],

Parameter	Value	Unit
r_c	1	cm^0
r_s	0.25	cm^0
$t_{c,1}$	20	min^0
$t_{c,2}$	50	min^0
$t_{s,1}$	2.5	min^0
$t_{s,2}$	2.5	min^0
T_{max}	70	K

Table 6.1: Values for temperature profile parameters used for the initial simulation.

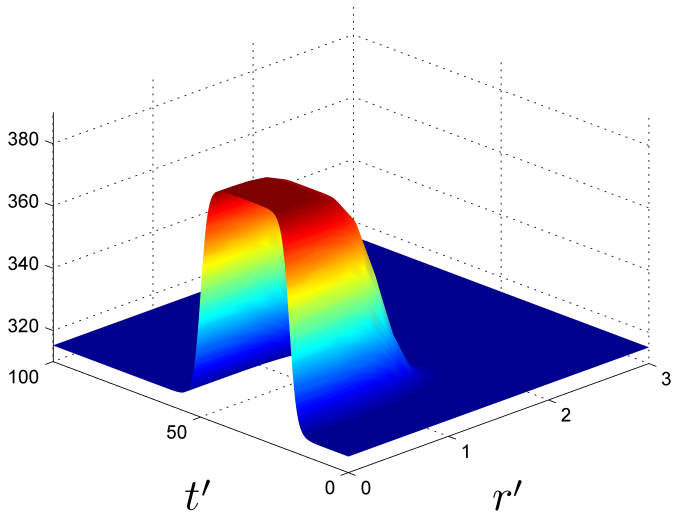

Figure 6.5: Temperature profile imposed to the system.

and Matthews [75] reports that a typical value for A_i is 108 mM. These concentration values satisfy equation 6.11 without modification. However, in order to satisfy equations 6.9 and 6.12 one or more concentration must be adjusted from those used by Melkikh and Sutormina. Keeping extracellular concentrations unchanged so as to keep Equation 6.11 satisfied, it was decided to fix Na_i, Cl_i, and $HCO_{3\,i}$, as reported by Melkikh and Sutormina, whilst K_i and A_i were amended to 128 mM (from 160 mM [81]) and 91.8 mM (from 108 mM [81]) respectively.

Working from parameter values used by Endresen et al. [34], v_x, v_m, v_h and v_{ATP} have been left unchanged. In order to maintain the balance of currents achieved

by Endresen et al. with different Nernst potentials in the liver that result from the different ion concentrations, the conductance parameter values used by Endresen et al. were adjusted. Arbitrarily, k_{NaK} was kept at the value set by Endresen et al. whilst new values of k_{Na} and k_{K} were determined. It should be noted here that the absolute values of ion currents are unimportant in comparison to ensuring that the currents balance to prevent accumulation of species.

As reported by McLennan [78], the model presented here uses 0.86 for the value of ϕ_i^0. Diffusion coefficients were also taken from McLennan's findings, for each of the coefficients a representative value being obtained from the average of the (2 or 4) reported values. Thermal ablation zone radii are typically centimetres in size (RITA protocols exist for 2, 3, 4, or 5 cm) and occur over the duration of minutes; hence the non-dimensionalising length and time constants were set to be 1 cm and 1 s. A complete listing of parameter values that are constant across the various simulations presented is thus given in Table 6.2; the seven parameter values contained in Equation 6.30 are varied between different simulations and are therefore given in the following section to accompany the relevant results.

6.3.4 Initial and Boundary Conditions

Initial conditions for all variables are set to be those at normothermic temperature as given in Table 6.2. Boundary conditions are necessary to compute the discretised diffusion vector $\mathbf{F}_{diff}$. With spherical polar geometry, Neumann boundary conditions were applied at the origin, where spatial derivatives were set at 0. The other boundary condition — at high radius, which is assumed to be sufficiently remote from the origin — was set using Dirichlet boundary conditions, e.g. $\mathrm{Na}_i\,(r \to \infty) = \mathrm{Na}_i^0$.

Variable/Constant	Value	Unit	Source
k	1.38×10^{-20}	mJ K^{-1}	Universal Constant
e	1.60×10^{-19}	C	Universal Constant
T^0	310	K	Normothermic body temperature ($\approx$ 37 C°)
Na_e^0	143	mM	[81]
K_e^0	4.0	mM	[81]
Cl_e^0	20.0	mM	[81]
$HCO_{3,e}^0$	25.0	mM	[81]
Na_i^0	29.0	mM	[81] (adjusted)
K_i^0	128	mM	recalculated
Cl_i^0	120	mM	[81]
$HCO_{3,i}^0$	27.0	mM	[81]
A_i^0	91.8	mM	[75] (recalculated)
k_{Na}	27100	pA	recalculated
k_K	1060	pA	recalculated
k_{NaK}	11.46	pA	[34]
υ_x	-25.1	mV	[34]
υ_h	-91.0	mV	[34]
υ_m	-41.4	mV	[34]
υ_{ATP}	-450	mV	[34]
ϕ_i^0	0.86	cm^3/cm^3	[78]
D_{Na}^0	10.5×10^{-4}	$cm^2\ min^{-1}$	[78] (averaged)
D_K^0	3.7×10^{-4}	$cm^2\ min^{-1}$	[78] (averaged)
τ	1.0	min	n.a.
R	1.0	cm	n.a.

Table 6.2: Values for parameters and constants required for simulations of the initial model

6.4 INITIAL MODEL RESULTS

The first simulation presented here is based on parameter values that would typify a temperature profile present during a clinical ablation of a liver tumour that is relatively small in size (radius $\approx$ 1 cm). For this simulation the total duration was set to be 100 minutes. Approximately 30 minutes of heating was obtained by setting the centrepoints of the hyperbolic tangent functions to 20 and 50 — this produces a duration of approximately 38 minutes for a temperature rise of more than 3 °C,

with a duration of approximately 22 minutes for a temperature rise of at least 67 °C. This was deemed to be suitably representative of lengthier clinical ablation durations [14] [105].

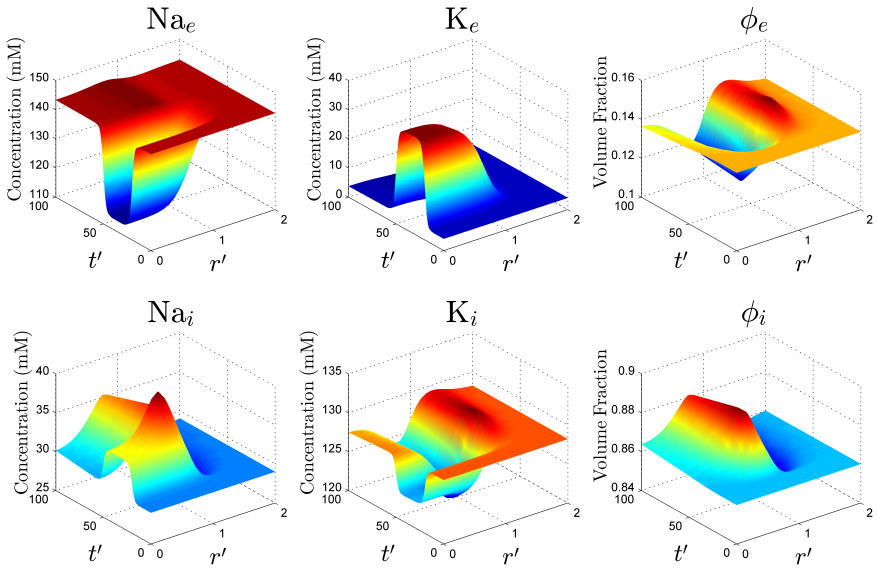

Figure 6.6: Simulation results for temperature profile shown in Figure 6.5: top panels (left to right) show Na_e, K_e, and ϕ_e; bottom panels (left to right) show Na_i, K_i, and ϕ_i.

Results from a simulation using the above temperature profile are displayed in Figure 6.6. The extracellular concentrations Na_e and K_e closely track the temperature profile (or negative of the profile for extracellular sodium), whereas the other concentrations initially track the temperature rise but then deviate. This is because the cell volume and intracellular concentrations are variables that are more closely linked together. The intracellular volume increase is relatively small, (+3.1 % of ϕ_i^0), but is more pronounced when the percentage change in the extracellular volume is considered (-19.3 % of ϕ_e^0). Despite the small nature of the volume deviations, the changes in the ion concentrations are considerably larger; in particularly K_e has a maximum increase of approximately 500 %. Such large deviations from initial ion concentrations may significantly alter the electro-chemical behaviour of the cells.

In order to investigate the significance of the shape of the temperature profile on the cell volume, two further sets of simulations were run. First, temperature functions with different maximum temperatures were used; and second, temperature functions with different values of r_s were used. To quantify the effects of these changes intracellular volume, plots of ϕ_i against r' (which controls the scale of the spatial 'stretch' of the hyperbolic tangent temperature function) are shown for the times at which the maximum increase in intracellular volume is recorded, Figure 6.7.

It is clear from Figure 6.7 that ΔT has an approximately linear effect upon changes in ϕ_i. Furthermore, with increasing ΔT the features of the graph move rightwards on the graph, i.e. towards higher r'. However, this feature is very slight relative to other effects.

Of greater interest is how r_s affects ϕ_i when all other variables are kept constant. The bottom panel of Figure 6.7 also shows that spatially 'sharper' temperature profiles (smaller values of r_s) result in greater cell swelling inside the heating zone, and greater cell shrinkage outside the heating zone — this shows a very non-linear dependence for ϕ_i upon r_s. The most obviously qualitative difference is that when $r_s = 1$, the results predict zero cell shrinkage anywhere which may be due to the extremely slow spatial 'turn off' of the hyperbolic tangent term which for $r_s > 1$ is not plateaued by $r' = 0$.

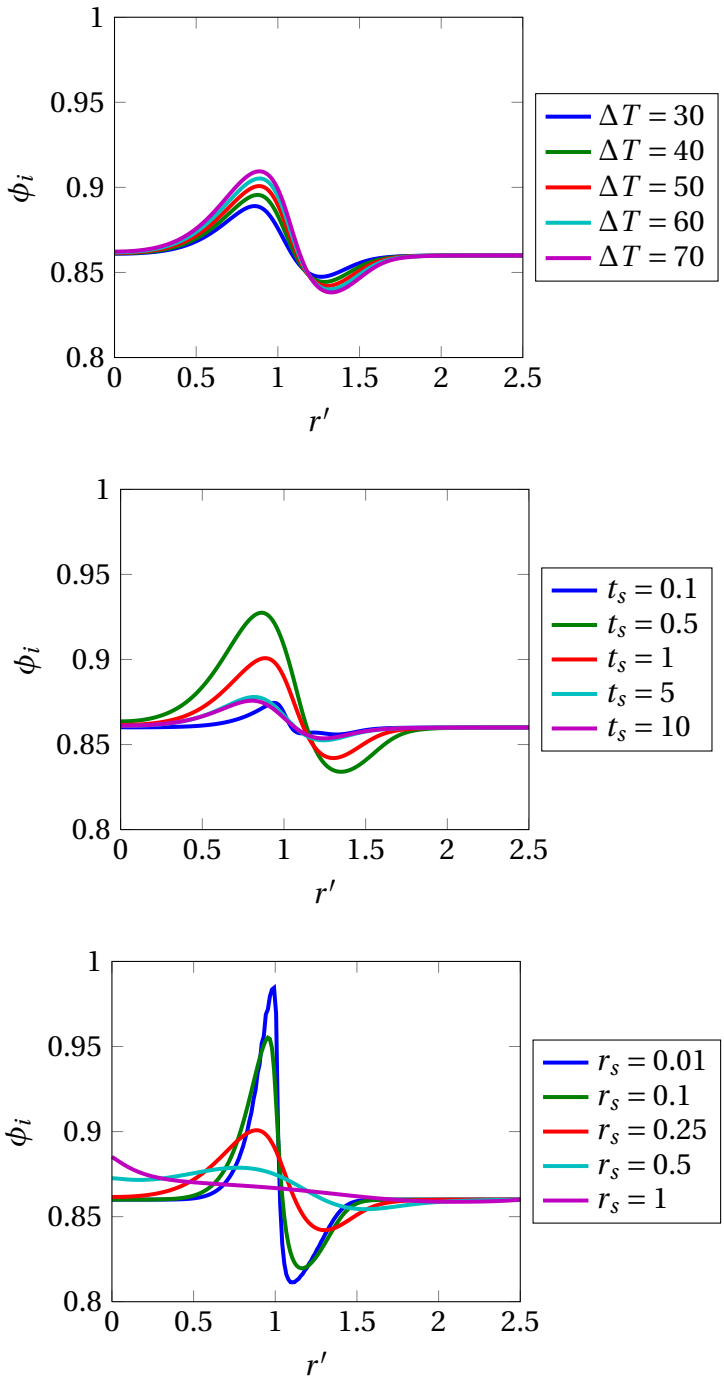

Figure 6.7: Spatial plots of intracellular volume at time of maximum swelling. Top panel shows variations with maximum temperature rise. Centre panel shows variations with temporal 'stretch' of the hyperbolic tangent in the temperature function. Bottom panel shows variations with spatial 'stretch' of the hyperbolic tangent in the temperature function. Parameters not explicitly stated are those inTable 6.2

6.5 EXTENDED MODEL

6.5.1 Cell Death Model

To further investigate the response of cell volume to imposed thermal changes, the model detailed in the first half of this chapter was extended to incorporate the model for cell death detailed in chapter 3.

Expanding the model to include cell death requires two more variables and two equations. Arbitrarily selecting the two additional variables to be the fraction of cells in the 'Alive' state and the fraction of cells in the 'Dead' state causes the additional two equations to be:

$$\frac{dA}{dt} = -k_f A + k_b (1 - A - D), \tag{6.31}$$

$$\frac{dD}{dt} = k_f (1 - A - D), \tag{6.32}$$

where k_f and k_b are the rate constants previously defined.

6.5.2 Cell Death Effects

The cell death model is here included to assess how cellular damage might affect the intracellular cell volumes. Already modelled are three transport mechanisms: passive transport of sodium through h- and m-gates, passive transport of potassium through x-gates, and active transport of both sodium and potassium through the Na-K pump. As the Na-K pump is the only method of active transport modelled, it was selected as the mechanism to be affected as cell viability was reduced through thermal damage. For simplicity, the pump current was set to linearly reduce with the decreasing fraction of cells in the Alive state. Thus, the pump conductivity was modified to:

$$k_{\mathrm{NaK}} = \overline{k_{\mathrm{NaK}}} \frac{A}{A^0}, \tag{6.33}$$

where $\overline{k_{\mathrm{NaK}}}$ is a pump scaling constant (set to the value of k_{NaK} as used in the first part of the model), whilst A^0 is the initial value of the fraction of cells in the Alive state. Thus as the fraction of cells in the Alive state reduces to zero, the Na-K pumps in cells in that region of tissue cease to function.

6.6 EXTENDED MODEL ANALYSIS

Since, the analysis detailed in section 6.3 for the initial model was also used to perform simulations with the extended model, for the sake of brevity, only changes to the analysis from section 6.3 are included here.

The extended model as detailed in section 6.5 contains four unaltered equations, two modified nonlinear equations (the modified i_{NaK} appears in two equations), and two additional differential equations. It is possible still to formulate the system into the form given in Equation 6.23. With the two new variables appended to the end of $\mathbf{u}$ the order becomes:

$$\mathbf{u} = \begin{bmatrix} \mathrm{Na}_e \\ \mathrm{K}_e \\ \mathrm{Na}_i \\ \mathrm{K}_i \\ v_m \\ \phi_i \\ A \\ D \end{bmatrix},$$

and the order of the equations used to construct $\mathbf{M}$ becomes:

1. Conservation of sodium in the extracellular volume (6.13)
2. Conservation of potassium in the extracellular volume (6.14)

Variable/Constant	Value	Unit	Source
$\overline{k_f}$	3.33×10^{-3}	s^{-1}	[92]
k_b	7.77×10^{-3}	s^{-1}	[92]
T_k	40.5	°C	[92]
A^0	0.99	n.a.	[92]
D^0	0.00	n.a.	[92]
$\overline{k_{\text{NaK}}}$	11.46	pA	[92]

Table 6.3: Values for additional parameters and constants for the extended œdema model

3. Zero osmotic pressure ($\frac{\partial}{\partial t}$ 6.9)

4. Constant extracellular electroneutrality ($\frac{\partial}{\partial t}$ 6.11)

5. Steady-state transport of sodium ions ($\frac{\partial}{\partial t}$ 6.7)

6. Steady-state transport of potassium ions ($\frac{\partial}{\partial t}$ 6.8)

7. Change in fraction of Alive cells (6.31)

8. Change in fraction of Dead. (6.32)

For the same reasons, the temporal derivatives are omitted for reasons of space; these and $\mathbf{F}_{temp}$ are given in full in section A.

The extension of the initial model with the cell death model was performed such that the parameter values given in Table 6.1 did not need to be altered. Initial conditions and boundary conditions for the original six variables were also unaffected. The two additional equations and variables in the extended model require further parameter values. Whilst these values can be found in section 3.4, for completeness, these values are listed again in Table 6.3.

6.7 EXTENDED MODEL RESULTS

The simulation results presented here for the extended model were generated using the same parameter values that generated the primary simulation in 6.4, these values being given in Table 6.1. As shown in Figure 6.8, the imposed temperature profile irreversibly results in a ablation volume where the plot of fraction of cells in the dead state (D) has a value of 1, and an undamaged region of cells where D has a value of 0.

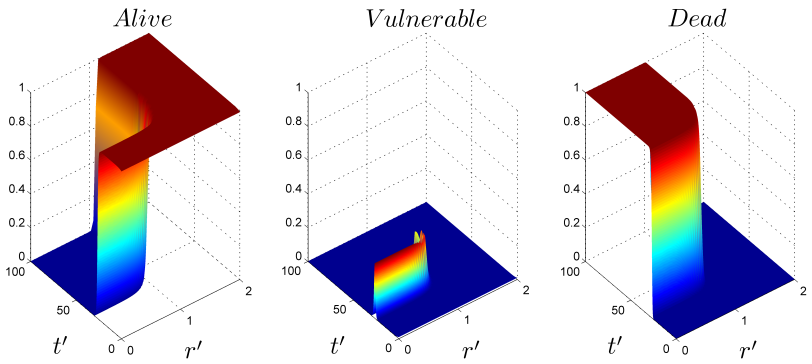

Figure 6.8: Fractions of cells in the Alive, Vulnerable, and Dead states (left, centre and right panels respectively)

Plots of the ion concentrations and volume fraction are shown in Figure 6.9 as were presented in Figure 6.6 for the model without cell death. Significantly larger amounts of cell swelling are predicted than in simulations of the model without cell death; this is shown with both greater peak values of ϕ_i and large swelling occurring over wider regions in space. Qualitatively, the plot of ϕ_i shows three main regions: an inner volume of little or no swelling from the origin to $r' \approx 0.5$, an area of cell shrinkage in the region outside the ablation ($r' > r_c$), and a region in between where there is significant cell swelling (up to $\phi_i = 1$).

Further simulations were then run to investigate the influence of ΔT, t_s, and r_s upon the intracellular volume in this extended model. Plots of ϕ_i against r' at

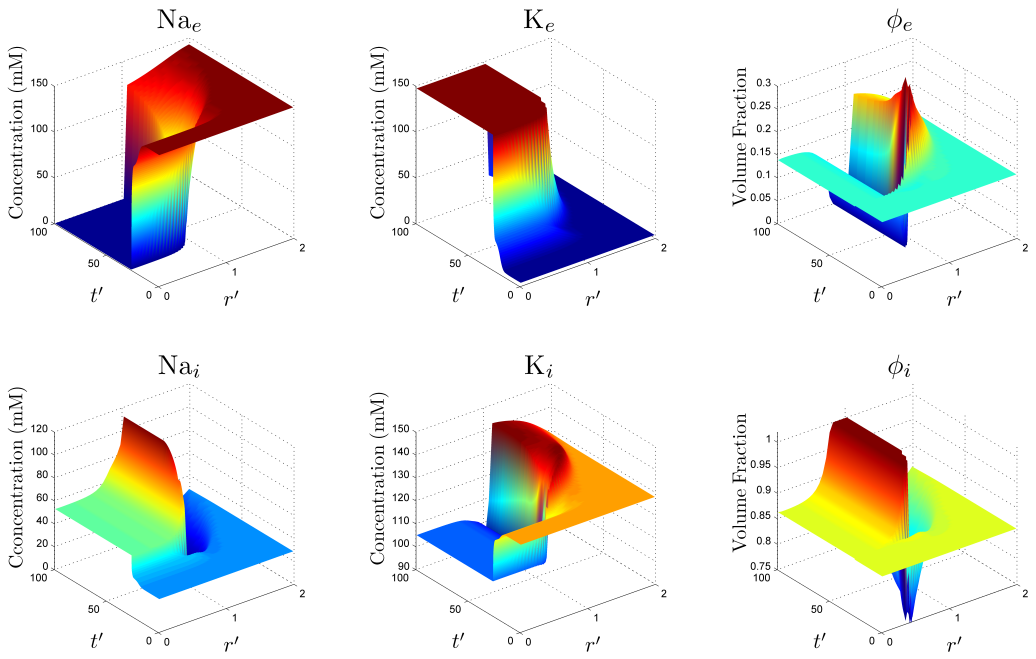

Figure 6.9: Simulation results for temperature profile shown in Figure 6.5: top panels (left to right) show Na_e, K_e, and ϕ_e; bottom panels (left to right) show Na_i, K_i, and ϕ_i.

$t = 100$ for various parameter values are shown in Figure 6.10. These results were also quantitatively assessed by determining the radial width for which $\phi_i > 95\%$, denoted here by $r_{95\%}$. Figure 6.11 shows how variations in each of ΔT, t_s, and r_s affect $r_{95\%}$.

The results presented in Figure 6.10 may serve to represent the rings of altered contrast shown in Figures 6.1 – 6.3. It was previously noted that Figure 6.1 shows lesions that have isoechoic centres, but hyperechoic rims, such as might represent core regions with little, or no, swelling surrounded by annular regions of swollen cells, or excess fluid. Similarly Figure 6.2 and Figure 6.3 show multiple distinct regions. In each case, the ring surrounding the core region is of approximately constant radial width. Compared to the radius of the core region, the radial widths of

these rings are similar to the $r_{95\%}$ widths of Figures 6.10 and 6.11 — between 10 % and 40 % of the core regions' radii.

With increasing ΔT the $r_{95\%}$ region of swelling increases at first, and then reduces, possibly because at high ΔT the cell death model progresses very rapidly to a fully dead region. It may be that maximum swelling is dependent upon a significant period of time spent with cells in the 'vulnerable' state. This hypothesis may also have support from the variation in t_s, as $r_{95\%}$ is shown to greatly increase with t_s initially but to reduce subsequently at $t_s > 2$. Notably, for $t_s = 0.1$ the maximum swelling and maximum shrinkage are both small. One possible reason might be that above a certain maximum $\frac{\partial T}{\partial t}$ cell death occurs at a rate so high that minimal extracellular diffusion of ions is possible and that the $\mathrm{Na}-\mathrm{K}$ pump is disabled almost instantly, preventing the gradually changing imbalance of concentrations that gives rise to changes in volume fraction.

The position of the region of swelling also varies with ΔT, but is broadly consistent with variations in t_s or r_s with which the radial positional where the transition from swelling to shrinkage occurs at $r' \approx 1$ for all simulations. The effect of increasing ΔT is that the 'start' of the swelling occurs at a larger value of r'; this spatial repositioning is approximately linearly dependent upon changes in ΔT. Similarly, the spatial position of the 'end' of the swelling moves to greater values of r' with increasing ΔT.

Finally, the dependence of $r_{95\%}$ upon r_s is clearly shown by Figure 6.11 to be approximately linear. Only three values for r_s were tested because using values of r_s larger than 0.1 resulted in a temperature profile with a spatially dependent hyperbolic tangent that does not plateau at $r' = 0$ and thereby $\frac{\partial T}{\partial r'} \not\approx 0$ at $r' = 0$.

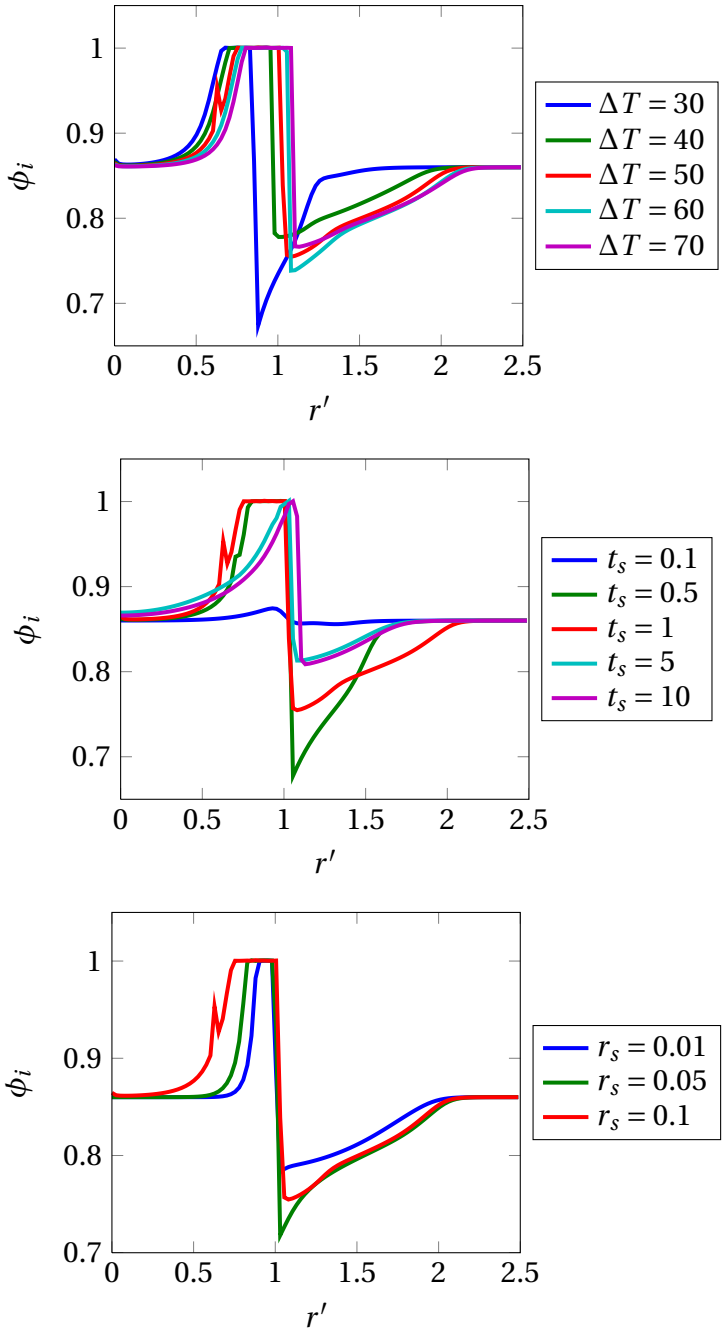

Figure 6.10: Spatial plots of intracellular volume at time of maximum swelling. Top panel shows variations with maximum temperature rise. Centre panel shows variations with temporal 'stretch' of the hyperbolic tangent in the temperature function. Bottom panel shows variations with spatial 'stretch' of the hyperbolic tangent in the temperature function. Parameters not explicitly given take values from Table 6.3.

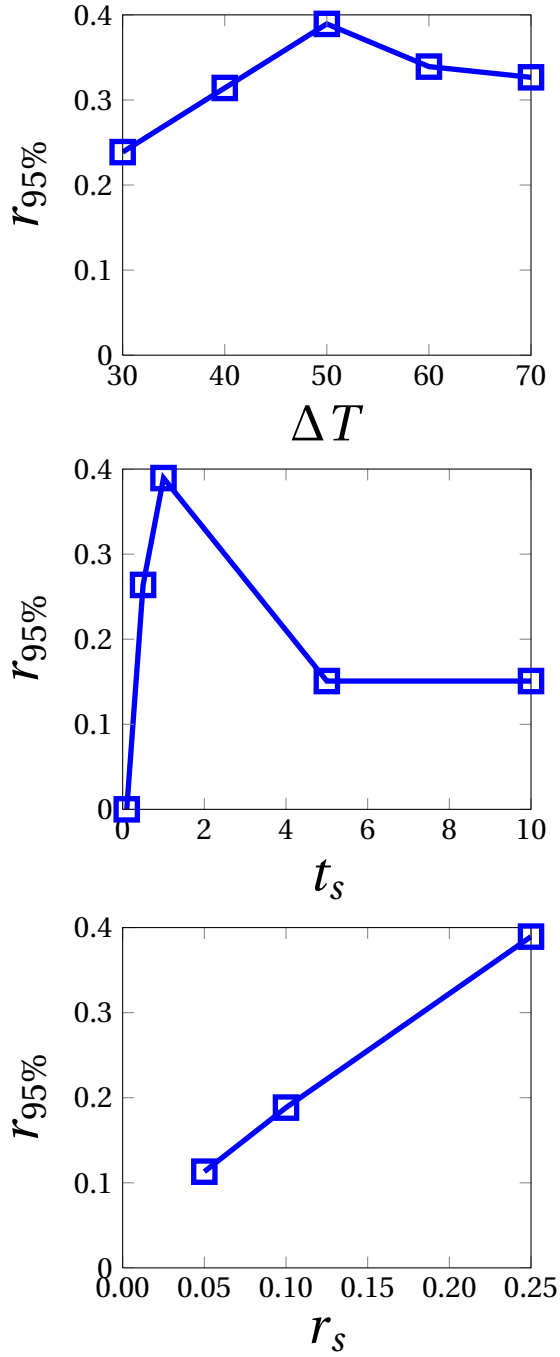

Figure 6.11: Dependence of r_{95} upon variations in parameter values. Top panel shows variations with ΔT, middle panel shows variations with t_s, bottom panel shows variations with r_s.

6.8 DISCUSSION

6.8.1 Model Refinement

In the model proposed here, there are several areas for potential further refinement. Parameters used are assumed to have no temperature dependence other than as already stated. Whilst this lack of complexity is beneficial to computational effort, the primary reason for constant parameter values is the lack of any experimental evidence to the contrary.

Consideration must be made to the parameters that have been adjusted from those reported in the literature. Only one concentration of the active species of sodium and potassium was adjusted — the intracellular concentration of potassium, K_i. The value used here was 23 % lower than that reported which is not insignificant, but was necessary in order to achieve conditions of no net charge inside the cell and for there to be no difference in water potential across the cell membrane. The other adjusted concentration was the intracellular concentration of large nonpermeable ions which was lowered by 18 %. Intracellular potassium and nonpermeable anions were selected to be modified because the deficit in equations 6.9 and 6.12 was a constant value, and thus to minimise the relative changes the largest concentrations were selected. It should be noted that extracellular electroneutrality (Equation 6.11) was true for the values reported by Melkikh and Sutormina and thus modifying an extracellular concentration would have invalidated this otherwise balanced equation.

It was necessary to adjust parameters in equations 6.3, 6.4 and 6.5 in order to satisfy equations 6.7 and 6.8; either the conductance parameters (k_{K}, k_{Na} and k_{NaK}) or the voltage parameters (v_x, v_m and v_h) required modification. The conductance parameters were selected for adjustment for two reasons: the highly nonlinear na-

ture of the equations would mean that altered potentials would severely change the dynamics of the equations. Secondly, Endresen *et al.* refer to the potentials as 'observed constants', it is assumed that these were obtained through fits to experimental data as done in a previous publication [35]. Endresen *et al.* then refer to the conductances as 'adjustable parameters' and thus these were selected for recalculation. Simulations were run to assess the differences in results when selecting k_{K} or k_{Na} to be fixed; no substantial differences in simulation output were found.

The assumption that cells remain fixed in space permits the use of Equation 6.2. Assuming that the extracellular space has a high fluid content that can be forced away as a cell swells gives justification for spatially fixed cells. However, as extracellular volume fractions approach zero, immovable extracellular structures such as sizable extracellular matrix components will become significant and the assumption of spatially fixed cells should be addressed. Further model refinement should examine these assumptions and their validities.

It should be noted that Endresen *et al.* in their earlier publication equations for ion currents that incorporate the product of entropy and temperature. However, they acknowledge the lack of any experimental data and subsequently incorporate the temperature dependence directly into the gate potential. Whilst this temperature dependence may play an important part in the model presented here, it is not currently possible to quantify the scale of the dependence without a detailed look at a wide range of experimental data. This entropy-temperature term could however prove to be a very promising route for further investigation, should data become available in the future.

Finally, it should be noted that the formulation of the model with highly nonlinear temporal effects (ion transport equations) being coupled with spatial derivative (diffusion) terms means that there is a considerable challenge in numerical imple-

mentation. In order to minimise, but not eliminate, spatial oscillations, it was found that it is desirable for the numerical step size relationship to be such that $\delta r' < \delta t'$, yet this is difficult to achieve because the nonlinear temporal temporal differential equations require use of a 'stiff' numerical solver. The 'method of lines' as implemented for these simulations is best suited to a fixed spatial discretisation and thus is somewhat inconvenient for producing simulation results with high spatial resolutions and short computation times but without oscillations. In the cases shown in Figure 6.10, numerical oscillations appear in the simulation where $\Delta T = 50$, $t_s = 1$, and $r_s = 0.1$, and in the simulation where $t_s = 0.5$; the other simulations that showed no numerical oscillations had smaller values of $r_{95\%}$. These simulations with the largest values of $r_{95\%}$ also had the steepest spatial gradient of swelling $\left(\frac{\partial \phi_i}{\partial r'}\right)$; it is likely that this is linked to the origin of the oscillations and the discontinuities between regions of swelling and shrinkage.

Further work involving simulations that investigate either further parametric studies or the simulation of real clinical therapies will necessitate a more professional computational solver a solver that is 'stiff' in both time and space might be required, the creation of which would be beyond the scope of the work presented here.

6.8.2 Additional Cell Death Effects

The cell death model incorporated into the model affects the hepatocyte model through the inoperation of the Na-K pump only. Another possible physiological result of ablation may be cell membrane rupture. Were this to happen, for example, at the origin of the heated region where maximum temperatures occur, then the modelled system would need not only $\frac{\partial T}{\partial t}$ as an input but also the inclusion of temporally variable boundary conditions. A likely form would be that of a Heavi-

side step function where ϕ_i, Na_i, and K_i become 0, whilst Na_e and K_e are modified to account for all ions suddenly existing in the extracellular volume. With these new values, electroneutrality would be maintained in both the intra- and extracellular volumes, but the osmotic pressure would not. To balance the equation of osmotic pressure, Na_i and K_i would have to be set to equal the extracellular concentrations; $\phi_i = 0$ resolving any issue of maintaining a conservation of mass.

One demonstration of such a boundary condition step function is: if cells at the origin were to rupture at normothermia, Na_e would be modified from 143.0 mM to 120.2 mM and K_e would change from 4.0 mM to 28.8 mM, both causing significant concentration gradients. In such a case the system would switch from one where diffusion is driven by changes in the cellular dynamics to one where cellular dynamics and Nernst potentials are driven by extracellular diffusion. This is clearly a considerably different modelling scenario but one that will need to be further investigated.

6.8.3 Diffusion Coefficient Importance

Possibly the most crucial relationship to the model is that of the difference between diffusion coefficients. Without a difference between D_{Na} and D_{K} there is no temperature dependent change in cell volume as shown mathematically below.

Combining equations 6.13 and 6.15, and equations 6.14 and 6.16, the diffusion equations can be written:

$$\frac{\partial}{\partial t}\left(\phi_e \mathrm{Na}_e + \phi_i \mathrm{Na}_i\right) = \nabla D_{\mathrm{Na}} \nabla \mathrm{Na}_e, \tag{6.34}$$

$$\frac{\partial}{\partial t}\left(\phi_e \mathrm{K}_e + \phi_i \mathrm{K}_i\right) = \nabla D_{\mathrm{K}} \nabla \mathrm{K}_e. \tag{6.35}$$

By combining constant parameters into single terms c_1 and c_2, Equation 6.9 and 6.11 can be re-expressed as:

$$\mathrm{Na}_e + \mathrm{K}_e = c_1, \tag{6.36}$$

and

$$\mathrm{Na}_i + \mathrm{K}_i = c_2 - \frac{\phi_i^0 \mathrm{A}_i^0}{\phi_i}. \tag{6.37}$$

Summing 6.34 and 6.35 and substituting 6.36 and 6.37 produces:

$$\frac{\partial}{\partial t}\left(\phi_e c_1 + \phi_i\left(c_2 - \frac{\phi_i^0 \mathrm{A}_i^0}{\phi_i}\right)\right) = \nabla D_{\mathrm{Na}} \nabla \mathrm{Na}_e + \nabla D_{\mathrm{K}} \nabla \mathrm{K}_e, \tag{6.38}$$

from which the $\phi_i^0 \mathrm{A}_i^0$ term is constant and thus can be removed from the differential. Then, by eliminating ϕ_i, K_e with the substitutions: $\phi_i = 1 - \phi_e$, $\mathrm{K}_e = c_1 - \mathrm{Na}_e$, 6.17 and substituting out D_{Na}, and D_{K} with equations 6.18 and 6.38, equation 6.38 becomes:

$$\frac{\partial}{\partial t}\left(\phi_e c_1 + c_2 - \phi_e c_2\right) = \frac{D_{\mathrm{Na}}^0}{\phi_e^0} \nabla \phi_e \nabla \mathrm{Na}_e - \frac{D_{\mathrm{K}}^0}{\phi_e^0} \nabla \phi_e \nabla \mathrm{Na}_e, \tag{6.39}$$

which can be further simplified to:

$$\frac{\partial}{\partial t}\left(\phi_e\right) = \frac{1}{\phi_e^0 (c_1 - c_2)}\left(D_{\mathrm{Na}}^0 - D_{\mathrm{K}}^0\right) \nabla \phi_e \nabla \mathrm{Na}_e. \tag{6.40}$$

This final expression shows clearly that in the case where D_{Na}^0 is equal to D_{K}^0 then the temporal derivative of cell volume fraction is zero and no swelling occurs.

Additionally, this proof shows that in the scenario that D_{Na} is smaller than D_{K}, the temperature dependence of ϕ_i is reversed, i.e. with the model without the inclusion of the O'Neill Model for cell death the results would be a decrease in cell volume; shrinkage instead of the swelling demonstrated. This finding suggests that close attention should be paid to the differences between diffusion coefficients of various different species if the model is expanded to include other active ions. Further, should there be any parameter that causes variations in diffusion coefficient then it would be important to investigate this dependence carefully, for if it were to

modify the difference between diffusion coefficients, then this would alter the cell volume response of the system. Such parameters might include temperature, material properties or any introduced non-naturally occurring chemicals (perhaps the presence of chemotherapeutic drugs).

6.8.4 Clinical Implications

Any significant swelling, even of cells that subsequently progress to a dead state, is important in a clinical setting. Registration of pre-, intra- and post-operative images is vital to a clinician's ability to determine treatment success. Variable swelling that alters the geometry of relevant treatment volumes between different imaging times increases the difficulty of obtaining accurate registration, thereby adding an additional unknown for clinicians to interpret.

Whilst the results presented here have primarily been focussed upon the intracellular volume swelling, it might be important to consider the change in extracellular volume. In all simulations, the region outside of the imposed temperature profile shows reduction in ϕ_i, ie an increase in extracellular volume. Clinically, a bright ring is visible in imaging data (Figures 6.1, 6.2, and 6.3). This ring is commonly thought to correspond to a hypervascular zone as it is most visible in arterial phase images. A significant increase in ϕ_e may be the cause of this bright ring as a result of an influx of fluid to the volume containing the shrunken cells.

One of the cardinal tasks for clinicians performing RFA is to be assured that the final ablation zone fully encompasses the tumour. In current clinical practice the only real-time tool for monitoring ablation development available to radiotherapists are the readings from the temperature probes that are part of the RFA needle. If the results presented here prove to be accurate, then this observable bright ring could indicate the location of the rim of the ablation. The model results presented

here might provide a valuable link between the imaged ring and the ablation zone and thus potentially result in a method of early determination of the extent of the ablated zone. Such a link would be of immense clinical use and would be almost guaranteed to raise ablation success rates.

6.9 CONCLUSION

In this chapter a novel mathematical model of a hepatocyte has been created that predicts cell swelling in response to temporally and spatially varying imposed temperature fields. The model was constructed from previously published equations and physical assumptions using published experimental data with minimal modification. The hepatocyte model was combined with the model for cell death presented in chapter 3. These models were used to simulate a continuum of similar cells in a diffuse extracellular medium. Equations governing ion transport across the cell membrane contain dependence upon both temperature and the state of the cell; the effect of this upon the whole system was investigated by simulating a continuum volume subjected to various imposed temperature conditions. Parameters used to characterise the temperature functions were selected to mimic temperatures profiles present in the liver during thermal ablations as used in the treatment of cancer tumours.

Simulation results for the initial model without cell death showed that the model responded approximately linearly to the absolute rise in temperature and strongly non-linearly to the spatial 'sharpness' of the imposed temperature function. A linear response to the magnitude of the difference between diffusion coefficients of sodium and potassium proven mathematically. No other significant dependencies were discovered.

More powerful results were discovered from simulations of the extended model which showed significant increases in the intracellular volume in a spherical annulus colocated with the rim of the ablated zone. The extent of the swelling was such that at places in the simulations the extracellular volume decreased to a volume fraction of zero. Further, a significant area of cell shrinkage (i.e. extracellular volume increase) was predicted in a region immediately peripheral to the area of cell swelling. Clinically, volumes of increased fluid (blood or other fluids) can be relatively easy to image. Such a region of cell shrinkage, and with it increased extracellular volume, may result in an influx of interstitial fluid which could potentially be used as another imaging biomarker. These results suggest that the standard behaviour of hepatocytes at such supraphysiological conditions as found in thermal treatments might contribute to oedemata as observed clinically. This may prove of use as the results show a strong spatial link between model predicted ablation zones and regions of swelling; in a clinical setting observations of œdemata might in future be utilised to provide early indications of final ablation sizes.

CHAPTER 7

CONCLUSIONS AND FURTHER WORK

The work presented in this thesis along with work completed by collaborations led to the publication of Payne, S. J., Flanagan, R. Pollari, M. , Alhonnoro, T. , Bost, C. , **O'Neill, D. P.**, Peng, T. , and Stiegler, P., "Image-based multi-scale physiological planning for ablation cancer treatment", *Philosophical Transactions of the Royal Society A*, **369:** 4233–4254, 2011.

Additionally, due to the nature of the collaborative project from which this thesis was written, some of the 'future work' has already been carried out by other researchers; these associated publications are mentioned as relevant in the text of this chapter.

7.1 CONCLUSIONS

This work that led to the this thesis contributed towards the objectives of a seven partner, collaborative consortium, IMPPACT: **I**mage-based **M**ultiscale **P**hysiological **P**lanning for **A**blazon **C**ancer **T**reatment, the objectives of which were detailed in section 1.3. Required by the research team at Oxford was the supply of mathematical models for implementation by NUMA Engineering Services, and for validation with data supplied by experimental and clinical teams at the Medical Universities of Graz and Leipzig. Two mathematical models were necessary: a heat transfer model developed by Dr. T. Peng, and a cell death model, primarily devel-

oped by the author of this thesis and presented in Chapters 3 – 5. Identified during the course of the project was the scope for the creation of a model for thermal œdema. The O'Neill Model for cell death was also used as an input for the model for thermally induced œdema. The end objectives of the project included model validation. Porcine liver test ablations and clinical case studies were used to demonstrate how the various modelling and simulation work-packages of the project assembled into a single predictive tool for modelling thermal ablation in the liver. For further details of the other components, how they fit together and demonstrations of two case study ablation simulations, see Appendix B which contains Payne *et al.* [95].

Predicting thermal ablation of tumours is not a trivial task, there being two major reasons for this; the first of which is that the ultimate prediction of ablation volume is the output of a series of successive mathematical models which causes difficulty with regards to validation of individual components. In subsection 7.1.1 the manner in which the various models fit together is detailed, after which, subsection 7.1.2 discusses the methods and challenges of validation. The second significant obstacle to modelling RFA, patient specific variability, is discussed in subsection 7.1.3.

7.1.1 Model Assembly

In order to model thermal ablation, three key models are required: a heat transfer model for predicting the spatio-temporal temperature field from the imposed heat source, a cell death model for determining the progressive cell damage that results from the developing temperature field, and a model that accounts for how various material properties vary under conditions of high temperature rises and tissue damage. These models, their inputs, and their outputs are summarised in Table 7.1.

To complicate matters further, these models form a closed loop as is schematically shown in Figure 7.1. This interconnectedness results in a highly complex sys-

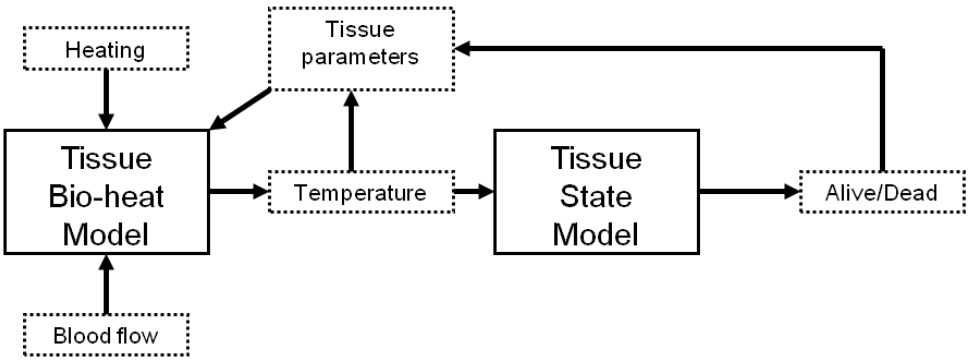

Figure 7.1: Schematic of models of ablation, reproduced from Payne *et al.* [96]

tem where each model must be considered in relation to the others. Additionally there is the consequence that this closed loop causes a number of difficulties for validation and this will be discussed subsequently.

Model	Input	Output
Heat Transfer	Applied heat source Material properties	Temperature
Cell Death	Temperature Time-temperature history Current tissue viability	Tissue Viability (alive/partially damaged/dead)
Material Properties	Temperature Tissue state	Thermal Conductivity Fluid porosity et cetera

Table 7.1: Submodels with inputs and outputs required for modelling thermal ablation

There is much literature for predicting heat transfer in biological tissue. However, the liver is an unusually highly perfused medium where, with the exception of the few major blood vessels, the vascular network is fine in nature and unpredictable both between patients and even across a single liver. Furthermore, there are clinical restrictions that arise from image resolution limits, registration issues, and needle damage which mean that many of the established models for heat transfer are inappropriate for RFA in the liver.

In work carried out primarily by the author's collaborator, Dr. Tingying Peng, during the course of the project it was shown mathematically that all blood vessels can be classified into three classes for heat transfer [100]. Large vessels (such as large arteries and veins) have such high rates of blood flow that the blood within them does not increase significantly in temperature above normothermic conditions. Thus, these vessels primarily act as heat sinks for the heated tissue through which they pass. The smallest vessels (capillaries, sinusoids, and vessels a few generations higher) have such slow flow rates that the blood flowing through them is equilibrated with the surrounding tissue and there is negligible heat transfer. The final class, terminal artery branches (before arterioles), are of the appropriate length and channel blood at certain flow rates such that the majority of temperature equilibration occurs across them; these vessels are correspondingly termed 'thermally significant'. In clinical settings, these, most significant, vessels are just beyond the imaging resolution limit currently possible. However, as imaging resolution improves in future, the ability to individually identify and model these thermally significant vessels may become possible.

Having identified limitations in the literature regarding models of cell death in chapter 2, chapters 3, 4, and 5 presented the creation and subsequent development of a model to predict the progression of thermal damage of liver cells under hyperthermic conditions. This focus resulted from the identification in chapter 2 that the literature for hyperthermic cell death was sparse with regard to supra-physiological hyperthermia and that the key model used (the Arrhenius model) was poorly suited to clinical implementation. The O'Neill Model for cell death is dynamic in time unlike many of the alternative models; it is also compatible with temporarily varying temperature fields because it can predict the instantaneous state transition rates. In

this way, the O'Neill Model fits within the schematic shown in Figure 7.1 and is fully implementable for clinical use.

The literature for models of material properties of liver tissue dependence upon temperature and/or progressive tissue damage remains relatively sparse. That which existed was somewhat inconclusive or showed little variation with temperature. As such, models for material properties were left for investigation at a later date as their influence was presumed to be of a secondary effect and therefore not easily discernible given the quality of the data available for validation.

The model for thermally induce œdema is entirely novel and does not sit within the iterative loop shown in Figure 7.1. Whilst it does require inputs that are the results from both the tissue bio-heat model and the tissue state (cell death) model, its own results (cellular volume changes) do not feed back into the global model at this point. The model in chapter 6 is presented as a preliminary model that suggests a mechanism for predicting the hyperdense annular shell observed around thermal ablations. The primary objective of creating the model was to investigate whether predictions of thermally induced volume cellular swelling were possible; this has successfully been shown and thus validation, which is discussed next, is the greatest priority for future work.

7.1.2 Validation

Validation is a vitally important process with any model that is intended for engineering implementation. As alluded to earlier, validation for thermal ablation therapies is extremely difficult. One particularly significant challenge is patient variability. The various ways in which patient specific variations affect the model are discussed later in subsection 7.1.3. In an ideal modelling scenario it would be to validate any single component of the model individually. Obtaining such conditions

for experimental validation of the component models of this thesis is a substantial challenge; to date, one without an ideal solution.

If it were possible, real-time observations for each output during a thermal ablation (clinical or experimental) would be the perfect tool for model validation. However there is a considerable limitation in the ability to obtain conclusive quantification of model outputs. Temperature fields can be monitored with excellent temporal resolution by use of temperature probes (such as are built in to the RITA Starburst needle), but the spatial sampling is poor as is the subsequent registration with imaging. Collaborators in the IMPPACT project produced and used a bespoke temperature probe rig designed to the author's specification to determine the temperature changes throughout the duration of the ablation at a greater number of spatial locations than is possible with the RITA Starburst needle's inbuilt thermometers. Imaging thermometry with magnetic resonance imaging has been used experimentally but is not possible here because the metal composition of the ablation needles is incompatible with MRI equipment. Consequently, a perfectly determined spatio-temporal temperature field is not attainable, neither for validation purposes, not as a fully-known input to the cell death and œdema models.

The final extent of cell death is a definitive experimental result, however it is only ever determinable with histological staining. Histological evidence has to occur after treatment through the extraction of the tumour (or the whole liver), slicing and labour-intensive staining and analysis. Thus, there will not be any available data for the temporal progression of cell death through the duration of the ablation. Even performed with the utmost skill and care, the procedures involved in obtaining histologies are liable to have the tissue slices become warped (or even torn). Therefore there exist substantial registration issues that result from changes in geometry in

the process of ablation extraction, some of which are addressed by collaborators in [118].

The validation of thermally induced œdema is, in theory, a more easily obtainable goal. Borne out of the observation of an imaging phenomenon and post-excision histological evidence of cellular swelling, the model was designed to be multiscale. It achieved this with explicitly modelled cellular-level processes that manifest themselves at the tissue level. It is this macroscopic result (changes in tissue density) that may be observed in intra- or post-operative imaging data. Validation is not trivial though as it requires a minimum degree of confidence in both the outputs of the bio-heat model and of the cell death model. However, the excellent temporal resolution available through ultrasound imaging, and the high quality spatial resolution of CT imaging could potentially be powerful tools for evaluating and validating the œdema model.

7.1.3 Patient Specific Considerations

In addition to the practical difficulties of obtaining meaningful data discussed above, there is a related, but distinct, complication that each liver is unique in a number of ways. The extent to which these patient specific variations affect the models in both their current form and their future development must be considered.

Heat transfer in the liver, for the most part, is a mechanical, not a biological process. However, a number of pathological conditions will modify the transfer of heat. The dependence of heat flow upon blood flow, as shown in [91], [99], [100], [101], and [98] means that this is one of the most important variations between patients to understand. Whilst the difficulties encountered with registering vessel geometries from imaging were discussed above, a number of other issues also exist. Determin-

ing blood flow rates in various vessels is a substantial challenge, not least because small errors in registered vessel diameters can vary flow rates substantially. Additionally, pathologies such as stenosed or occluded vessels elsewhere in the liver can significantly alter local blood flow rates. Cirrhosis frequently causes significant volumes of blood to be shunted directly to the venous tree (see subsection 2.2.6). The increased vasculature that is associated with tumour growth will additionally modify the local perfusion and the vessel sizes involved are likely to be below current imaging resolutions. Reduced cardiac output caused by age, anæasthesia or other factors may also modify the total blood flow to the liver and the corresponding flow in the region of interest. Further studies into these, and other, relevant pathological conditions will need to be performed to yield further model refinement and to move towards a greater patient specific adaptability.

The cell death model presented in chapter 3 was fitted to data involving HepG2 cells and lung fibroblasts. Chapter 4 then established how different cell types affect the model parameters. This is of particular relevance to making the model patient specific. There are many different primary cancers found in the liver and an extremely large variety of metastatic carcinomata (as detailed in subsection 2.2.5), each with a different, or mix of different, cell types. Whilst much of the literature shows how parameter values of various models vary for differing cell type, as discussed in section 2.4, these parameter values often vary with little or no predictability between different experimental set ups. Further, tests upon cultures of single cell types do not closely represent liver conditions where the liver parenchyma is perforated by sinusoids, capillaries, stellate cells and other structures.

On the macroscopic scale where tissue damage is considered, discretised volumes will invariably contain some mixture of cell types. The experimental work on which chapter 4 was based was initiated in consideration of this fact and mixed co-

cultures were used to provide experimental data. As mentioned in section 4.6, the disadvantages of this experimental method that results in uncertainties over exact viabilities of differing cells types in a mixed co-culture should be considered. However, one useful feature of the cell death model presented here is that parameter values varied between cell type investigated, but within one order of magnitude. This shows that when the exact cell line composition of tissue is unknown, it is hoped that the model can still be of use by producing broadly consistent predictions of tissue damage.

As discussed above and demonstrated in the relevant chapters, the heat transfer and cell death models can be implemented clinically for patient specific cases, so long as sufficient care is taken over determining geometry for the heat transfer model, and specifying cell line dependent parameters. The model for thermally induced œdema must also be used with careful consideration of how parameters may vary. Perhaps importantly, cirrhotic livers are often turgid with blood; this would mean that despite ion concentrations remaining unchanged, the additional extracellular blood and fluid may translate to a different balance between homeostatic intra- and extra-cellular volumes (ϕ_i^0 and ϕ_e^0).

Also worthy of mention here is that the model for œdema was generated with the specific purpose of providing a link between intra-operative imaging data and final ablation volume. Hence the œdema model, if completely and successfully validated to show the hyperdense annular shell in CT images is collocated with the rim of the ablation zone, could function as a completely independent method of determining final ablation. In this way it could provide a fully compatible validation method for the other models.

7.2 FURTHER WORK

The work presented in this thesis and summarised in the first part of this chapter, although satisfactorily concluded for the requirements of the IMPPACT project, has a number of lines along which further work could take place. As presented, the models of this thesis were brought to varying states of validation and it is further validation that dominates the recommendations for further work discussed below.

7.2.1 Future Validation

The O'Neill Model for hyperthermic cell death has perhaps the most clear direction forward in the immediate future. As presented in chapters 3, 4, and 5, the model has been shown to fit the experimental data within the standard errors of the data sets and some cell line dependence has been shown in the model parameters, although the previously mentioned caution must be had when using results from mixed co-cultures. Further experimental data obtained from replicating the experimental procedure with additional different cell lines will widen the applicability of the model to various clinical scenarios. Additionally, investigating alternative experimental methods, such as the transwell membrane, or cell-line specific viability assays, might yield methods that provide greater insight into survival rates of mixed co-cultures. Extrapolating outside of the IMPPACT project, with further experimental work, the O'Neill Model could be applied to the prediction of thermally induced cell death in any number of other tissues. The pancreas, kidney, and colon are prime examples of tissues in which RFA has been used and each will have a different mixture of cells and cell lines.

It was inferred from the results presented in section 4.4 that modifying the experimental procedure affects the model parameters. Further investigation into this possibility should be a priority. If the use of a transwell membrane had a direct effect

upon cell viabilities then this should be modelled, however if the highly increased sensitivity of cell cultures was a secondary effect, caused by experimenting upon part-cultures that were insufficiently massive, and as such can be ruled out, then this should be confirmed through further work. By integrating the cell death model into the global model for validation and quantifying how sensitive the final lesion size is to variations in parameter values, the relative importance of determining cell death parameter variations can be assessed easily.

The work of chapter 5 drew comparisons between the empirically based O'Neill Model and the mechanistic Jung Model. The Jung Model was modified in order to better fit the experimental data, however no observations were made experimentally to provide secondary support to these changes. The experimental data of Jung are not available and thus this method is not currently possible. Further work to obtain mechanistic experimental data of lesion creation would be of great interest and use for determining the validity of the Modified Jung Model beyond the result that it provides a better to the post-heating experimental data than the original model.

Problems that limit the ability to validate the heat transfer model in isolation were discussed in the previous sections. Further validation of the heat transfer model will take place within the process of whole-model validation. Given the limitations of obtaining ground truth for experimental results, the best process for validation will involve large numbers of simulations with subtly varied parameters that will be run for a large number of clinical case studies. Payne *et al.* [95] showed how the whole model can predict a thermal ablation to a tolerance that satisfies clinicians, but only presented a single simulation matched to one ablation.

By building a library of clinical ablations (and lab-based porcine test ablations) a wider assessment of model performance can be obtained. Cataloguing this library across various pathologies and patient specific parameters will further facil-

itate the refinement of the model and determination of parameter values. It must be noted, however, that a significant limitation upon validation is that of the imaging resolution, which under clinically acceptable limits (contrast medium dosage and X-ray dosage) is unlikely to increase significantly in the near future; porcine lab experiments are not necessary limited to the same extent. The registration issues that arise from the effects of gravity and body movement between ablation and histological excision or post-treatment scans also causes further degradation in data confidence. These limitations only serve to emphasise the importance of obtaining a larger number of ablation data sets to which the model(s) are to be validated.

7.2.2 Model Development

The heat transfer model required for the complete model of thermal ablation was developed primarily by the author's colleague. This work produced three publications, the first of which, [100], applied a two-equation coupled system with clinically representative parameter values and drew comparisons to existing models from the literature. The second publication, [101], investigated the balance between direct convective heat transfer and tissue perfusion in the locale of a blood vessel of diameter 4 mm. Most recently, work investigating intrahepatic cooling between two parallel blood vessels was presented in Peng *et al.* [98]. Further work exists for the O'Neill Model of cell death, however, as described in the previous subsection, this work is predominantly that of determining parameter values for additional cell types and validation with regard to differing experimental procedure, and gaining better insight into mixed cell co-cultures.

The model for œdema as presented in the previous chapter, contains a number of possibilities for refinement, a number of which were discussed in detail in subsection 6.8.1. Here, it is proposed how to progress with the model for œdema rather

than the details of increasing model complexity. Integrating the model for œdema into the global model schematic remains for future work and should be taken as the next step. Both the temperature field and the cell death model directly input to the model for œdema hence any developments and refinements will additionally benefit the ability to predict thermally induced cell swelling.

Finally, as identified in section 7.1, the œdema model, once fully validated, might form a direct link between images taken intra-operatively and the ultimate zone of tissue ablation. Crucially, this novel link could serve as a clinical biomarker for determining ablation zones; such a biomarker has previously been attempted with MRI thermometry and other methods, but never to great success. If successfully shown, this would be of significant use to clinicians as it would provide a real-time check for determining ablation progress in the theatre. It is therefore the final recommendation of this thesis, that establishing a link between the observed annular shells in imaging data and the final ablated zones through use of the models presented in this thesis should be the priority for future modelling of RFA.

REFERENCES

[1] A. Andreano, E. Meneghel, G. Bovo, D. Ippolito, A. Salvioni, C. Filice, S. Sironi, and MF Meloni. Contrast-enhanced ultrasound in planning thermal ablation of liver metastases: Should the hypervascular halo be included in the ablation volume? *Journal of Ultrasound*, 13(4):158–163, 2010.

[2] I. Arias, A. Wolkoff, J. Boyer, D. Shafritz, N. Fausto, H. Alter, and D. Cohen. Organizational principles of the liver. In J.W. Grisham, editor, *The Liver: Biology and Pathobiology*, chapter 1, pages 3–16. John Wiley & Sons, 5th edition, 2009.

[3] M. Ashburner. Patterns of puffing activity in the salivary gland chromosomes of drosophila. *Chromosoma*, 31(3):356–376, 1970.

[4] J.W. Baish, P.S. Ayyaswamy, and K.R. Foster. Small-scale temperature fluctuations in perfused tissue during local hyperthermia. *Journal of biomechanical engineering*, 108:246, 1986.

[5] M. Balázs, S. Várkonyi, and A. Pintér. Electron microscopic study of alcoholic liver disease with special attention to the changes of mesenchymal cells of the liver. *Experimentelle Pathologie*, 14(6):340–350, 1977.

[6] S.M. Beard, M. Holmes, C. Price, and A.W. Majeed. Hepatic resection for colorectal liver metastases: a cost-effectiveness analysis. *Annals of surgery*, 232(6):763, 2000.

[7] HD Berendes. The induction of changes in chromosomal activity in different polytene types of cell in drosophila hydei. *Developmental biology*, 11(3):371, 1965.

[8] H.D. Berendes. Polytene chromosome structure at the submicroscopic level. *Chromosoma*, 29(1):118–130, 1970.

[9] JC Bischof, J. Padanilam, W.H. Holmes, RM Ezzell, RC Lee, RG Tompkins, ML Yarmush, and M. Toner. Dynamics of cell membrane permeability changes at supraphysiological temperatures. *Biophysical journal*, 68(6):2608–2614, 1995.

[10] A. Blouin, R.P. Bolender, and E.R. Weibel. Distribution of organelles and membranes between hepatocytes and nonhepatocytes in the rat liver parenchyma. a stereological study. *The Journal of cell biology*, 72(2):441–455, 1977.

[11] P. Boyle and J. Ferlay. Cancer incidence and mortality in europe, 2004. *Annals of Oncology*, 16(3):481–488, March 2005.

[12] M.S. Breen, X. Chen, D.L. Wilson, and G.M. Saidel. Modeling cellular thermal damage from radio-frequency ablation. In *[Engineering in Medicine and Biology, 2002. 24th Annual Conference and the Annual Fall Meeting of the Biomedical Engineering Society] EMBS/BMES Conference, 2002.*

Proceedings of the Second Joint, volume 1, pages 715–vol. IEEE, 2002.

[13] J.C. Chato. Heat transfer to blood vessels. *Journal of Biomechanical Engineering*, 102, 1980.

[14] M.H. Chen, W. Yang, K. Yan, M.W. Zou, L. Solbiati, J.B. Liu, and Y. Dai. Large liver tumors: Protocol for radiofrequency ablation and its clinical application in 110 patients —mathematic model, overlapping mode, and electrode placement process. *Radiology*, 232(1):260–271, 2004.

[15] M.M. Chen and K.R. Holmes. Microvasculature contributions in tissue heat transfer. *Annals of the New York Academy of Sciences*, 335(1):137–150, 1980.

[16] X. Chen and G.M. Saidel. Mathematical modeling of thermal ablation in tissue surrounding a large vessel. *Journal of Biomechanical Engineering*, 131(1), 2009.

[17] Y.I. Cho, J.P. Hartnett, and T.F. Irvine. *Bioengineering Heat Transfer*. Advances in Heat Transfer. Academic Press, 1992.

[18] W.G. Connor, E.W. Gerner, R.C. Miller, and M.L.M. Boone. Prospects for hyperthermia in human cancer therapy. *Radiology*, 123(2):497–503, 1977.

[19] R.A. Coss, W.C. Dewey, and J.R. Bamburg. Effects of hyperthermia on dividing chinese hamster ovary cells and on microtubules in vitro. *Cancer research*, 42(3):1059, 1982.

[20] J.W. Culbertson, R.W. Wilkins, E.J. Ingelfinger, and S.E. Bradley. The effect of the upright posture upon hepatic blood flow in normotensive and hypertensive subjects. *Journal of Clinical Investigation*, 30(3):305, 1951.

[21] S.A. Curley. Radiofrequency ablation of malignant liver tumors. *Annals of surgical oncology*, 10(4):338–347, 2003.

[22] W.C. Dewey, L.E. Hopwood, S.A. Sapareto, and L.E. Gerweck. Cellular responses to combinations of hyperthermia and radiation. *Radiology*, 123(2):463–474, 1977.

[23] J.A. Dickson and S.K. Calderwood. Temperature range and selective sensitivity of tumors to hyperthermia: a critical review. *Annals of the New York Academy of Sciences*, 335(1):180–205, 1980.

[24] G.J. Dienes. A kinetic model of biological radiation response. *Radiation research*, 28(2):183–202, 1966.

[25] S. Dooley, B. Delvoux, B. Lahme, K. Mangasser-Stephan, and A.M. Gressner. Modulation of transforming growth factor β response and signaling during transdifferentiation of rat hepatic stellate cells to myofibroblasts. *Hepatology*, 31(5):1094–1106, 2000.

[26] H.A. Edmondson and P.E. Steiner. Primary carcinoma of the liver. a study of 100 cases among 48,900 necropsies. *Cancer*, 7(3):462–503, 1954.

[27] H. Elias. A re-examination of the structure of the mammalian liver. ii. the hepatic lobule and its relation to the vascular and biliary systems. *American Journal of Anatomy*, 85(3):379–456, 1949.

[28] H. Elias. Observations on the general and regional anatomy of the human liver. *The Anatomical Record*, 117(3):377–394, 1953.

[29] H. Elias. Virus-like behaviour of human carcinoma. *Nature*, 195:819–820, 1962.

[30] H. Elias. Anatomy of the liver. In C. Roullier, editor, *The Liver: Morphology, Biochemistry, Physiology*, volume 1, chapter 2. Academic Press, New York, 1963.

[31] H. Elias. Carcinoma of the liver in man. In C. Roullier, editor, *The Liver: Morphology, Biochemistry, Physiology*, volume 2, chapter 24. Academic Press, New York, 1963.

[32] H. Elias and D. Petty. Gross anatomy of the blood vessels and ducts within the human liver. *American Journal of Anatomy*, 90(1):59–111, 1952.

[33] inc Encyclopaedia Britannica. *The New Encyclopaedia Britannica*, volume 24. Encyclopaedia Britannica, 1997.

[34] L.P. Endresen, K. Hall, J.S. Høye, and J. Myrheim. A theory for the membrane potential of living cells. *European Biophysics Journal*, 29(2):90–103, 2000.

[35] L.P. Endresen and J.S. Hoye. A solution to the gating paradox. *Arxiv preprint physics/9809023*, 1998.

[36] A. Evringham, E.M. Brenneman, and S.M. Horvath. Influence of sodium pentobarbital on splanchnic blood flow and related functions. *American Journal of Physiology–Legacy Content*, 197(3):624–626, 1959.

[37] L.F. Fajardo L-G. Pathological effects of hyperthermia in normal tissues. *Cancer Research*, 44(10 Supplement):4826s–4835s, 1984.

[38] J. Ferlay, H.R. Shin, F. Bray, D. Forman, C. Mathers, and D.M. Parkin. Estimates of worldwide burden of cancer in 2008: Globocan 2008. *International Journal of Cancer*, 127(12):2893–2917, 2010.

[39] A Fischer. Dynamics of the circulation in the liver. In C. Roullier, editor, *The Liver: Morphology, Biochemistry, Physiology*, volume 1, chapter 7. Academic Press, New York, 1963.

[40] J.F. Fowler. Differences in survival curve shapes for formal multi-target and multi-hit models. *Phys. Med. Biol.*, 9(2):177–188, 1964.

[41] A.V.C. França, J. Elias Jr, B.L.G. Lima, A.L.C. Martinelli, and F.J. Carrilho. Diagnosis, staging and treatment of hepatocellular carcinoma. *Brazilian journal of medical and biological research*, 37(11):1689–1705, 2004.

[42] A. Frenzer, W.J. Butler, I.D. Norton, J.S. Wilson, I.V. Apte, R.C. Pirola, P. Ryan, and I.C. Roberts-Thomson. Polymorphism in alcohol-metabolizing enzymes, glutathione s-transferases and apolipoprotein e and susceptibility to alcohol-induced cirrhosis and chronic pancreatitis. *Journal of Gastroenterology and Hepatology*, 17(2):177–182, 2002.

[43] E.W. Gerner. *Hyperthermia in Cancer Therapy*. GK Hall Mecial Publishers, Boston, 1983.

[44] N.L. Gershfeld and M. Murayama. Thermal instability of red blood cell membrane bilayers: temperature dependence of hemolysis. *Journal of Membrane Biology*, 101(1):67–72, 1988.

[45] J-P. Gillet, M.M. Gottesman, and M. Okabe. The hepatocyte and the cancer cell: Dr jekyll and mr hyde. In I. Arias, A. Wolkoff, J. Boyer, D. Shafritz, N. Fausto, H. Alter, and D. Cohen, editors, *The Liver: Biology and Pathobiology*, chapter 66, pages 1075–1090. John Wiley & Sons, 5th edition, 2009.

[46] JP Gilmore. Effect of anesthesia and hepatic sampling site upon hepatic blood flow. *American Journal of Physiology–Legacy Content*, 195(2):465–468, 1958.

[47] S.N. Goldberg, M.C. Stein, G.S. Gazelle, R.G. Sheiman, J.B. Kruskal, and M.E. Clouse. Percutaneous radiofrequency tissue ablation: Optimization of pulsed-radiofrequency technique to increase coagulation necrosis. *Journal of Vascular and Interventional Radiology*, 10(7):907–916, 1999.

[48] C.A. Goresky. A linear method for determining liver sinusoidal and extravascular

volumes. *American Journal of Physiology–Legacy Content*, 204(4):626–640, 1963.

[49] H. Gray, P.L. Williams, and L.H. Bannister. *Gray's Anatomy: The Anatomical Basis of Medicine and Surgery*. Gray's Anatomy: The Anatomical Basis of Clinical Practice. Churchill Livingstone, 1995.

[50] A.C. Guyton and J.E. Hall. *Introduction to Physiology: The Cell and General Physiology*, pages 40+. Elsevier, eleventh edition, 2006.

[51] D.V. Habif, H.T. Randall, and H.S. Soroff. The management of cirrhosis of the liver and ascites with particular reference to the portacaval shunt operation. *Surgery*, 34(3):580–606, 1953.

[52] F.C. Henriques Jr and A.R. Moritz. Studies of thermal injury: I. the conduction of heat to and through skin and the temperatures attained therein. a theoretical and an experimental investigation. *The American Journal of Pathology*, 23(4):530, 1947.

[53] P. Hildebrand, T. Leibecke, M. Kleemann, L. Mirow, M. Birth, H.P. Bruch, and C.Brk. Influence of operator experience in radiofrequency ablation of malignant liver tumours on treatment outcome. *European Journal of Surgical Oncology (EJSO)*, 32(4):430–434, 2006.

[54] A. Jemal, F. Bray, M.M. Center, J. Ferlay, E. Ward, and D. Forman. Global cancer statistics. *CA: a cancer journal for clinicians*, 61(2):69–90, 2011.

[55] L.M. Jiji, S. Weinbaum, and D.E. Lemons. Theory and experiment for the effect of vascular microstructure on surface tissue heat transfer. part ii: Model formulation and solution. *Journal of biomechanical engineering*, 106:331, 1984.

[56] C. Jolly and R.I. Morimoto. Role of the heat shock response and molecular chaperones in oncogenesis and cell death. *Journal of the National Cancer Institute*, 92(19):1564–1572, 2000.

[57] H. Jung. A generalized concept for cell killing by heat. *Radiation research*, 106(1):56–72, 1986.

[58] W.M. Kays, M.E. Crawford, and B. Weigand. *Convective heat and mass transfer*. McGraw-Hill series in mechanical engineering. McGraw-Hill Higher Education, 2005.

[59] J.P. Keener and J. Sneyd. *Mathematical Physiology: Cellular Physiology*. Interdisciplinary Applied Mathematics. Springer, 2009.

[60] K.H. Keller and L. Seiler. An analysis of peripheral heat transfer in man. *Journal of Applied Physiology*, 30(5):779–786, 1971.

[61] Y. Kim, H. Rhim, H.K. Lim, D. Choi, M.W. Lee, and M.J. Park. Coagulation necrosis induced by radiofrequency ablation in the liver: Histopathologic and radiologic review of usual to extremely rare changes. *Radiographics*, 31(2):377–390, 2011.

[62] HG Klinger. Heat transfer in perfused biological tissueŮi: General theory. *Bulletin of mathematical biology*, 36:403–415, 1974.

[63] Z. Kmieć. *Cooperation of Liver Cells in Health and Disease*. Advances in anatomy, embryology, and cell biology. Springer, 2001.

[64] T. Knittel, D. Kobold, F. Piscaglia, B. Saile, K. Neubauer, M. Mehde, R. Timpl, and G. Ramadori. Localization of liver myofibroblasts and hepatic stellate cells in normal and diseased rat livers: distinct roles of (myo-) fibroblast subpopulations

in hepatic tissue repair. *Histochemistry and cell biology*, 112(5):387–401, 1999.

[65] H.A. Kolb and G. Adam. Regulation of ion permeabilities of isolated rat liver cells by external calcium concentration and temperature. *Journal of Membrane Biology*, 26(1):121–151, 1976.

[66] J. Landry and N. Marceau. Rate-limiting events in hyperthermic cell killing. *Radiation research*, 75(3):573–585, 1978.

[67] B.P. Lane. Functional analysis of the liver. In F.F. Becker, editor, *The Liver: Normal and Abnormal Functions*, chapter 1. Marcel Dekker, New York, 1974.

[68] D. Lanneau, M. Brunet, E. Frisan, E. Solary, M. Fontenay, and C. Garrido. Heat shock proteins: essential proteins for apoptosis regulation. *Journal of cellular and molecular medicine*, 12(3):743–761, 2008.

[69] W.W. Lautt and C.V. Greenway. Conceptual review of the hepatic vascular bed. *Hepatology*, 7(5):952–963, 1987.

[70] R.C. Lee and R.D. Astumian. The physicochemical basis for thermal and nonthermal 'burn' injuries. *Burns*, 22(7):509–519, 1996.

[71] HJ Leenders and HD Berendes. The effect of changes in the respiratory metabolism upon genome activity in drosophila. *Chromosoma*, 37(4):433–444, 1972.

[72] D.M. Leifer, W.D. Middleton, S.A. Teefey, C.O. Menias, and J.R. Leahy. Follow-up of patients at low risk for hepatic malignancy with a characteristic hemangioma at us1. *Radiology*, 214(1):167–172, 2000.

[73] W. Leyko and G. Bartosz. Membrane effects of ionizing radiation and hyperthermia. *International Journal of Radiation Biology*, 49(5):743–770, 1985.

[74] Z. Li and P. Srivastava. Heat-shock proteins. *Current Protocols in Immunology*, pages A–1T, 2004.

[75] G.G. Matthews. *Cellular Physiology of Nerve and Muscle*. Blackwell Science, 2003.

[76] R.S. McCuskey. Morphological mechanisms for regulating blood flow through hepatic sinusoids. *Liver*, 20(1):3–7, 2000.

[77] J.P. McGahan and G.D. Dodd. Radiofrequency ablation of the liver. *American Journal of Roentgenology*, 176(1):3–16, 2001.

[78] H. McLennan. The diffusion of potassium, sodium, sucrose and inulin in the extracellular spaces of mammalian tissues. *Biochimica et biophysica acta*, 24:1–8, 1957.

[79] A.V. Melkikh and D.S. Bessarab. Model of active transport of ions through diatom cell biomembrane. *Bulletin of mathematical biology*, 72(7):1912–1924, 2010.

[80] A.V. Melkikh and M.I. Sutormina. Model of active transport of ions in cardiac cell. *Journal of theoretical biology*, 252(2):247–254, 2008.

[81] A.V. Melkikh and M.I. Sutormina. A model of active transport of ions in hepatocytes. *Biophysics*, 55(1):67–70, 2010.

[82] J.W. Mitchell and G.E. Myers. An analytical model of the counter-current heat exchange phenomena. *Biophysical Journal*, 8(8):897–911, 1968.

[83] A.R. Moritz. Studies of thermal injury: Iii. the pathology and pathogenesis of cutaneous burns. an experimental study. *The American Journal of Pathology*, 23(6):915, 1947.

[84] A.R. Moritz and F.C. Henriques Jr. Studies of thermal injury: Ii. the relative importance of time and surface temperature in the causation of cutaneous burns. *The American journal of pathology*, 23(5):695, 1947.

[85] H. Moriwaki, WS Blaner, R. Piantedosi, and DS Goodman. Effects of dietary retinoid and triglyceride on the lipid composition of rat liver stellate cells and stellate cell lipid droplets. *Journal of lipid research*, 29(11):1523–1534, 1988.

[86] N.E. Nagy, K.B. Holven, N. Roos, H. Senoo, N. Kojima, K.R. Norum, and R. Blomhoff. Storage of vitamin a in extrahepatic stellate cells in normal rats. *Journal of lipid research*, 38(4):645–658, 1997.

[87] T. Nakamura, S. Nakamura, and K. Tokita. Measurement of the intrahepatic shunted flow of blood in cirrhosis of the liver. *Nature*, 1960.

[88] K. Nakata, GF Leong, and RW Brauer. Direct measurement of blood pressures in minute vessels of the liver. *American Journal of Physiology–Legacy Content*, 199(6):1181–1188, 1960.

[89] W.H. Nernst. Die elektromotorische wirksamkeit der ionen. *Z. Phys. Chem.*, 4:129–181, 1889.

[90] Y. Ni, S. Mulier, Y. Miao, L. Michel, and G. Marchal. A review of the general aspects of radiofrequency ablation. *Abdominal imaging*, 30(4):381–400, 2005.

[91] D.P. O'Neill, T. Peng, and S.J. Payne. A two-equation coupled system model for determination of liver tissue temperature during radio frequency ablation. In *Proceedings of 31st IEEE EMBS conference*, pages 3893–3896. IEEE, 2009.

[92] D.P. O'Neill, T. Peng, P. Stiegler, U. Mayrhauser, S. Koestenbauer, K. Tscheliessnigg, and S.J. Payne. A three-state mathematical model of hyperthermic cell death. *Annals of biomedical engineering*, 39(1):570–579, 2011.

[93] M. Park, H. Rhim, Y. Kim, D. Choi, H.K. Lim, and W.J. Lee. Spectrum of ct findings after radiofrequency ablation of hepatic tumors1. *Radiographics*, 28(2):379–390, 2008.

[94] D.A. Parsell, J. Taulien, S. Lindquist, P. Viitanen, R. Jaenicke, A. Horwich, F.U. Hartl, RJ Ellis, WJ Welch, D.A. Parsell, et al. The role of heat-shock proteins in thermotolerance [and discussion]. *Philosophical Transactions of the Royal Society of London. Series B: Biological Sciences*, 339(1289):279–286, 1993.

[95] S. Payne, R. Flanagan, M. Pollari, T. Alhonnoro, C. Bost, D. O'Neill, T. Peng, and P. Stiegler. Image-based multi-scale modelling and validation of radio-frequency ablation in liver tumours. *Philosophical Transactions of the Royal Society A: Mathematical, Physical and Engineering Sciences*, 369(1954):4233–4254, 2011.

[96] S.J. Payne, T. Peng, and D.P. O'Neill. Mathematical modeling of thermal ablation. *Critical reviews in biomedical engineering*, 38(1):21, 2010.

[97] J.A. Pearce. Models for thermal damage in tissues: processes and applications. *Critical reviews in biomedical engineering*, 38(1):1, 2010.

[98] T. Peng, D. O'Neill, and S. Payne. Mathematical study of the effects of different intrahepatic cooling on thermal ablation zones. In *Proceedings of 33rd IEEE EMBS conference*, pages 6866–6869. IEEE, 2011.

[99] T. Peng, D.P. O'Neill, and S.J. Payne. 1-d steady state analysis of a two-equation

coupled system for determination of tissue temperature in liver during radio frequency ablation. In *Proceedings of 31st IEEE EMBS conference*, pages 3385–3388. IEEE, 2009.

[100] T. Peng, D.P. O'Neill, and S.J. Payne. A two-equation coupled system for determination of liver tissue temperature during thermal ablation. *International Journal of Heat and Mass Transfer*, 54.9:2100–2109, 2011.

[101] T. Peng, D.P. O'Neill, S.J. Payne, C. Bost, and R. Flanagan. Mathematical modeling of directional effects of perfusion on liver tissue temperature of radio frequency ablation. In *Proceedings of 6th World Congress on Biomechanics*, pages 740–743. Springer, 2010.

[102] H.H. Pennes. Analysis of tissue and arterial blood temperatures in the resting human forearm. *Journal of Applied Physiology*, 1(2):93–122, 1948.

[103] J.A. Pickrell. *Lung connective tissue–location, metabolism, and response to injury*. CRC Press, 1981.

[104] T.D. Pollard, W.C. Earnshaw, and J. Lippincott-Schwartz. *Cell biology*. Saunders W.B. Saunders/Elsevier, 2008.

[105] R.T. Poon, K.K. Ng, C.M. Lam, V. Ai, J. Yuen, S.T. Fan, and J. Wong. Learning curve for radiofrequency ablation of liver tumors: prospective analysis of initial 100 patients in a tertiary institution. *Annals of surgery*, 239(4):441, 2004.

[106] A.M. Rappaport. Acinar units and the pathophysiology of the liver. In C. Roullier, editor, *The Liver: Morphology, Biochemistry, Physiology*, volume 1, chapter 6. Academic Press, New York, 1963.

[107] A.M. Rappaport, Z.J. Borowy, W.M. Lougheed, and W.N. Lotto. Subdivision of hexagonal liver lobules into a structural and functional unit. role in hepatic physiology and pathology. *The Anatomical Record*, 119(1):11–33, 1954.

[108] F. Ritossa. A new puffing pattern induced by temperature shock and dnp in drosophila. *Cellular and Molecular Life Sciences*, 18(12):571–573, 1962.

[109] FM Ritossa. Experimental activation of specific loci in polytene chromosomes of drosophila. *Experimental cell research*, 35:601, 1964.

[110] J.L.R. Roti and K.J. Henle. Comparison of two mathematical models for describing heat-induced cell killing. *Radiation Research*, 81(3):374–383, 1980.

[111] M.N. Rylander, K.R. Diller, S. Wang, and S.J. Aggarwal. Correlation of hsp70 expression and cell viability following thermal stimulation of bovine aortic endothelial cells. *Journal of biomechanical engineering*, 127:751, 2005.

[112] S.A. Sapareto and W.C. Dewey. Thermal dose determination in cancer therapy. *International Journal of Radiation Oncology Biology Physics*, 10(6):787–800, 1984.

[113] S.A. Sapareto, L.E. Hopwood, W.C. Dewey, M.R. Raju, and J.W. Gray. Effects of hyperthermia on survival and progression of chinese hamster ovary cells. *Cancer Research*, 38(2):393–400, 1978.

[114] S.A. Sapareto, G.P. Raaphorst, and W.C. Dewey. Cell killing and the sequencing of hyperthermia and radiation. *International Journal of Radiation Oncology*, 5(3):343–347, 1979.

[115] A.M. Sapozhnikov, E.D. Ponomarev, T.N. Tarasenko, and W.G. Telford. Spontaneous apoptosis and expression of cell surface

heat-shock proteins in cultured el-4 lymphoma cells. *Cell proliferation*, 32(6):363–378, 1999.

[116] T. Scheibel and J. Buchner. The hsp90 complexŮa super-chaperone machine as a novel drug target. *Biochemical pharmacology*, 56(6):675–682, 1998.

[117] W.E. Schiesser and G.W. Griffiths. *A Compendium of Partial Differential Equation Models: Method of Lines Analysis With Matlab*. Cambridge University Press, 2009.

[118] M. Seise, T. Alhonnoro, and M. Kolesnik. Interactive registration of 2D histology and 3D CT data for assessment of radiofrequency ablation treatment. *Journal of Pathology Informatics*, 2(2):9, 2011.

[119] C. Selden, M. Khalil, and H.J.F. Hodgson. What keeps hepatocytes on the straight and narrow? maintaining differentiated function in the liver. *Gut*, 44(4):443–446, 1999.

[120] D. Shackman, L.G. Graber, and B.G. Melrose. Liver blood flow and general anesthesia. *Clinical Science*, 12:307, 1953.

[121] S. Sherlock and J. Dooley. *Diseases of the Liver and Biliary System*. Blackwell Scientific Publications, 9th edition, 1993.

[122] S. Sherlock and J. Dooley. *Diseases of the Liver and Biliary System*. Blackwell Science Publications, 11th edition, 2002.

[123] A. Szasz and G. Vincze. Dose concept of oncological hyperthermia: Heat-equation considering the cell destruction. *Journal of Cancer Research and Therapeutics*, 2(4):171, 2006.

[124] F. Sztark, J. Dubroca, P. Latry, A. Quinton, C. Balabaud, and P. Bioulac-Sage. Perisinusoidal cells in patients with normal liver histology: A morphometric study. *Journal of Hepatology*, 2(3):358–369, 1986.

[125] N. Uchida, H. Kato, and T. Ishida. A model for cell killing by continuous heating. *Medical Hypotheses*, 41(6):548–553, 1993.

[126] T. Uehara, M. Hirooka, Y. Kisaka, M. Abe, Y. Hiasa, and M. Onji. Usefulness of the hyperechoic rim for assessing the therapeutic efficacy of radiofrequency ablation in hepatocellular carcinoma patients. *Hepatology Research*, 39(10):954–962, 2009.

[127] F.M. Vogt, G. Antoch, P. Veit, L.S. Freudenberg, N. Blechschmid, O. Diersch, A. Bockisch, J. Barkhausen, and H. Kuehl. Morphologic and functional changes in nontumorous liver tissue after radiofrequency ablation in an in vivo model: comparison of 18f-fdg pet/ct, mri, ultrasound, and ct. *Journal of Nuclear Medicine*, 48(11):1836–1844, 2007.

[128] Angiodynamics website. StarBurst Talon RFA device technical documentation. `http://www.angiodynamics.com/uploads/pdf/090210-073141_StarBurst%20Talon%20IFU.pdf`, April 2012.

[129] ATCC website. Hep g2 technical documentation. `http://www.atcc.org/attachments/17391.pdf`, December 2012.

[130] ATCC website. Mrc-5 technical documentation. `http://www.atcc.org/attachments/17396.pdf`, December 2012.

[131] IMPPACT website. `http://www.imppact.eu/`, March 2012.

[132] Sigma-Aldrich website. Corning transwell polycarbonate membrane inserts. `http://www.sigmaaldrich.com/labware/labware-products.html?TablePage=17216290`, April 2012.

[133] E.R. Weibel, W. Stäubli, H.R. Gnägi, and F.A. Hess. Correlated morphometric and

biochemical studies on the liver cell. *The Journal of cell biology*, 42(1):68–91, 1969.

[134] S. Weinbaum and L.M. Jiji. A new simplified bioheat equation for the effect of blood flow on local average tissue temperature. *Journal of biomechanical engineering*, 107:131, 1985.

[135] S. Weinbaum, L.M. Jiji, and D.E. Lemons. Theory and experiment for the effect of vascular microstructure on surface tissue heat transfer. part i: Anatomical foundation and model conceptualization. *Journal of biomechanical engineering*, 106:321, 1984.

[136] J.B. West. *Respiratory physiology–the essentials*. Lippincott Williams & Wilkins, 2000.

[137] A. Westra and W.C. Dewey. Variation in sensitivity to heat shock during the cell-cycle of chinese hamster cells in vitro. *International Journal of Radiation Biology*, 19(5):467–477, 1971.

[138] P. Whiting, J. Dowden, and P. Kapadia. A mathematical analysis of the results of experiments on rats' livers by local laser hyperthermia. *Lasers in Medical Science*, 4(1):55–64, 1989.

[139] E.H. Wissler. Comparison of computed results obtained from two mathematical models: a simple 14-node model and a complex 250-node model. *Journal de physiologie*, 63(3):455, 1971.

[140] W. Wulff. The energy conservation equation for living tissue. *Biomedical Engineering, IEEE Transactions on*, BME-21(6):494–495, nov. 1974.

APPENDIX A

EXPLICIT ELEMENTS FOR USE IN SECTION 6.3 AND SECTION 6.6

MASS MATRIX ELEMENTS IN SECTION 6.3

$$\mathbf{M}_{1,1} = \phi_e \tag{A.1}$$

$$\mathbf{M}_{1,3} = \phi_i \tag{A.2}$$

$$\mathbf{M}_{1,5} = \mathrm{Na}_i - \mathrm{Na}_e \tag{A.3}$$

$$\mathbf{M}_{2,2} = \phi_e \tag{A.4}$$

$$\mathbf{M}_{2,4} = \phi_i \tag{A.5}$$

$$\mathbf{M}_{2,5} = \mathrm{K}_i - \mathrm{K}_e \tag{A.6}$$

$$\mathbf{M}_{3,1} = 1 \tag{A.7}$$

$$\mathbf{M}_{3,2} = 1 \tag{A.8}$$

$$\mathbf{M}_{3,3} = -1 \tag{A.9}$$

$$\mathbf{M}_{3,4} = -1 \tag{A.10}$$

$$\mathbf{M}_{3,5} = \frac{\mathrm{A}_i^0 \phi_i^0}{{\phi_i}^2} \tag{A.11}$$

$$\mathbf{M}_{4,1} = 1 \tag{A.12}$$

$$\mathbf{M}_{4,2} = 1 \tag{A.13}$$

$$\begin{aligned}\mathbf{M}_{5,1} = {} & \frac{9k_{\mathrm{NaK}}}{2\mathrm{Na}_e}\mathrm{sech}^2\left(\frac{e}{2kT}\left(v + 2v_{\mathrm{K}} - 3v_{\mathrm{Na}} - v_{\mathrm{ATP}}\right)\right) \\ & + \frac{k_{\mathrm{Na}}}{8\mathrm{Na}_e}\cosh\left(\frac{e}{2kT}\left(v - v_{\mathrm{Na}}\right)\right)\left(1 - \tanh\left(\frac{2e}{kT}(v - v_h)\right)\right) \\ & \times \left(1 + \tanh\left(\frac{2e}{kT}(v - v_m)\right)\right)\end{aligned} \tag{A.14}$$

$$\mathbf{M}_{5,2} = \frac{-3k_{\mathrm{NaK}}}{\mathrm{K}_e}\mathrm{sech}^2\left(\frac{e}{2kT}\left(v + 2v_{\mathrm{K}} - 3v_{\mathrm{Na}} - v_{\mathrm{ATP}}\right)\right) \tag{A.15}$$

$$\begin{aligned}\mathbf{M}_{5,3} = {} & \frac{-9k_{\mathrm{NaK}}}{2\mathrm{Na}_i}\mathrm{sech}^2\left(\frac{e}{2kT}\left(v + 2v_{\mathrm{K}} - 3v_{\mathrm{Na}} - v_{\mathrm{ATP}}\right)\right) \\ & - \frac{k_{\mathrm{Na}}}{8\mathrm{Na}_i}\cosh\left(\frac{e}{2kT}\left(v - v_{\mathrm{Na}}\right)\right)\left(1 - \tanh\left(\frac{2e}{kT}(v - v_h)\right)\right) \\ & \times \left(1 + \tanh\left(\frac{2e}{kT}(v - v_m)\right)\right)\end{aligned} \tag{A.16}$$

$$\mathbf{M}_{5,4} = \frac{3k_{\mathrm{NaK}}}{\mathrm{K}_i}\mathrm{sech}^2\left(\frac{e}{2kT}\left(v + 2v_{\mathrm{K}} - 3v_{\mathrm{Na}} - v_{\mathrm{ATP}}\right)\right) \tag{A.17}$$

$$\begin{aligned}\mathbf{M}_{5,5} = {} & \frac{ek_{\mathrm{Na}}}{2kT}\sinh\left(\frac{e}{2kT}\left(v - v_{\mathrm{Na}}\right)\right)\left(1 + \tanh\left(\frac{2e}{kT}(v - v_m)\right)\right) \\ & \times \mathrm{sech}^2\left(\frac{2e}{kT}(v - v_h)\right) \\ & - \frac{ek_{\mathrm{Na}}}{2kT}\sinh\left(\frac{e}{2kT}\left(v - v_{\mathrm{Na}}\right)\right)\left(1 - \tanh\left(\frac{2e}{kT}(v - v_h)\right)\right) \\ & \times \mathrm{sech}^2\left(\frac{2e}{kT}(v - v_m)\right) \\ & - \frac{ek_{\mathrm{Na}}}{8kT}\cosh\left(\frac{e}{2kT}\left(v - v_{\mathrm{Na}}\right)\right)\left(1 - \tanh\left(\frac{2e}{kT}(v - v_h)\right)\right) \\ & \times \left(1 + \tanh\left(\frac{2e}{kT}(v - v_m)\right)\right) \\ & - \frac{3ek_{\mathrm{NaK}}}{2kT}\mathrm{sech}^2\left(\frac{e}{2kT}\left(v + 2v_{\mathrm{K}} - 3v_{\mathrm{Na}} - v_{\mathrm{ATP}}\right)\right)\end{aligned} \tag{A.18}$$

$$\mathbf{M}_{6,1} = \frac{-3k_{\mathrm{NaK}}}{\mathrm{Na}_e}\operatorname{sech}^2\left(\frac{e}{2kT}(v+2v_{\mathrm{K}}-3v_{\mathrm{Na}}-v_{\mathrm{ATP}})\right) \tag{A.19}$$

$$\begin{aligned}\mathbf{M}_{6,2} = \frac{2k_{\mathrm{NaK}}}{\mathrm{K}_e}&\operatorname{sech}^2\left(\frac{e}{2kT}(v+2v_{\mathrm{K}}-3v_{\mathrm{Na}}-v_{\mathrm{ATP}})\right)\\ &+\frac{k_{\mathrm{K}}}{4\mathrm{K}_e}\cosh\left(\frac{e}{2kT}(v-v_{\mathrm{K}})\right)\left(1+\tanh\left(\frac{2e}{kT}(v-v_x)\right)\right)\end{aligned} \tag{A.20}$$

$$\mathbf{M}_{6,3} = \frac{3k_{\mathrm{NaK}}}{\mathrm{Na}_i}\operatorname{sech}^2\left(\frac{e}{2kT}(v+2v_{\mathrm{K}}-3v_{\mathrm{Na}}-v_{\mathrm{ATP}})\right) \tag{A.21}$$

$$\begin{aligned}\mathbf{M}_{6,4} = \frac{-2k_{\mathrm{NaK}}}{\mathrm{K}_i}&\operatorname{sech}^2\left(\frac{e}{2kT}(v+2v_{\mathrm{K}}-3v_{\mathrm{Na}}-v_{\mathrm{ATP}})\right)\\ &-\frac{k_{\mathrm{K}}}{4\mathrm{K}_i}\cosh\left(\frac{e}{2kT}(v-v_{\mathrm{K}})\right)\left(1+\tanh\left(\frac{2e}{kT}(v-v_x)\right)\right)\end{aligned} \tag{A.22}$$

$$\begin{aligned}\mathbf{M}_{6,5} = \frac{-ek_{\mathrm{K}}}{kT}&\sinh\left(\frac{e}{2kT}(v-v_{\mathrm{K}})\right)\operatorname{sech}^2\left(\frac{2e}{kT}(v-v_x)\right)\\ &+\frac{ek_{\mathrm{NaK}}}{kT}\operatorname{sech}^2\left(\frac{e}{2kT}(v+2v_{\mathrm{K}}-3v_{\mathrm{Na}}-v_{\mathrm{ATP}})\right)\\ &-\frac{ek_{\mathrm{K}}}{4kT}\cosh\left(\frac{e}{2kT}(v-v_{\mathrm{K}})\right)\left(1+\tanh\left(\frac{2e}{kT}(v-v_x)\right)\right)\end{aligned} \tag{A.23}$$

All other elements of $\mathbf{M}$ are zero.

FORCING VECTOR ELEMENTS IN SECTION 6.3

$$\begin{aligned}\mathbf{F}_{temp_5} = &-\frac{ek_{\mathrm{Na}}}{2kT^2}\sinh\left(\frac{e}{2kT}(v-v_{\mathrm{Na}})\right)\left(1+\tanh\left(\frac{2e}{kT}(v-v_m)\right)\right)\\ &\times(v-v_h)\operatorname{sech}^2\left(\frac{2e}{kT}(v-v_h)\right)\\ &+\frac{ek_{\mathrm{Na}}}{8kT^2}\cosh\left(\frac{e}{2kT}(v-v_{\mathrm{Na}})\right)\left(1-\tanh\left(\frac{2e}{kT}(v-v_h)\right)\right)\\ &\times v\left(1+\tanh\left(\frac{2e}{kT}(v-v_m)\right)\right)\\ &+\frac{3k_{\mathrm{NaK}}}{2kT^2}\operatorname{sech}^2\left(\frac{e}{2kT}(v+2v_{\mathrm{K}}-3v_{\mathrm{Na}}-v_{\mathrm{ATP}})\right)(v-v_{\mathrm{ATP}})\\ &+\frac{ek_{\mathrm{Na}}}{2kT^2}\sinh\left(\frac{e}{2kT}(v-v_{\mathrm{Na}})\right)\left(1-\tanh\left(\frac{2e}{kT}(v-v_h)\right)\right)\\ &\times(v-v_m)\operatorname{sech}^2\left(\frac{2e}{kT}(v-v_m)\right)\end{aligned} \tag{A.24}$$

$$\begin{aligned}\mathbf{F}_{temp_6} = &\frac{ek_{\mathrm{K}}}{kT^2}\sinh\left(\frac{e}{2kT}(v-v_{\mathrm{K}})\right)(v-v_x)\operatorname{sech}^2\left(\frac{2e}{kT}(v-v_x)\right)\\ &+\frac{ek_{\mathrm{K}}}{4kT^2}v\cosh\left(\frac{e}{2kT}(v-v_{\mathrm{K}})\right)\left(1+\tanh\left(\frac{2e}{kT}(v-v_x)\right)\right)\\ &\frac{ek_{\mathrm{NaK}}}{kT^2}\operatorname{sech}^2\left(\frac{e}{2kT}(v+2v_{\mathrm{K}}-3v_{\mathrm{Na}}-v_{\mathrm{ATP}})\right)(v-v_{\mathrm{ATP}})\end{aligned} \tag{A.25}$$

All other elements of $\mathbf{F}_{temp}$ are zero.

MASS MATRIX ELEMENTS IN SECTION 6.6

$$\begin{aligned}\mathbf{M}_{5,1} = &\frac{9k_{\mathrm{NaK}}}{2\mathrm{Na}_e}A\operatorname{sech}^2\left(\frac{e}{2kT}(v+2v_{\mathrm{K}}-3v_{\mathrm{Na}}-v_{\mathrm{ATP}})\right)\\ &+\frac{k_{\mathrm{Na}}}{8\mathrm{Na}_e}\cosh\left(\frac{e}{2kT}(v-v_{\mathrm{Na}})\right)\left(1-\tanh\left(\frac{2e}{kT}(v-v_h)\right)\right)\\ &\times\left(1+\tanh\left(\frac{2e}{kT}(v-v_m)\right)\right)\end{aligned} \tag{A.26}$$

$$\mathbf{M}_{5,2} = \frac{-3k_{\mathrm{NaK}}}{\mathrm{K}_e}A\operatorname{sech}^2\left(\frac{e}{2kT}(v+2v_{\mathrm{K}}-3v_{\mathrm{Na}}-v_{\mathrm{ATP}})\right) \tag{A.27}$$

$$\mathbf{M}_{5,3} = \frac{-9k_{\mathrm{NaK}}}{2\mathrm{Na}_i} A \operatorname{sech}^2\left(\frac{e}{2kT}(v + 2v_{\mathrm{K}} - 3v_{\mathrm{Na}} - v_{\mathrm{ATP}})\right) - \frac{k_{\mathrm{Na}}}{8\mathrm{Na}_i}\cosh\left(\frac{e}{2kT}(v - v_{\mathrm{Na}})\right)\left(1 - \tanh\left(\frac{2e}{kT}(v - v_h)\right)\right) \times \left(1 + \tanh\left(\frac{2e}{kT}(v - v_m)\right)\right) \quad \text{(A.28)}$$

$$\mathbf{M}_{5,4} = \frac{3k_{\mathrm{NaK}}}{\mathrm{K}_i} A \operatorname{sech}^2\left(\frac{e}{2kT}(v + 2v_{\mathrm{K}} - 3v_{\mathrm{Na}} - v_{\mathrm{ATP}})\right) \quad \text{(A.29)}$$

$$\mathbf{M}_{5,5} = \frac{ek_{\mathrm{Na}}}{2kT}\sinh\left(\frac{e}{2kT}(v - v_{\mathrm{Na}})\right)\left(1 + \tanh\left(\frac{2e}{kT}(v - v_m)\right)\right) \times \operatorname{sech}^2\left(\frac{2e}{kT}(v - v_h)\right) - \frac{ek_{\mathrm{Na}}}{2kT}\sinh\left(\frac{e}{2kT}(v - v_{\mathrm{Na}})\right)\left(1 - \tanh\left(\frac{2e}{kT}(v - v_h)\right)\right) \times \operatorname{sech}^2\left(\frac{2e}{kT}(v - v_m)\right) - \frac{ek_{\mathrm{Na}}}{8kT}\cosh\left(\frac{e}{2kT}(v - v_{\mathrm{Na}})\right)\left(1 - \tanh\left(\frac{2e}{kT}(v - v_h)\right)\right) \times \left(1 + \tanh\left(\frac{2e}{kT}(v - v_m)\right)\right) - \frac{3ek_{\mathrm{NaK}}}{2kT} A \operatorname{sech}^2\left(\frac{e}{2kT}(v + 2v_{\mathrm{K}} - 3v_{\mathrm{Na}} - v_{\mathrm{ATP}})\right) \quad \text{(A.30)}$$

$$\mathbf{M}_{5,7} = -3k_{\mathrm{NaK}}\tanh\left(\frac{e}{2kT}(v + 2v_{\mathrm{K}} - 3v_{\mathrm{Na}} - v_{\mathrm{ATP}})\right) \quad \text{(A.31)}$$

$$\mathbf{M}_{6,1} = \frac{-3k_{\mathrm{NaK}}}{\mathrm{Na}_e} A \operatorname{sech}^2\left(\frac{e}{2kT}(v + 2v_{\mathrm{K}} - 3v_{\mathrm{Na}} - v_{\mathrm{ATP}})\right) \quad \text{(A.32)}$$

$$\mathbf{M}_{6,2} = \frac{2k_{\mathrm{NaK}}}{\mathrm{K}_e} A \operatorname{sech}^2\left(\frac{e}{2kT}(v + 2v_{\mathrm{K}} - 3v_{\mathrm{Na}} - v_{\mathrm{ATP}})\right) + \frac{k_{\mathrm{K}}}{4\mathrm{K}_e}\cosh\left(\frac{e}{2kT}(v - v_{\mathrm{K}})\right)\left(1 + \tanh\left(\frac{2e}{kT}(v - v_x)\right)\right) \quad \text{(A.33)}$$

$$\mathbf{M}_{6,3} = \frac{3k_{\mathrm{NaK}}}{\mathrm{Na}_i} A \operatorname{sech}^2\left(\frac{e}{2kT}(v + 2v_{\mathrm{K}} - 3v_{\mathrm{Na}} - v_{\mathrm{ATP}})\right) \quad \text{(A.34)}$$

$$\mathbf{M}_{6,4} = \frac{-2k_{\mathrm{NaK}}}{\mathrm{K}_i} A \operatorname{sech}^2\left(\frac{e}{2kT}(v + 2v_{\mathrm{K}} - 3v_{\mathrm{Na}} - v_{\mathrm{ATP}})\right) - \frac{k_{\mathrm{K}}}{4\mathrm{K}_i}\cosh\left(\frac{e}{2kT}(v - v_{\mathrm{K}})\right)\left(1 + \tanh\left(\frac{2e}{kT}(v - v_x)\right)\right) \quad \text{(A.35)}$$

$$\mathbf{M}_{6,5} = \frac{-ek_{\mathrm{K}}}{kT}\sinh\left(\frac{e}{2kT}(v-v_{\mathrm{K}})\right)\operatorname{sech}^2\left(\frac{2e}{kT}(v-v_x)\right) + \frac{ek_{\mathrm{NaK}}}{kT}A\operatorname{sech}^2\left(\frac{e}{2kT}(v+2v_{\mathrm{K}}-3v_{\mathrm{Na}}-v_{\mathrm{ATP}})\right) - \frac{ek_{\mathrm{K}}}{4kT}\cosh\left(\frac{e}{2kT}(v-v_{\mathrm{K}})\right)\left(1+\tanh\left(\frac{2e}{kT}(v-v_x)\right)\right) \quad \text{(A.36)}$$

$$\mathbf{M}_{6,7} = 2k_{\mathrm{NaK}}\tanh\left(\frac{e}{2kT}(v+2v_{\mathrm{K}}-3v_{\mathrm{Na}}-v_{\mathrm{ATP}})\right) \quad \text{(A.37)}$$

$$\mathbf{M}_{7,7} = 1 \quad \text{(A.38)}$$

$$\mathbf{M}_{8,8} = 1 \quad \text{(A.39)}$$

All other elements of $\mathbf{M}$ are either as in the previous section, or zero.

FORCING VECTOR ELEMENTS IN SECTION 6.6

$$\mathbf{F}_{temp_5} = -\frac{ek_{\mathrm{Na}}}{2kT^2}\sinh\left(\frac{e}{2kT}(v-v_{\mathrm{Na}})\right)\left(1+\tanh\left(\frac{2e}{kT}(v-v_m)\right)\right) \times (v-v_h)\operatorname{sech}^2\left(\frac{2e}{kT}(v-v_h)\right) + \frac{ek_{\mathrm{Na}}}{8kT^2}\cosh\left(\frac{e}{2kT}(v-v_{\mathrm{Na}})\right)\left(1-\tanh\left(\frac{2e}{kT}(v-v_h)\right)\right) \times v\left(1+\tanh\left(\frac{2e}{kT}(v-v_m)\right)\right) + \frac{3k_{\mathrm{NaK}}}{2kT^2}A\operatorname{sech}^2\left(\frac{e}{2kT}(v+2v_{\mathrm{K}}-3v_{\mathrm{Na}}-v_{\mathrm{ATP}})\right)(v-v_{\mathrm{ATP}}) + \frac{ek_{\mathrm{Na}}}{2kT^2}\sinh\left(\frac{e}{2kT}(v-v_{\mathrm{Na}})\right)\left(1-\tanh\left(\frac{2e}{kT}(v-v_h)\right)\right) \times (v-v_m)\operatorname{sech}^2\left(\frac{2e}{kT}(v-v_m)\right) \quad \text{(A.40)}$$

$$\mathbf{F}_{temp_6} = \frac{ek_{\mathrm{K}}}{kT^2}\sinh\left(\frac{e}{2kT}(v-v_{\mathrm{K}})\right)(v-v_x)\operatorname{sech}^2\left(\frac{2e}{kT}(v-v_x)\right) + \frac{ek_{\mathrm{K}}}{4kT^2}v\cosh\left(\frac{e}{2kT}(v-v_{\mathrm{K}})\right)\left(1+\tanh\left(\frac{2e}{kT}(v-v_x)\right)\right) - \frac{ek_{\mathrm{NaK}}}{kT^2}A\operatorname{sech}^2\left(\frac{e}{2kT}(v+2v_{\mathrm{K}}-3v_{\mathrm{Na}}-v_{\mathrm{ATP}})\right)(v-v_{\mathrm{ATP}}) \quad \text{(A.41)}$$

All other elements of $\mathbf{F}_{temp}$ are zero.

APPENDIX B

PAYNE *et al.* , PHIL. TRANS. R. SOC. A

PHILOSOPHICAL TRANSACTIONS OF THE ROYAL SOCIETY A

Phil. Trans. R. Soc. A (2011) **369**, 4233–4254
doi:10.1098/rsta.2011.0240

Image-based multi-scale modelling and validation of radio-frequency ablation in liver tumours

By Stephen Payne[1,*], Ronan Flanagan[2], Mika Pollari[3], Tuomas Alhonnoro[3], Claire Bost[2], David O'Neill[1], Tingying Peng[1] and Philipp Stiegler[4]

[1]*Department of Engineering Science, Institute of Biomedical Engineering, University of Oxford, Oxford OX1 3PJ, UK*
[2]*NUMA Engineering Services Ltd., The Business Centre, Blackthorn Business Park, Dundalk, Co. Louth, Republic of Ireland*
[3]*Department of Biomedical Engineering and Computational Science, School of Science and Technology, Aalto University, Helsinki, Finland*
[4]*Division of Transplantation Surgery, Medical University of Graz, Graz, Austria*

The treatment of cancerous tumours in the liver remains clinically challenging, despite the wide range of treatment possibilities, including radio-frequency ablation (RFA), high-intensity focused ultrasound and resection, which are currently available. Each has its own advantages and disadvantages. For non- or minimally invasive modalities, such as RFA, considered here, it is difficult to monitor the treatment *in vivo*. This is particularly problematic in the liver, where large blood vessels act as heat sinks, dissipating delivered heat and shrinking the size of the lesion (the volume damaged by the heat treatment) locally; considerable experience is needed on the part of the clinician to optimize the heat treatment to prevent recurrence. In this paper, we outline our work towards developing a simulation tool kit that could be used both to optimize treatment protocols in advance and to train the less-experienced clinicians for RFA treatment of liver tumours. This tool is based on a comprehensive mathematical model of bio-heat transfer and cell death. We show how simulations of ablations in two pigs, based on individualized imaging data, compare directly with experimentally measured lesion sizes and discuss the likely sources of error and routes towards clinical implementation. This is the first time that such a 'loop' of mathematical modelling and experimental validation *in vivo* has been performed in this context, and such validation enables us to make quantitative estimates of error.

Keywords: modelling; radio-frequency ablation; liver; image analysis

*Author for correspondence (stephen.payne@keble.ox.ac.uk).

One contribution of 11 to a Theme Issue 'Towards the virtual physiological human: mathematical and computational case studies'.

1. Introduction

The minimally invasive nature of thermal ablation (the heating of tissue to induce death) makes it a common choice for the treatment of primary hepatocellular cancerous tumours in the liver when the prognosis of surgical resection techniques is poor. Unfortunately, the success rate drops off rapidly with decreased experience: for liver tumours, clinicians with 2–4 years experience achieve 89 per cent survival rates at 2 years, significantly above the 46 per cent survival rate managed by those with fewer than 2 years of experience [1]. This is largely owing to the complex relationship between thermal power and final lesion size, which is very strongly affected by localized perfusion and the presence of nearby large cooling vessels, which act as significant heat sinks in the liver. It is thus very difficult to tailor the heating protocol to the individual patient.

During thermal ablation, such as radio-frequency ablation (RFA), which uses a high-frequency alternating current to induce heating, visualization of the progress of the resulting thermal coagulation is often unavailable. As a result, mathematical modelling plays a vital role in the determination of *in vivo* temperatures to plan and optimize treatment protocols [2,3]. It would be extremely valuable to have a computational tool that, based on individual patient imaging data, could be used to optimize the heating protocol in advance of the treatment. This could also be used as a training tool for the less-experienced clinicians to improve outcome rates where they are at their poorest level.

However, the development of such a tool is extremely difficult because an extensive validation is required before it can be used with confidence in a clinical setting. Such validation requires predictions to be made of the size of the lesion, based solely on routinely available imaging data for either human or animal models, and then compared with the status of the liver tissue after treatment. This requires a combination of mathematical modelling, computational efficiency, accurate image analysis and carefully designed experimental studies; the need for such a team to be gathered to 'close the loop' between prediction and reality is a significant obstacle to achieving this.

In this paper, we present our progress towards this and show the results that we have obtained on animal models. This has been performed through the development and implementation of a multi-scale mathematical model that can be used to simulate the ablation process, based on patient-specific data and images. Using the image analysis, we are able to perform a quantitative validation of the model predictions of lesion size compared with those acquired through histological examination. These are presented and discussed alongside plans to extend the work into human models and hence into clinical practice. This would be the first such simulation tool kit for this therapy in the liver, and has the potential to make a substantive impact on clinical outcomes, as well as providing valuable pointers for future successful work in other organs.

2. Mathematical model

A schematic of the mathematical model is shown in figure 1, illustrating how the different parts of such a model connect. The two major components are the bio-heat model, which uses the heating and blood flow field to predict the tissue

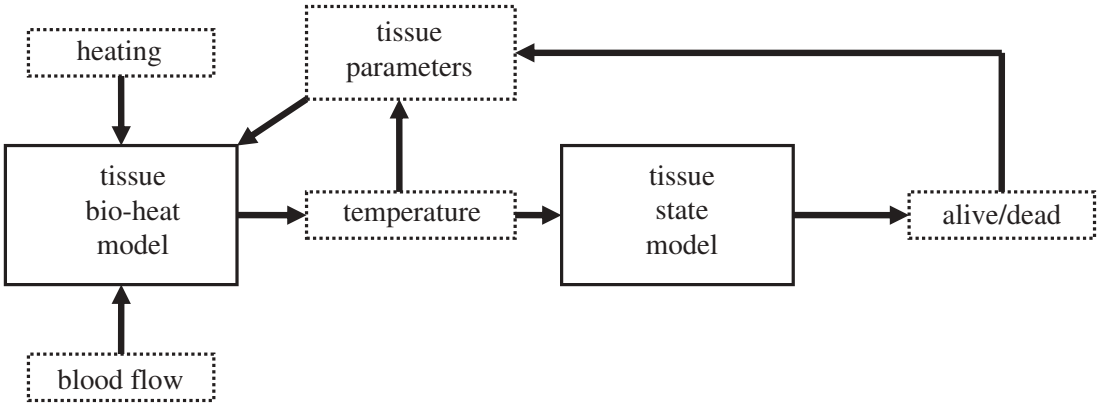

Figure 1. Schematic of mathematical model taken from Payne *et al.* [3].

temperature (which varies both temporally and spatially), and the tissue state model, which requires the tissue temperature profile to predict the state of the tissue (alive or dead). This status in turn affects the tissue parameters, such as thermal conductivity (which may also be temperature dependent), and hence influences the bio-heat model. There is thus considerable interaction between the different sections of the model, which exhibits many nonlinearities.

In order to predict the outcome of a heating protocol, four things are thus required: the heating profile, the blood flow field, a bio-heat model (with parameter values) and a tissue state model (with parameter values). For a review of the literature, see Payne *et al.* [3], where the practical difficulties of choosing models and parameter values are discussed in more detail. In this paper, we describe the practical implementation which we have adopted for our particular application, that of RFA in the liver.

(*a*) *Bio-heat model*

The classical bio-heat equation, the Pennes model, has been widely used in the literature to model the electrical–thermal heating process during the ablation procedure [4–6]. However, the convective heat-transfer term between tissue and blood in the equation is oversimplified, assuming the blood to be a volumetric heat sink and one that is uniformly distributed throughout the tissue [7]. Owing to the absence of an equation to model variations in blood temperature, large deviations have been found between Pennes model predictions and the absolute temperature field in vascularized tissue [8,9]. In order to overcome these shortcomings, many subsequent modifications have been proposed, including those by Wulff [10] and Klinger [11], who considered the local blood mass flux in order to account for the blood flow direction, but continuous equilibrium between tissue and blood temperatures is assumed. Again, the validity of this thermal equilibrium assumption has been questioned under conditions of thermal ablation [12]. Inaccurate estimation of blood cooling effects can greatly affect the prediction of tissue temperature and thus the necrosis zone after the intervention, especially for highly blood-perfused organs such as the liver.

Therefore, in this project, we have proposed a new split-volume bio-heat equation to model the heat transfer during RFA of liver tissue [13]. We adopt the same fundamental physical approach as that of Chen & Holmes [14], who

considered each elemental volume to comprise a tissue fraction and a blood fraction. Separate equations are postulated based on conservation of energy for the tissue and blood phases, respectively,

$$(1-\varepsilon)\rho_{\mathrm{t}} c_{\mathrm{t}} \frac{\partial T_{\mathrm{t}}}{\partial t} = (1-\varepsilon)\sigma_{\mathrm{t}}|E|^2 + (1-\varepsilon)\nabla\cdot(k_{\mathrm{t}}\nabla T_{\mathrm{t}}) - H(T_{\mathrm{t}} - T_{\mathrm{b}}) \tag{2.1}$$

and

$$\varepsilon\rho_{\mathrm{b}} c_{\mathrm{b}} \left(\frac{\partial T_{\mathrm{b}}}{\partial t} + \mathbf{v}\cdot\nabla T_{\mathrm{b}}\right) = \varepsilon\sigma_{\mathrm{b}}|E|^2 + \varepsilon\nabla\cdot(k_{\mathrm{b}}\nabla T_{\mathrm{b}}) + H(T_{\mathrm{t}} - T_{\mathrm{b}}), \tag{2.2}$$

where ρ, c, k, H, ε, $\mathbf{v}$, σ, E and T denote density, specific heat capacity, thermal conductivity, local volumetric heat-transfer coefficient, blood volume fraction, blood flow velocity field, electrical conductivity, electric field and temperature, respectively, and subscripts 't' and 'b' refer to the tissue and blood phases, respectively. The tissue and blood temperatures are the dependent variables to solve, for which the blood flow velocity field and electric field must be prescribed (as described below). In these equations, the first term on the right-hand side is the radio frequency heating source term, the second the heat-conduction term and the third the tissue/blood convective heat exchange term. The bulk flow term appears on the left-hand side of the blood bio-heat equation as part of the total temporal derivative. The heat exchange term between the blood and the tissue represents convective heat transfer via the vascular wall, which can be obtained through Newton's cooling law,

$$H = s_{\mathrm{b}} h_{\mathrm{b}}, \tag{2.3}$$

where s_{b} and h_{b} are the volume-averaged specific surface area and convective heat-transfer coefficient, respectively. For a bundle of vascular tubes of radius R, we can estimate that $s_{\mathrm{b}} = 2V_{\mathrm{b}}/RV = 2\varepsilon/R$ and that $h_{\mathrm{b}} = k_{\mathrm{b}}Nu/2R$, such that $H = \varepsilon k_{\mathrm{b}}Nu/R^2$ [15], where Nu is the Nusselt number, set to be 4.93 for these conditions [16], and V denotes volume. This illustrates clearly that the local volumetric heat-transfer coefficient depends on both the blood volume fraction and the vessel radius.

Differing from traditional bio-heat models, the split-volume bio-heat model incorporates the local thermal non-equilibrium between the blood and the peripheral tissue and uses two separate equations to represent the thermodynamics of the blood and solid tissue phases. When used to examine the separate contribution of different parts of the vasculature, the model behaviour is shown to be dependent on a non-dimensional number, γ, termed the thermal significance coefficient, which is a measure of the relative heat flow between the blood and the tissue volume phases, as described completely in Peng *et al.* [13]. For vessels in the highest generation of the vasculature such as the big arteries and veins, γ is found to be far larger than unity, indicating that the blood in these large vessels essentially holds a constant temperature, in which case, the split-volume bio-heat model can be simplified into the Pennes model; on the other hand, for small vessels in the bottom generations of the vasculature such as arterioles, capillaries and venules, γ is much smaller than unity, suggesting that the blood in small vessels is in continuous equilibrium with tissue temperature, in which case, the model is equivalent to the Klinger model. However, most of the temperature equilibration occurs as the blood travels via the middle

generations of the vasculature such as terminal artery branches, under which circumstance γ is of order unity and hence the split-volume model cannot be further simplified.

In this project, large vessels (diameter greater than 10 mm) can be individually reconstructed from a vessel-enhanced X-ray computed tomography (CT) image, as outlined below, and thus their cooling effects are determined by calculating the exact convective heat transfer on their vessel wall [6]. The cooling effects of very small vessels (diameter less than 0.1 mm) can be considered to be of negligible importance, on the basis that their contribution to vasculature cooling is smallest [13]. Vessels in the middle generations of the vasculature, such as the terminal artery branches, are then modelled as a porous media flow field, as outlined below, and their cooling effects estimated by the split-volume thermal model.

(*b*) *Cell death model*

Once the tissue temperature has been modelled, the second major component of the mathematical model is that which governs the relationship between tissue temperature and tissue state. For this, we have proposed a novel three-state model, outlined in more detail by O'Neill *et al.* [17], extending the existing models that are predominantly based on two states (alive and dead). This three-state model includes an intermediate compartment between the fully alive (A) and dead (D) compartments, which we term the vulnerable (V) state,

$$A \underset{k_\mathrm{b}}{\overset{k_\mathrm{f}}{\rightleftarrows}} V \xrightarrow{k_\mathrm{f}} D, \tag{2.4}$$

where transitions between the states are governed by (temperature-dependent) forward and (temperature-independent) backward rate constants, and A, V and D represent the fraction of cells within each state at each point in the tissue. While most of the literature (see [18] for a very thorough review) uses Arrhenius-based rate coefficients, as proposed by early workers in this area, such as Henriques and Moritz for cutaneous skin burns [19–21], the nature of this exponential form, where the transition rate is proportional to the exponential of the activation energy divided by temperature, results in a highly sensitive constant of proportionality where reported values range over tens of orders of magnitude [18].

Our model is similar to the two- and three-state models proposed by Breen *et al.* [22] and Szasz & Vincze [23], and it has been shown by O'Neill *et al.* [24] that with certain mathematical manipulations, it can be related to the physiologically based model with infinite states as proposed by Jung [25–27]. The biological implication of this is that the vulnerable compartment accounts for cells that are at elevated risk of critical damage.

For simplicity, all complex stages of the path to cell death are incorporated into a single-damage mechanism; thus, as the processes from alive to vulnerable and from vulnerable to dead are taken to be two stages of the same result, a single forward rate constant, k_f, is used. This rate constant is nonlinear, being proportional to the combined proportion of cells in the vulnerable and dead compartments $(1 - A)$,

$$k_\mathrm{f} = \overline{k_\mathrm{f}} \mathrm{e}^{T/T_\mathrm{k}} (1 - A), \tag{2.5}$$

where $\overline{k_f}$ is a scaling constant and T_k is a parameter that sets the rate of the exponential increase with temperature. The backward rate constant, simulating any self-healing, is set to a value that is invariant with temperature, as this was found to provide a good fit to the experimental data.

Tailor-made heating experiments for model parameterization were carried out at constant temperatures on cultures made up of two cell lines: human liver hepatocellular carcinoma (HepG2) and human lung fibroblast (MRC-5). Two pure cultures and three co-cultures (75/25, 50/50 and 25/75) were cultured overnight at 37°C. For each time and temperature combination, the culture medium was replaced with a preheated medium and then incubated in a preheated heating cabinet. The temperatures were 55°C, 65°C, 75°C, 85°C and 100°C, and the heating times were 300, 600 and 900 s. Post-heating, the medium was replaced with another medium at 37°C and spiked with 20 µl methanethiosulphonate (MTS) reagent. Fluoroscopy measurements were taken at 2, 26 and 50 h after heating, the readings signifying the metabolic activity of the living cells, i.e. the relative proportions of alive and dead cells. Data were normalized to a control value at 37°C and there were five or six repeats of each plate, which had four separated wells. The data were fitted to the model giving average r.m.s. errors between the model predictions and the data of 1.40 per cent. This compares favourably with the s.e. of 3.39 per cent for the experimental data.

A second part of the model for cell death, which accounts for delayed cell death occurring post-heating after the tissue has returned to normothermia, has also been proposed and validated against the experimental data [17]. Crucially, the data show that there appears to be a threshold for cell viability, estimated to be 80 per cent, such that if the local viability is reduced beyond this level, the cells will inevitably progress to a dead state eventually. This is of particular value computationally, as the simulations need not be run past the time at the end of heating.

Of further significant benefit to the multi-scale simulation of RFA treatments is that the mixed co-culture experiments have highlighted different thermal resistances of different cells. We note that this will be of considerable importance in future refinement of the model for patient-specific treatment planning, where conditions may vary widely.

(*c*) *Electrical heating model*

At the frequencies employed in RFA (300 kHz–1 MHz) and within the area of interest (it is known that the electrical power is deposited within a small radius around the active electrode), the tissues can be considered purely resistive as the displacement currents are negligible. Using a quasi-static approach, the distributed heat source q (Joule loss) is given by [28]

$$q = \mathbf{J} \cdot \mathbf{E}, \tag{2.6}$$

where $\mathbf{J}$ is the current density and $\mathbf{E}$ is the electric field intensity. The values of these two vectors are evaluated using Laplace's equation,

$$\nabla \cdot (\sigma \nabla V_{PD}) = 0, \tag{2.7}$$

where V_{PD} is the voltage. Joule heat can thus be written as

$$q = \sigma |\nabla V_{\mathrm{PD}}|^2. \tag{2.8}$$

In the literature, the voltage is usually set to be a constant number on the surface of the radio-frequency (RF) electrode probe needle and the potential field generated around the probe is solved numerically, using equation (2.7) (e.g. Panescu *et al.* [5]). This approach, though theoretically accurate, suffers from a high computational cost because of the required fine volume mesh on the surface of the very thin probe tips. Moreover, the exact position of the whole electrode probe is not always available in CT imaging [3], and the calculated Joule heat has been found to be very sensitive to the probe position [29]. Therefore, it is highly desirable that the deposited Joule heat during RFA can be estimated without prior knowledge of the whole electrode geometry in the tissue.

In practice, the electric field strength generated by an RF electrode probe is only sufficiently high to cause significant direct heating very close to the electrodes, thermal conduction contributing most of the tissue heating at distances farther from the electrode [30]. This raises the possibility of enclosing the thermal energy generated locally by the electrode inside a few voxels containing the electrode probe. Thus, in our electro-thermo simulation, we use a few point sources to represent the power delivered by the electrode, based on the estimation from an analytical analysis of charge distribution and electrical field of the radiofrequency interstitial tumor ablation (RITA) probe used in the animal model experiments here (StarBurst Radiofrequency Ablation, AngioDynamics; www.angiodynamics.com).

As the full details of the analytical study will be presented separately, a brief overview is given here. The analysis starts by solving the charge distribution on a line conductor of finite length, a simplified geometry of the electrode probe. Coulomb repulsion pushes charges out towards the ends, just as the charge on a solid conductor flows to the surface. However, no explicit analytical solution of the charge distribution has been found in the literature; in fact, it has been suggested that the problem itself may be ill-posed, the answer depending on the particular model used to represent the conductor [31].

In our approach, based on the previous study of Andrews [32], we assume that the charge density is uniform apart from at the ends. The radio between the charge density at two ends of the conductor and the middle part can be obtained using a moment method of formulation, given as

$$R_\rho = \frac{\rho_{\mathrm{end}}}{\rho_{\mathrm{mid}}} = \frac{\ln(L/Nr) + \gamma/2 + \ln((N-3)/(\sqrt{2N-3}))}{\ln(L/Nr) - 3/2(N-1)}, \tag{2.9}$$

where $\gamma \approx 0.5772$ is Euler's constant, L is the conductor length, r is the conductor radius and the end of the conductor Δl is assumed to be $1/N$ of the whole length of the conductor. With the charge density ratio, the joule heat generated by the probe end and the middle part is given as (assuming the total deposited power to be P)

$$q_{\mathrm{end}} = \frac{R_\rho^2 P}{2R_\rho^2 + (N-2)} \tag{2.10}$$

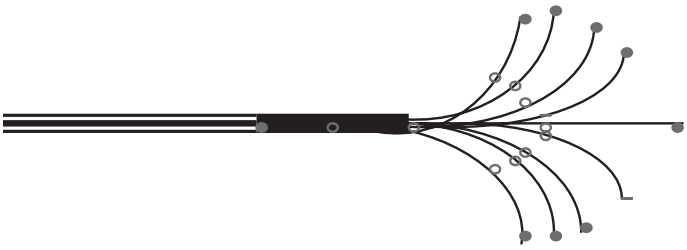

Figure 2. Schematic of point power sources used in the simulation, the power delivered at the tip ends and the probe shaft's end (filled circles) is higher than the power deposited at other points (unfilled circles).

and

$$q_{\mathrm{mid}} = \frac{P}{2R_\rho^2 + (N-2)}. \tag{2.11}$$

The RITA probe needle used in the project has a diameter of 0.5 mm. The needle length varies from 1 to 4 cm and hence we use the average, $L = 2.5$ cm. The selection of section number N is, however, somewhat arbitrary but must satisfy a preliminary condition $N = L/\Delta l \ll L/r$ [19]. We choose $N = 10$ here, thus obtaining a power ratio of $q_{\mathrm{end}}/q_{\mathrm{mid}} \approx 2.5$.

Thus, as shown in figure 2, 21 electrical sources were placed in the simulation in the following positions: tip ends (9), tip middles (9), tip intersection (1), probe shaft's middle (1) and probe shaft's end (1). The magnitude of power delivered at the tip ends and the probe shaft's end will be much higher than that of the rest of the electrical sources. Assuming the whole power input is P, the power distribution will be: tip ends ($9 \times 2.5/36P$), tip middles ($9 \times 1/36P$), tip intersection ($1/36P$), probe shaft's middle ($1/36P$) and probe shaft's end ($2.5/36P$).

Although this approach is a simplification to the actual heating distribution, the improvement in computational time required is a considerable bonus, given the need to perform simulations rapidly in a clinical setting. Examination of the model predictions with this model shows that the heating distribution is 'smoothed out' by the conduction of heat within the tissue and convection within the blood stream, thus the particular details of the heating point sources appear to have only a limited effect on the final lesion size. The most important factor appears to be that the heating is distributed along the probe tips and shaft.

(*d*) *Flow model*

The continuum porous media flow field can be constructed as an extension of the existing CT-visible vasculature, by setting porous media flow sources and sinks at boundaries of the vessel tree to mimic the flow of blood from the large vessels to those in the middle generations of the vasculature (modelled using a porous medium approach). This approach incorporates the patient-specific information of individual vascular geometries and hence better represents the vascular-mediated cooling. As a simplified case, this model was used to analyse the cooling effects of a CT-visible vessel and its unregistered branches [33]. Strong

directional effects of perfusion on the tissue temperature distribution have been found, which is confirmed by recent experiment results [34]. Therefore, the same model equations are applied to the real vascular geometries in the liver, as presented in this paper.

Using the theory of porous media, Darcy's law states that the flow velocity is the gradient of pressure,

$$\boldsymbol{u}_{\mathrm{b}} = -\frac{\kappa}{\mu\varepsilon^{2/3}}\nabla p, \tag{2.12}$$

where κ is the permeability of the medium and μ is the dynamic viscosity of the fluid. The pressure field, p, can be evaluated using Laplace's equation based on continuity of blood flow velocity,

$$\nabla \cdot \boldsymbol{u}_{\mathrm{b}} = \nabla \cdot \left(-\frac{\kappa}{\mu\varepsilon^{2/3}}\nabla p\right) = 0. \tag{2.13}$$

To solve equation (2.13), boundary conditions must be specified on the organ boundary and the CT-constructed vessel tree. In our model simulation, mixed boundary conditions are used by setting either flow velocity $\boldsymbol{u}_{\mathrm{b}}$ or pressure value p on all boundary points. On the organ boundary, a Neumann boundary condition is used, given as $\boldsymbol{u}_{\mathrm{b}} = 0$; while on the CT-constructed vessel tree, a Dirichlet boundary condition is used: a small positive pressure is applied on the portal vein vessel wall and a small negative pressure is applied on the hepatic vein vessel wall. This drives the porous medium flow, which mimics the middle generations of the vasculature, as described above.

3. Image analysis

As outlined in the mathematical model in §2.4, we now examine how the geometric models were generated. The data included images from two pigs, both during and after RFA. The images were acquired at arterial, portal venous and hepatic venous phases and with forced breath-hold techniques to minimize breath-related motion. The data were imaged at the Medical University of Graz using a 320-line Aquilion ONE CT scanner (Toshiba Medical Systems, Otawara, Japan). The images were scanned with a matrix size of $512 \times 512 \times 320$ and a resolution of 0.4 and 0.5 mm for in-plane and out-of-plane, respectively.

In the image analysis, we extracted the geometric models of the liver, hepatic artery, portal vein, hepatic vein and location of RFA needle tips. In this paper, healthy pigs were used and thus tumour segmentation was not needed. The locations of needle tips were extracted from intra-operative volumes (imaged during the RFA treatment), whereas anatomic structures were extracted from post-operative volumes (imaged after the RFA treatment). With registration, each structure was guaranteed to be spatially aligned in the reference frame.

The proposed image analysis framework has five steps, outlined in detail below: (i) registration of all data to the selected reference frame, (ii) segmentation of liver outline, (iii) segmentation of vessels, (iv) segmentation of the induced lesion, and (v) manual processing and surface meshing.

(a) Registration

Not all deformations could be removed with the forced breath-hold technique, so an additional registration was used. We used in-house software similar to Rueckert *et al.* [35]. Such approaches have been previously used in liver motion estimation [36]. In the registration, one of the volumes was assigned as a target, and all other volumes denoted as source volumes were registered one by one with the target; first by rigid and then by non-rigid transformation. The non-rigid transformation was parametrized as a cubic B-spline free-form deformation model with control points positioned in a regular lattice [35,36].

Normalized mutual information (NMI) was used to measure the similarity between the volumes [37]. In optimization, the inverse of the NMI between the target and the source volume was minimized with respect to the transformation parameters. We used simplex minimization for the rigid model and conjugate gradient minimization for the non-rigid model [38]. To speed-up the computation, we used hierarchical coarse-to-fine optimization. We used a two-level image pyramid, where the coarse-level resolution was 2.0 mm and the fine resolution was 1.0 mm in each direction. Similarly, the control point distance was hierarchically refined from 40 to 20 mm and finally to 10 mm.

(b) Liver segmentation

We have developed a new hybrid segmentation method for liver outline. The method is based on landmarking followed by direct and indirect liver segmentation. In landmarking, the goal was to extract the structures that are easy to segment and use them to limit the segmentation in the internal part of the abdominal cavity. Our approach is similar to the landmarking presented by Rangayyan *et al.* [39]. First, the contrast-enhanced CT image was divided in two parts as follows. Air was segmented and components connecting the image borders were marked as a background. The background was morphologically opened to remove external artefacts, the largest internal component was marked as a body, and all other tissues were marked as non-body. Subsequently, the body was divided into thoracic and abdominal cavities based on the location of the diaphragm. We segmented the lung lobes and fitted two quadratic surfaces representing the diaphragm through the bottom of the lobes [39]. The surfaces were combined and the thoracic cavity above the diaphragm was removed.

Finally, we divided the abdomen into internal and peripheral parts. The skeleton was segmented with the region-growing algorithm. We then formed an intact skeletal armour by closing the skeleton in the head–feet direction. The previously extracted non-body tissue and the armour were assigned in the same class and morphologically closed. This removed all the peripheral tissue located inside the body but external to skeletal bones.

In indirect segmentation, the internal part of the abdominal cavity was further processed by iteratively removing non-liver tissue. First, fat and internal air were segmented and morphologically opened with large structuring elements. This process divided the abdominal cavity into separate organs, the largest of which is the liver.

In direct segmentation, the intensity distribution of the healthy liver tissue was estimated. The indirect segmentation above provided an initial liver mask for intensity distribution estimations. The liver was segmented with region growing.

Holes, e.g. vessels, were then closed with morphological operations. The process was repeated to all registered post-operative volumes: arterial, portal venous and hepatic venous phase volumes. This results in six different liver segmentations for a single liver. To form a consensus result, a voxel-wise majority of voting was applied to indirect and direct segmentations.

(*c*) *Vessel segmentation*

The hepatic vessels were extracted employing the tried and true skeleton-based approach first introduced by Selle *et al.* [40], further developed with multi-scale and matched filter approaches, intensity ridge-tracking and mathematical morphology.

Matched filters refer to Hessian-based vessel enhancement filters, which characterize local scale-dependent second-order variations around a shape primitive, and thus the likelihood of a vessel, by the eigenvalues of the Hessian matrix of a Gaussian-filtered image. The standard deviation of the Gaussian kernel is chosen according to the desired vessel size, and filter responses with several vessel sizes are merged into one [41]. To make computation practical, multi-scale Hessian convolution was implemented using the image-pyramid approach. The result both enhances vessels and removes noise, so no additional pre-processing is required.

The hepatic vessels were segmented in two phases—the first being wavefront region growing with user initiation. Wavefront implementation supports high-level control over propagation, e.g. topological constrains, and it resolves large- to medium-sized vessels using a single threshold. The smallest vessels were segmented in the second phase, which is a ridge-oriented alternative to earlier locally adaptive schemes, but which differs from the usual merging and reconnection schemes. In this iterative scheme, the initial segmentation is extruded graph-wise using a watershed transform [42]. It can be thought of as propagating both at the watershed line (intensity ridge) and towards the watershed minima, from which the former was extracted using heuristic graph analysis. The method is inherently capable of growing over small gaps and extracting structures down to unit voxel thickness. Finally, a marker-controlled watershed transform for vessel boundaries was performed to complete the segmentation of small vessels.

In post-processing, the segmented vessels were converted into piecewise linear skeletons using a top-down minimum-cost traversal balanced by two distance fields. Conversion to the skeletal domain reveals the vessel tree structure for qualitative analysis, and the transform is approximately invertible, thus it can be used as an intermediate step within the segmentation pipeline. In our previous work [43], this method was proven to be high performing and capable of extracting 97 and 75 per cent of the vessels equal to or above the radius of 2.0 or 1.0 voxel units, respectively. With regard to sensitivity, the results showed improvements over the existing methods.

(*d*) *Lesion segmentation*

The applied lesion segmentation process was similar to direct segmentation of the liver. The intensity distribution of the lesion was estimated and a region-growing algorithm was applied. The result was morphologically opened to remove

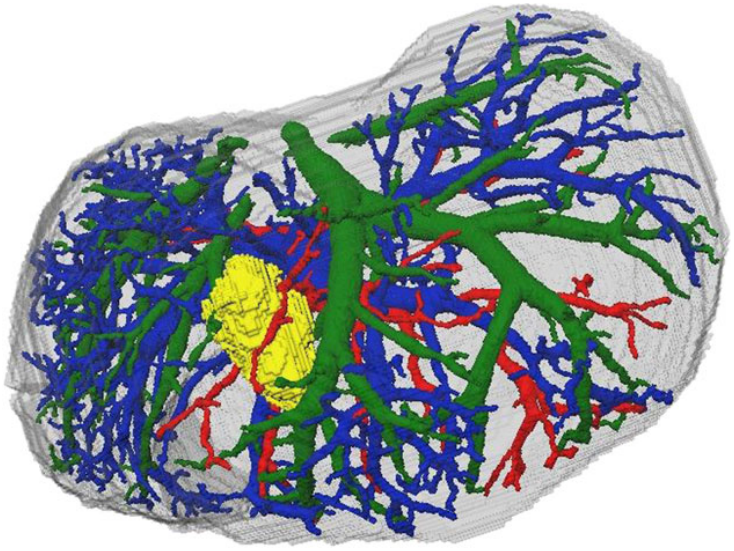

Figure 3. An example of reconstructed geometry: liver outline (transparent), hepatic artery (red), portal vein (blue), hepatic vein (green) and RFA lesion (yellow).

overflow to adjacent structures. The process was repeated for all registered post-operative volumes. The voxel-wise majority voting was applied for final segmentation.

(*e*) *Manual refinement and meshing*

After the automatic and semi-automatic segmentation, manual refinement of the segmentation results was performed. For liver and lesions, slice-by-slice correction, with ITK-SNAP [44] (www.itksnap.org), was performed. For vessels, we used in-house tools developed for semi-automatic pruning of a vessel tree in the skeletal domain. The needle tips were extracted by hand using intra-operative series. Finally, the geometric models of anatomic structures were produced from image data using the marching cubes approach [45].

(*f*) *Conclusions*

An example of the reconstructed liver geometry is shown in figure 3, illustrating the different components of the vascular tree and the lesion. The high quality of the reconstruction enables the mathematical model to be implemented with confidence, as described in the subsequent section.

4. Numerical model implementation

In this section, we describe the practical implementation of the mathematical model outlined in §2, using the physical geometries generated, as outlined in §3. In particular, we focus on the approaches taken to minimize computational expense, as this will be a critical requirement if treatment protocols are to be optimized and hence used in clinical practice.

(*a*) *Finite-element method discretization of the coupled differential equations*

The numerical implementation of the coupled differential equations is performed using the finite-element method, resulting in a spatial discretization of the computational domain. The tetrahedral mesh used for the computation is obtained by a process described at the end of this section.

Each equation is integrated over time using a backward difference formula of order 2, which in the case of the bio-heat equations amounts to expressing the diffusive, convective and forcing terms with respect to the new value of the temperature. This method (implicit in time) has the advantage of being stable and reads, for a second-order discretization of the time derivative,

$$\varepsilon\rho_{\mathrm{b}}c_{\mathrm{b}}\frac{3T_{\mathrm{b}}^{n+1}-4T_{\mathrm{b}}^{n}+T_{\mathrm{b}}^{n-1}}{2\Delta t}=\varepsilon Q_{\mathrm{RFA,b}}^{n+1}+\varepsilon\nabla\cdot(k_{\mathrm{b}}\nabla T_{\mathrm{b}}^{n+1})+H(T_{\mathrm{t}}^{n+1}-T_{\mathrm{b}}^{n+1})-\varepsilon\rho_{\mathrm{b}}c_{\mathrm{b}}(v\cdot\nabla)T_{\mathrm{b}}^{n+1},\tag{4.1}$$

where the superscript 'n' denotes the approximation at time $n\Delta t$, Δt being the time step of the simulation and the case for $n=0$ is treated with a first-order discretization of the time derivative. The full linear system obtained from the discretization of the complete model is solved iteratively with a bi-conjugate gradient method and preconditioned with an incomplete lower and upper triangular matrix factorization.

(*b*) *Implementation with the* Elmer *code*

The core finite-element procedures are based on the open source multi-physics code Elmer [46]. The existing solvers written in Fortran 90 for basic models (advection–diffusion equation, Poisson equation) have been modified to deal with our particular model. The three resulting solvers (bio-heat equations, porous flow and cell death model) are weakly coupled and called iteratively within each time step.

(*c*) *Bio-heat equations implementation*

The coupled blood and tissue equations are solved by strong coupling through the heat transfer between the two domains. They are nonlinear owing to the linear dependency of thermal conductivity on temperature and are linearized with a fixed-point algorithm (see table 1 for the values of model parameters used here). Assuming that we are dealing with only mild variations of the properties with temperature, the Picard linearization can be used as an iterative method. The heat transfer is through convection and diffusion, therefore the finite-element implementation of the heat equation uses the Galerkin least-squares stabilization to prevent numerical oscillations. In order to model the various heat-transfer conditions at vessels walls, both fixed and convective boundary conditions are implemented for tissue and blood temperatures. A $T=37^{\circ}\mathrm{C}$ condition allows a strong cooling effect from blood, whereas the convective transfer produces a relaxation of the preceding condition. The convective transfer can be described by the following relation:

$$-k\frac{\partial T}{\partial n}=\alpha(T-37),\tag{4.2}$$

Table 1. Values of model parameters used in simulations.

parameter	description	value
ρ_b, ρ_t	blood and tissue densities	$1.06 \times 10^3\,\mathrm{kg\,m^{-3}}$
c_b	blood heat capacity	$4.18 \times 10^3\,\mathrm{J\,(kg\,K)^{-1}}$
c_t	tissue heat capacity	$3.6 \times 10^3\,\mathrm{J\,(kg\,K)^{-1}}$
c_t^*	tissue heat capacity in dead cells	$0.67 \times 10^3\,\mathrm{J\,(kg\,K)^{-1}}$
k_b, k_t	blood and tissue heat conductivities	$0.5121 \times (1 + 0.00161 \times (T - 310))\,\mathrm{W\ (m\,K)^{-1}}$
H	convective transfer coefficient	$24.4 \times 10^4\,\mathrm{W\ (m\,K)^{-1}}$
ε	blood volume fraction	0.1
κ	permeability	$2.0 \times 10^{-2}\,\mathrm{m^2}$
μ	dynamic viscosity	$4.6 \times (2.414 \times 10^{-5} \times 10^{247.8/(T-140)})\,\mathrm{Pa\,s}$
k_f	forward rate constant	$3.33 \times 10^{-3}\,\mathrm{s^{-1}}$
k_b	backward rate constant	$7.77 \times 10^{-3}\,\mathrm{s^{-1}}$
T_k	parameter of cell state model	40.5°C

where α is the heat-transfer coefficient and n the outer normal to the boundary. T is measured in degrees Celsius, relative to body temperature (assumed to be constant at 37°C). Equation (4.2) is applied at the walls of the (large) individually registered vessels, as described earlier. The heat-transfer coefficient is expressed as a function of the blood conductivity and the vessel radius. A fixed $T = 37$°C condition is applied on the outer wall of the liver to represent the heat-adjacent organ heat sink.

(*d*) *Joule heating modelling*

As the joule heating is proportional to the square of the gradient of the electric potential distribution throughout the liver tissue, we would normally have to solve the Poisson equation with a fine resolution near the needle surface in order to account for the steep gradients. One way to improve the solver efficiency is to approximate the joule heating by lumping the heat generation distribution into specified points on the needle (see §2.3 and figure 2). The sum of the heat generated adjacent to the needle surface can then be added into the heat equation directly as power source terms at these specific points and smoothed with a Gaussian function. The total electric power, which is time-dependent, and tracked by the StarBurstXL generator, is then shared between all the smoothed point sources. In order to approximate the sharp drop in tissue electric conductivity owing to the presence of vapour when the temperature goes above 100°C, we set the local electric power source term to zero in the heat equation when $T > 100$°C. This allows us to approximate the material properties evolution linked to phase change and prevents very high non-physical temperatures.

(*e*) *Pressure equation and porous flow modelling*

The porous blood flow used in the convection term of bio-heat equations is calculated from the gradient of the pressure, which is the solution of the Poisson equation. The blood flow, owing to the small vessel branches that are not visible as they are below the CT scan resolution, is modelled by assuming a porous flow boundary condition on the vessel wall surface. We can therefore approximate this

porous flow with a pressure distribution on the vessel wall that, in turn, forms the boundary condition for the solution of the Poisson equation. Indeed, fixed positive (respectively, negative) pressure values on input (respectively, output) vessels walls allow the definition of a reasonable approximation of porous blood flow. This modelling choice has the advantage of being numerically stable as no point sources have to be introduced in the Poisson equation for the pressure. The values of pressure at boundaries are guided by the data of the regional hepatic blood flow $q = 26\,\mathrm{ml}\,100\,\mathrm{g}^{-1}\,\mathrm{min}^{-1}$, which is then used to define an average target velocity across the liver tissue porous flow region. In addition to the fixed pressure on the vessel walls, a zero pressure flux boundary condition is applied on the liver outer wall.

(*f*) *Cell death model implementation: resolution of equations and modification of heat equation*

The three-state tissue death model for necrosis is computed by solving the coupled transient equations expressed in alive and dead variables with initial states $A = 0.99$ and $D = 0$ over the computational domain. The vulnerable variable is then easily derived. A fixed-point method is implemented for nonlinearities arising from the temperature dependence of the forward rate constant in the mathematical model. The solution of this model is then used to modify some of the material parameters in the temperature equations. Indeed, to model the poor convection in carbonized cells, the convection term is locally set to zero when $D > 0.8$, which is the critical threshold of cell viability in the model. A modified heat capacity value is also used locally below this threshold.

(*g*) *Parallel computing*

A first parallel implementation of the finite-element code, based on mesh partition, uses the message passing interface standard for inter-processes communication, and allows the distribution of the resolution of different parts of the computational domain to multiple processors. The Elmer-integrated meshing tool (Elmer Grid), using the METIS library, creates the suitable mesh partitions. The use of the METIS library is well adapted to complicated geometries, as it ensures that the number of shared nodes between the partitions, and consequently also the amount of inter-processor communication during the parallel computation is minimized. An optimized parallel implementation is currently under development, one that takes advantage of potential model simplifications, guided by the more extensive validation of numerical results that are being gathered currently.

(*h*) *Meshing*

The volume-meshing strategy for the complicated liver vessel tree structure is based on a linear four-noded tetrahedral element. The open source pre-processor EnGrid has been substantially modified to provide different surface mesh preparation tools for the segmented liver/vessel wall, which has a jagged and castellated surface mesh. The resulting surface mesh of the integrated portal vein, hepatic vein, hepatic artery and liver wall provides a watertight boundary for the volume meshing. The volume meshing is implemented via EnGrid with a manual

mesh refinement. The adaptive mesh refinement is currently under development. The surface modification includes smoothing and coarsening of the segmented mesh in order to optimize the element count and the solution time. These surface modification tools are part of the simulation development process and although they will be available to the clinician, it is expected that we will have decided upon a suitable surface mesh density by the end of the image-based multi-scale physiological planning for ablation cancer treatment (IMPPACT) project. The surface mesh density will then be fixed and the final software will allow us to more easily automate the surface preparation and volume-meshing stages into the intervention planning system infrastructure. This is the only practical approach for clinicians who have no experience in the use of computational engineering simulation tools.

Typical surface mesh sizes are of the order of several hundred thousand triangular elements with resulting volume meshes of the order of 1–3 million tetrahedral elements. The mesh size is partly dependent on the number of small vessel branches near the ablation zone. The more of the small vessel branches there are, the more intricate the surface mesh and thereby the larger the number of elements in the volume mesh. The resolution from the CT scan, and thus the resolution of the segmentation, determines the vessel tree resolution. We expect the patient data to have fewer small branches than the pig data owing to the different contrast enhancement procedures used in clinical practice; therefore, the patient meshes and solution times ought to be faster and easier to implement than the pig simulation models.

We present here the results of the numerical simulation of two RFA processes on pig livers, namely RFA#26 and RFA#42. In both cases, the experimental data for electrical power source and geometry are available as inputs of the model. Indeed, the total electrical power over time is tracked by the RFA generator, and the segmentation of CT scans provides a detailed liver geometry (outer wall, hepatic artery, hepatic vein and portal vein). Moreover, the positions of the needle tips are also extracted. From these data, the heating source term and porous convection terms in the bio-heat equations can be defined, as well as the boundary conditions for the pressure solver.

Tetrahedral meshes were created here from the watertight surface mesh of the liver outer wall and inner vessel trees. After extraction of a refined mesh in a sphere around the segmented lesion, the resulting meshes for RFA#26 and RFA#42 contain 800 000 and 1 800 000 tetrahedral elements, respectively. These meshes describe the small vessel branches around the heating source in order to take into account their cooling effect in the RFA process. The density of the mesh is thus conditioned both by the geometry (small vessels branches inducing small surface elements) and by the numerical resolution of the model (electrical heating at smoothed point sources combined with porous flow convection). In particular, a fine mesh needs to be defined around the heat sources to eliminate numerical oscillations when porous flow convection is applied.

5. Results and discussion

In §§2–4, we have presented the necessary components of the tool: the mathematical model and its implementation, and the generation of the individual

subject geometry. We now present the results of the simulations and compare them with the experimental measurements, enabling us to perform a quantitative validation of the model predictions.

The implementation of the mathematical model has been validated over several test cases provided by RFA experiments on pig livers. Control of the ablated tissue volume is the key feature of the patient-specific intervention planning system for use by the clinicians. The segmentation of the CT scan of the ablated tissue is therefore used for the comparison between the experimental lesion and the numerically predicted one. This segmentation gives the ablated tissue volume just after the RFA process, and one week/month later, in order to take into account the possible healing of cells. According to the mathematical model for cell death, the critical threshold of cell viability $D > 0.8$ is then used to compute the boundary of the numerically predicted lesion.

The temperature distribution in the tissue, which is a function of the power input magnitude and distribution, the cooling effect of the vessels, the tissue and blood material properties and the tissue perfusion, can also be compared with the experimental data at some precise locations. In fact, five thermocouples placed at the ends of the RFA probe tips track the tissue temperature throughout the RFA process. This tracking of the temperature provides a control of the intermediate results/variables of the mathematical model, and is essential for the validation of the cell death model. More extensive temperature measurements would, however, be very valuable to provide a direct validation of the bio-heat model (as opposed to the whole model validation performed here) and this will be the subject of future work.

The computation is run in parallel on a cluster with three nodes, each node having two CPUs. Under these conditions, the computation of each RFA process (approx. 10 min in real time) needs approximately 4 h to complete. The speed-up factor with sequential computation is optimal for linear system assembly steps. However, the scalability of the linear solvers has still to be improved to increase the global speed-up factor. The results (temperatures, blood velocities, dead elements, etc.) are written out at specified time steps for visualization. The tissue temperature for RFA#26 at 600 s after ablation start is shown in figure 4*a* to illustrate both the localized nature of the heating and the large amount of cooling provided by the vasculature in particular regions of the liver. It is clear that the interaction between the heating and the temperature fields is highly complex, justifying the need for such a sophisticated model.

The remainder of figure 4 shows the results of both the predicted dead zone and the experimentally measured lesion size for figure 4*b* (RFA#26) and figure 4*c* (RFA#42). The sections of the vessel trees in the surrounding region are also shown, illustrating the importance of the heat sink effect. This cooling influence of the vessels modifies locally the temperature distribution and in turn reduces the predicted ablation zone. The correct thermal boundary conditions on the vessel walls near the ablation zone are therefore important for the accuracy of the final prediction. In particular, the application of convective boundary conditions for temperature allows the predicted ablation volume to wrap around some thermally non-significant vessels, as shown at the top of the figure for RFA#42.

These results show very good agreement for the size and shape of the ablated zone between the predicted results and the actual data. A more quantitative comparison is performed by computing the maximal deviation between the

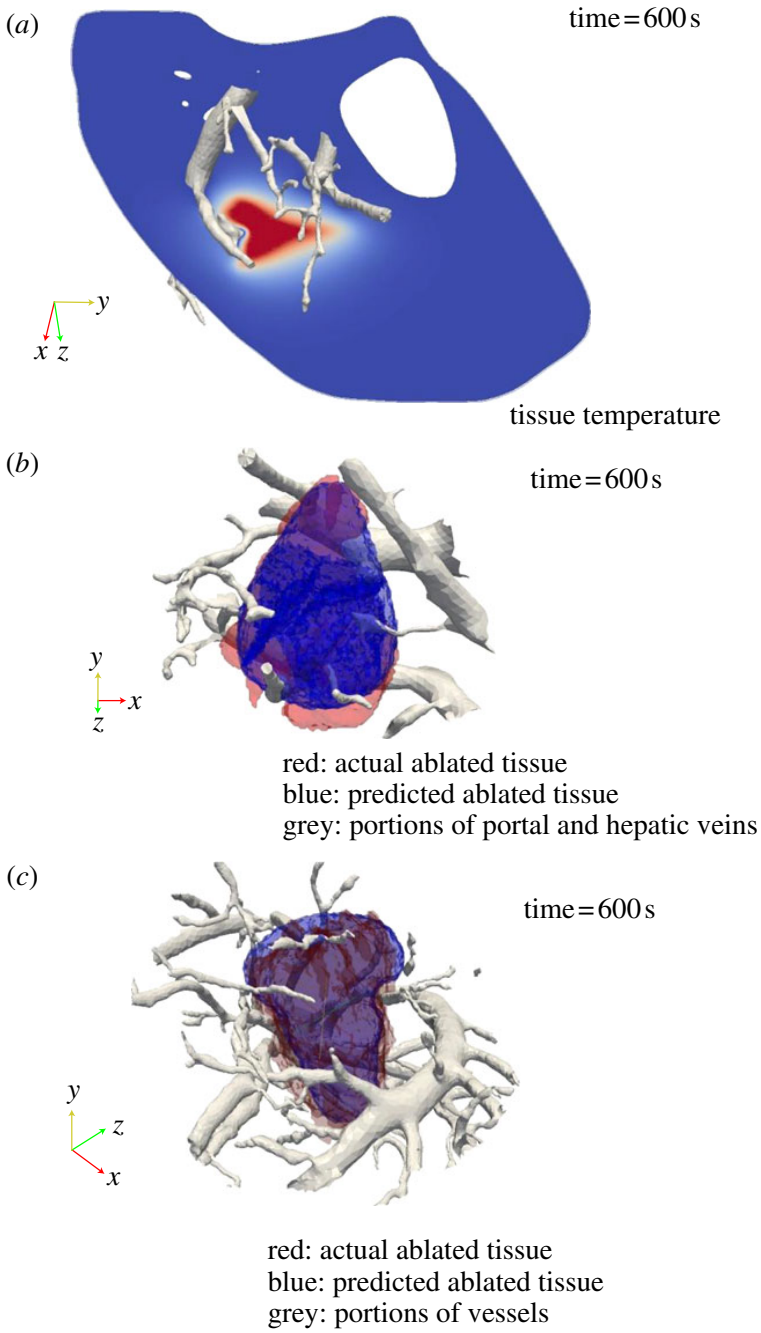

Figure 4. (*a*) Schematic of tissue temperature field at the end of the ablation protocol for RFA#26, the temperature distribution from 310 (blue) to over 340 K (red) being shown on a cut through the liver; comparison between the predicted (blue) and the actual (red) volumes of ablated tissue cells at the end of the protocol for (*b*) RFA#26 and (*c*) RFA#42.

predicted and the actual lesion surfaces: likely to be the parameter of greatest clinical importance in ensuring that the predictions are sufficiently accurate for clinical practice. The values calculated here are 4.5 and 4.2 mm for the RFA#26 and RFA#42 pigs, respectively, with lesion characteristic lengths of 27.5 and 27 mm. Furthermore, the numerical temperatures at the tips ends are also in good agreement with the experimental data (data not shown). The volumes of the segmented and predicted lesions are given in table 2,

Table 2. Volumes of segmented and predicted lesions, for RFA#26 and RFA#42.

	volume of segmented lesion (mm^3)	volume of predicted lesion (mm^3)
RFA#26	8732	10 623
RFA#42	8618	13 577

again showing good agreement. Owing to the low thermal conductivity of the blood and the tissue, the temperature variation is also quite localized close to the heating source, which allows us to limit the computational domain to a volume approximately 35 mm radius from the centre of the ablation zone. This has a significant impact on the computational requirements of the simulations.

It should be noted that these results, although very encouraging, are still only preliminary, with only two comparisons being made. Now that the loop is completed, though, we will be performing further validation using further animal models. This will enable us to gain a greater insight into the likely quantitative error of our model. This dataset will also be invaluable in allowing us to refine the mathematical model to improve the accuracy of prediction. It is likely that there will be a lower bound of error, below which these models cannot go, however, owing to inherent uncertainties and errors in model parameter values and image quality. Determining this lower bound will be a very valuable contribution to this area, providing as it will be the inherent ability of mathematical modelling to contribute to clinical practice and ensuring that the clinicians are aware of the likely errors in predictions.

One of the greatest likely sources of error is the values of model parameters, such as thermal conductivity, which will vary from patient to patient and even spatially within the liver. The literature is very sparse on this, hence for a brief introduction to the limitations of the existing experimental data, e.g. the review by Payne *et al.* [3]. Considerable further work will need to be performed to reduce the errors associated with such variability, in particular, examining the variation in material properties with disease, such as cirrhosis, which is known to affect the flow field and is likely to strongly affect the material parameters. In addition, tumour flow is highly abnormal, often with stagnant flow; incorrect assumptions on the blood flow velocity field may thus overestimate the cooling effect significantly. Likewise, tumour hypoxia will be an additional factor in making the tumour response very different from the response of healthy liver tissue. As the tumour cells die, toxins are released, and these also have an effect on the remainder of the tumour.

Once we start to obtain clinical data from human patients, it will, however, be possible to examine the effects of such errors on the final prediction of lesion size; this sensitivity analysis will also be a valuable tool towards obtaining further experimental data where it is most important and thus needed. This further illustrates the importance of quantitative mathematical modelling and validation in helping to understand which biological questions most need answering and driving biological research forward in combination.

6. Conclusions

Comparison between model predictions and experimental data acquired on healthy animal models shows a very good agreement for the distribution of the ablated zone between the predicted and actual data. By carrying out a direct comparison between the two, it is possible to perform a quantitative validation of the model: a vital part of the development of any system. This is the first such attempt in the liver to close the gap between mathematical modelling and experimental validation of ablation treatment of tumours *in vivo*. As the project proceeds and more experimental data are gathered, further refinement of the model will be performed, in particular, to include animal-/patient-specific information, such as cirrhosis level. Validation in humans will then be performed as the project moves towards practical implementation, with substantial potential for widespread clinical use of a patient-specific intervention planning system. This tool will also provide quantitative results (particularly from validation) that will be very valuable in the development of similar systems for other body organs.

The research leading to these results has received funding from the European Community's Seventh Framework Programme under grant agreement no. 223877, project IMPPACT.

References

1 Hilderbrand, P., Leibecke, T., Kleemann, M., Mirow, L., Birth, M., Bruch, H. P. & Burk, C. 2006 Influence of operator experience in radiofrequency ablation of malignant liver tumours on treatment outcome. *Eur. J. Surg. Oncol.* **32**, 430–434. (doi:10.1016/j.ejso.2006.01.006)
2 Berjano, E. 2006 Theoretical modeling for radiofrequency ablation: state-of-the-art and challenges for the future. *Biomed. Eng. Online* **5**, 24. (doi:10.1186/1475-925X-5-24)
3 Payne, S. J., Peng, T. & O'Neill, D. P. 2010 Mathematical modelling of thermal ablation. *Crit. Rev. Biomed. Eng.* **38**, 21–30.
4 Santos, I., Haemmerich, D., Pinheiro, C. & da Rocha, A. 2008 Effect of variable heat transfer coefficient on tissue temperature next to a large vessel during radiofrequency tumor ablation. *Biomed. Eng. Online* **7**, 21. (doi:10.1186/1475-925X-7-21)
5 Panescu, D., Whayne, J. G., Fleischman, S. D., Mirotznik, M. S., Swanson, D. K. & Webster, J. G. 1995 Three-dimensional finite element analysis of current density and temperature distributions during radio-frequency ablation. *IEEE Trans. Biomed. Eng.* **42**, 879–890. (doi:10.1109/10.412649)
6 Chen, X. & Saidel, G. 2009 Mathematical modeling of thermal ablation in tissue surrounding a large vessel. *J. Biomech. Eng.* **131**, 011001. (doi:10.1115/1.2965374)
7 Khanafer, K. & Vafai, K. 2009 Advances in numerical heat transfer. In *Advances in numerical heat transfer*, vol. 3 (eds W. J. Minkowycz & E. M. Sparrow), pp. 1–28. Boca Raton, FL: CRC Press.
8 Brinck, H. & Werner, J. 1994 Efficiency function: improvement of classical bioheat approach. *J. Appl. Physiol.* **77**, 1617–1622.
9 Brinck, H. & Werner, J. 1995 Use of vascular and non-vascular models for the assessment of temperature distribution during induced hyperthermia. *Int. J. Hyperthermia* **11**, 615–626. (doi:10.3109/02656739509022494)
10 Wulff, W. 1974 The energy conservation equation for living tissue. *IEEE Trans. Biomed. Eng.* **BME-21**, 494–495. (doi:10.1109/TBME.1974.324342)
11 Klinger, H. 1974 Heat transfer in perfused biological tissue I: general theory. *Bull. Math. Biol.* **36**, 403–415. (doi:10.1016/S0092-8240(74)80038-8)
12 Mahjoob, S. & Vafai, K. 2009 Analytical characterization of heat transport through biological media incorporating hyperthermia treatment. *Int. J. Heat Mass Trans.* **52**, 1608–1618. (doi:10.1016/j.ijheatmasstransfer.2008.07.038)

13 Peng, T., O'Neil, D. P. & Payne, S. J. 2011 A two-equation coupled system for determination of liver tissue temperature during thermal ablation. *Int. J. Heat Mass Trans.* **54**, 2100–2109. (doi:10.1016/j.ijheatmasstransfer.2010.12.019)
14 Chen, M. M. & Holmes, K. R. 1980 Microvascular contributions in tissue heat transfer. *Ann. N. Y. Acad. Sci.* **335**, 137–150. (doi:10.1111/j.1749-6632.1980.tb50742.x)
15 Nakayama, A. 2001 A two-energy equation model for conduction and convection in porous media. *Int. J. Heat Mass Trans.* **44**, 4375–4379. (doi:10.1016/S0017-9310(01)00069-2)
16 Roetzel, W. & Xuan, Y. 1998 Transient response of the human limb to an external stimulust. *Int. J. Heat Mass Trans.* **41**, 229–239. (doi:10.1016/S0017-9310(96)00160-3)
17 O'Neill, D. P., Peng, T., Stiegler, P., Mayrhauser, U., Koestenbauer, S., Tscheliessnigg, K. & Payne, S. J. 2011 A three-state mathematical model of hyperthermic cell death. *Ann. Biomed. Eng.* **39**, 570–579. (doi:10.1007/s10439-010-0177-1)
18 Pearce, J. A. 2010 Models of thermal damage in tissues: processes and applications. *Crit. Rev. Biomed. Eng.* **38**, 1–20.
19 Henriques Jr, F. & Moritz, A. 1947 Studies of thermal injury: I. The conduction of heat to and through skin and the temperatures attained therein. A theoretical and an experimental investigation. *Am. J. Pathol.* **23**, 530–549.
20 Moritz, A. R. & Henriques Jr, F. C. 1947 Studies of thermal injury: II. The relative importance of time and surface temperature in the causation of cutaneous burns. *Am. J. Pathol.* **23**, 695–720.
21 Moritz, A. 1947 Studies of thermal injury: III. The pathology and pathogenesis of cutaneous burns. An experimental study. *Am. J. Pathol.* **23**, 915–941.
22 Breen, M., Chen, X., Wilson, D. & Saidel, G. 2002 Modeling cellular thermal damage from radio-frequency ablation. In *2nd Joint EMBS/BMES Conf., Houston, 23–26 October*, vol. 1. IEEE.
23 Szasz, A. & Vincze, G. 2008 Dose concept of oncological hyperthermia: heat-equation considering the cell destruction. *J. Cancer Res. Ther.* **2**, 171–181. (doi:10.4103/0973-1482.29827)
24 O'Neill, D., Peng, T. & Payne, S. 2010 Comparison of two mathematical models for hyperthermic cell death. In *6th World Congress of Biomechanics* (*WCB 2010*), *Singapore*, *1–6 August*, pp. 748–751. Berlin, Germany: Springer.
25 Jung, H. 1986 A generalized concept for cell killing by heat. *Radiat. Res.* **106**, 56–72. (doi:10.2307/3576561)
26 Jung, H. 1989 Step-down heating of CHO cells at 37.5–39°C. *Int. J. Hyperthermia* **5**, 665–673. (doi:10.3109/02656738909140491)
27 Jung, H. 1991 A generalized concept for cell killing by heat: effect of chronically induced thermotolerance. *Radiat. Res.* **127**, 235–242. (doi:10.2307/3577936)
28 Doss, J. D. 1982 Calculation of electric fields in conductive media. *Med. Phys.* **9**, 566–573. (doi:10.1118/1.595107)
29 Khlebnikov, R. & Muehl, J. (eds) 2010 Effects of needle placement inaccuracies in hepatic radiofrequency tumor ablation. In 32*nd Ann. Int. Conf. IEEE EMBS, Buenos Aires, Argentina, 31 August–4 September*, pp. 716–721. IEEE.
30 Schramm, W., Yang, D., Wood, B., Rattay, F. & Haemmerich, D. 2007 Contribution of direct heating, thermal conduction and perfusion during radiofrequency and microwave ablation. *Open Biomed. Eng. J.* **1**, 47–52. (doi:10.2174/1874120700701010047)
31 Griffiths, D. J. & Li, Y. 1996 Charge density on a conducting needle. *Am. J. Phys.* **64**, 706–714. (doi:10.1119/1.18236)
32 Andrews, M. 1997 Equilibrium charge density on a conducting needle. *Am. J. Phys.* **65**, 846–50. (doi:10.1119/1.18671)
33 Peng, T., O'Neill, D. P., Payne, S. J., Bost, C. & Flanagan, R. 2010 Mathematical modeling of directional effects of perfusion on liver tissue temperature of radio frequency ablation. In *6th World Congress of Biomechanics* (*WCB 2010*), *1–6 August* (eds R. Magjarevic, C. T. Lim & J. C. H. Goh), pp. 740–743. Berlin, Germany: Springer.
34 Podhajsky, R., Yi, M. & Mahajan, R. 2009 Differential and directional effects of perfusion on electrical and thermal conductivities in liver. In *31st Ann. Int. Conf. IEEE EMBS, Minneapolis, 3–6 September*, pp. 4295–4298. IEEE.

35 Rueckert, D., Sonoda, L. I., Hayes, C., Hill, D. L. G., Leach, M. O. & Hawkes, D. J. 2002 Nonrigid registration using free-form deformations: application to breast MR images. *IEEE Trans. Med. Imaging* **18**, 712–721. (doi:10.1109/42.796284)
36 Rohlfing, T., Maurer Jr, C. R., O'Dell, W. G. & Zhong, J. 2004 Modeling liver motion and deformation during the respiratory cycle using intensity-based nonrigid registration of gated MR images. *Med. Phys.* **31**, 427–437. (doi:10.1118/1.1644513)
37 Studholme, C., Hill, D. L. G. & Hawkes, D. J. 1997 Automated 3D registration of MR and PET brain images by multi-resolution optimization of voxel similarity measures. *Med. Phys.* **24**, 25–35. (doi:10.1118/1.598130)
38 Press, W. H., Teukolsky, S. A., Vetterling, W. T. & Flannery, B. P. 1992 *Numerical recipes in C*. New York: Press Syndicate of the University of Cambridge.
39 Rangayyan, R. M., Vu, R. H. & Boag, G. S. 2006 Delineation of the diaphragm in CT images to improve segmentation of the tumor mass in neuroblastoma. In *Proc. CARS 20th Int. Congress and Exhibition: Computer Assisted Radiology, Osaka, Japan*, pp. 78–80.
40 Selle, D., Preim, B., Schenk, A. & Peitgen, H. O. 2002 Analysis of vasculature for liver surgical planning. *IEEE Trans. Med. Imaging* **21**, 1344–1357. (doi:10.1109/TMI.2002.801166)
41 Erdt, M., Raspe, M., & Suehling, M. 2008 Hepatic vessel segmentation using graphics hardware. Lecture Notes in Computer Science, no. 5128, pp. 403–412.
42 Yim, P. J., Choyke, P. L. & Summers, R. M. 2000 Gray-scale skeletonization of small vessels in magnetic resonance angiography. *IEEE Med. Imaging* **19**, 568–576. (doi:10.1109/42.870662)
43 Alhonnoro, T. *et al.* 2010 Vessel segmentation for ablation treatment planning and simulation. Lecture Notes in Computer Science, no. 6361, pp. 45–52.
44 Yushkevich, P. A., Piven, J., Hazlett, H. C., Smith, R. G., Ho, S., Gee, J. C. & Gerig, G. 2006 User-guided 3D active contour segmentation of anatomical structures: significantly improved efficiency and reliability. *Neuroimage* **31**, 1116–1128. (doi:10.1016/j.neuroimage.2006.01.015)
45 Lorensen, W. E. & Cline, H. E. 1987 Marching cubes: a high resolution 3D surface construction algorithm. In *Proc. 14th Ann. Conf. Computer Graphics and Interactive Techniques*, pp. 163–169.
46 Elmer. 2011 Open source finite element code. See http://www.csc.fi/english/pages/elmer.